

G8542

**DESIGN, FABRICATION AND CHARACTERIZATION
OF FIBER OPTIC SENSORS FOR PHYSICAL
AND CHEMICAL APPLICATIONS**

Thomas Lee S.

International School of Photonics
Cochin University of Science and Technology,
Cochin - 682022, India

Ph D Thesis submitted to Cochin University of Science and Technology in
partial fulfillment of the requirements for the award of the
Degree of Doctor of Philosophy.

May 2003

G18542

Design, Fabrication and Characterization of Fiber Optic Sensors for Physical and Chemical Applications

Ph D thesis in the field of Photonics

Author

Thomas Lee S.
Research Fellow, International School of Photonics
Cochin University of Science and Technology,
Cochin – 682 022, India
lee@cusat.ac.in; thomaslees2002@hotmail.com

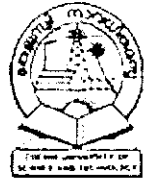
Research Advisors

Dr V P N Nampoori
Professor, International School of Photonics
Cochin University of Science and Technology,
Cochin - 682 022, India
vpnnampoori@cusat.ac.in

Dr P Radhakrishnan
Professor, International School of Photonics
Cochin University of Science and Technology
Cochin - 682 022, India
radhak@cusat.ac.in

**International School of Photonics, Cochin University of Science and Technology,
Cochin– 682 022, India
Website: www.photonics.cusat.edu**

May 2003




International School of Photonics
Cochin University of Science and Technology
Cochin - 682 022, India

CERTIFICATE

Certified that the work presented in this thesis entitled “DESIGN, FABRICATION AND CHARACTERIZATION OF FIBER OPTIC SENSORS FOR PHYSICAL AND CHEMICAL APPLICATIONS” based on the bonafide research work done by Mr. Thomas Lee S. is an authentic record of research work done by him under my guidance in the International School of Photonics, Cochin University of Science and Technology, Cochin 682 022, India and has not been included in any other thesis submitted previously for the award of any degree.

Cochin - 22
Date: 16th May 2003

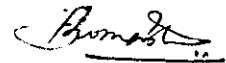

Prof. V.P.N. Nampoori
(Supervising Guide)
International School of Photonics,
CUSAT.

DECLARATION

I hereby declare that the work presented in this thesis entitled “DESIGN, FABRICATION AND CHARACTERIZATION OF FIBER OPTIC SENSORS FOR PHYSICAL AND CHEMICAL APPLICATIONS” is based on the original work done by me under the guidance of Prof. V.P.N.Nampoori, International School of Photonics, and the co-guidance of Prof. P.Radhakrishnan, International School of Photonics, Cochin University of Science and Technology, and it has not been included in any other thesis submitted previously for the award of any degree.

Cochin - 22

Date: 16th May 2003



Thomas Lee S.

WORDS OF GRATITUDE

Prof. V P Narayanan Nampoori, my guide, was with me through thick and thin. His sincerity and commitment to profession has made a deep impression in me. I cannot remember a single occasion when he became angry or irritated even under tough circumstances. His ever-smiling face and humility are highly sought after, yet hard to achieve qualities.

Prof. P Radhakrishnan, my co-guide, has always been an inspiration for me. He is a man of professionalism combined with a caring nature. His never to give up attitude has been a motivation for me. I take this opportunity to thank him for his wholehearted support.

I do not know what is the kind of relationship I have with Prof. C P Girijavallabhan, the founder of International School of Photonics (ISP). Sometimes he is like a close friend, sometimes a critic and all the time, a classic teacher. His great experimental skill as well as his passion for electronics was a real help for my research work. I really want to express my gratitude to him.

I remember the outstanding M. Tech lectures and special classes of Prof. V M Nandakumaran, Director of ISP, which has really enlightened me with great ideas of physics and mathematics. I thank him for his lectures and giving me an opportunity to work in the labs of ISP.

Mr. C M Basheer has always been there for any kind of help, especially while he had the charge of the library of ISP. I will be thankful to him always.

I do believe that there is a woman behind every man's success. Therefore, I thank the wives of all the great teachers of ISP.

During my research, I went through the line marked by Dr. Nibu A George. His logic and good understanding of physics helped me in sorting out many of the challenges I had to face in my research career.

I would like to give a special thanks to Mr. B Aneeshkumar for promptly collecting the references which I needed during my work. Words cannot express the gratitude I feel for him for this and constructing such a wonderful website for ISP.

Mr. Sebu Thomas Koleth, my M Sc classmate has been next to door whenever I needed some help, whether in developing some electronic circuits or in dealing with some computer problems. Mr. P P Vinodkumar, Dept of Computer Science, has been ready to help me without any hesitation.

During my stay at ISP, I have been fascinated by the technical skill of Mr. P Sureshkumar. He has made our life at ISP very cheerful by his enthusiasm and quick

wittedness. A home away from home provided by his wife, Mrs. Vijayakumari and their children, Paru and Appu will be cherished always. I am very thankful to him and Mr. Sajan D George for their endeavor to realize my dream of visiting a foreign country in the form of attending a conference.

I would like to thank Mr. Joy and Mr. Ajith for all the support and guidelines they have been providing me during my stay at St. Thomas College, Pala.

Prof. N V Unnikrishnan, Dr. Gin Jose and Mr. Vinoy, Department of Physics, M G University has been very friendly and kindly to me. Betty Joseph and Manju C M, M Sc students of M G University were very helping during the early stages of my work.

I have seen only a few persons like Prof. K Thyagarajan, IIT Delhi. I thank him for giving me so much freedom with him. Prof. V M Murugesan, NTU Singapore has been very much interested in my work. Prof. Gargi Vishnoi has been like my elder sister. I thank them for all their effort. I thank Prof. S Sugunan, Dept of Applied Chemistry for his discussions about the chemical aspects of my work.

It will be curse if I forget the teachers who have brought me to the starting point of this work. A special note of gratitude to Dr. T Ramesh Babu, Dr. M R Anantharaman, Dr. T M A Rasheed, Dr. M K Jayaraj, Prof. M Sabir, Prof. K P Rajappan Nair, Prof. K Babu Joseph, Prof. K P Vijayakumar, Department of Physics from where I graduated and my teachers at St. Thomas College, Pala where I did my undergraduate studies.

Mr. Abraham V Scaria and Mr. Vinu Namboory, my juniors at ISP have been of great help for the successful completion of this thesis.

I acknowledge the help rendered by Mr. Shaji S, Mr. Shibu M Eapen, Mrs. B Syamalakumari, Mrs. T Nandini, Mrs. Usha John, Mr. Thomas Zacharia, Mr. Sunny Kuriakose, Mr. K K Vijayan, Mr. K Ravindranath, Mr. C Joseph Mathai, Mr. Saji Augustine, Mr. M C Santhoshkumar, Mr. S Saravanan, Dr. Bindu K, Ms. Minu Joy, Mr. Aldrin Antony, Mr. Alex Mathew, researchers in the neighbouring departments of CUSAT for allowing me to utilize some of the facilities uniquely available to them.

I express my deep sense of gratitude to Mr. K Samuel Varghese and Ms. Priyamvada for the efforts they have made to chart the transmission spectrum of fiber gratings.

The experimental designs in my mind would not have materialized without the support of the maestros of USIC. I am grateful to Mr. Casimir, Mr. A B Muraleedharan, Mr. Jose, Mr. Joshy, Mr. Jose, Mr. Gopi Menon and Mr. Sukumaran.

I remember with gratitude the guidance of my seniors Dr. Shelly M John and Dr. Riju C Isaac in the form of timely advices. My senior research scholars at ISP Mr. Pramod Gopinath, Mr. Binoy Paul, Mr. K P Unnikrishnan, Mr. M G Jibukumar, Mr. Prasanth Ravi, Mrs. Bindu Murali have been always helping me to understand the history and tradition of ISP, and to familiarize with the various sophisticated instruments. I remember with gratitude, my friend and classmate Ms. Pravitha Ramanand to stand with me from the very first day of joining at ISP. My fellow researchers, Mrs. K Geetha, Ms. Dilna S, my class mate Mr. Rajesh S, Ms. A Santhi, Ms. Lekshmi S, Ms. Rekha Mathew, Sr. Ritty J Nedumpara, Mr. Jijo P U, Mr. Manu Punnen John, and Mr. Rajesh M for all the support they provided me. Our “young scientist” Dr. A Deepthy has always been like a research guide. I would like to thank all the M. Tech students of ISP, especially Mr. R Dineshkumar with whom I had some collaborative work at the concluding stages of my work and Mr. Babu Jacob for the fruitful discussions.

I thank the present and past staff at ISP office, Mrs. Prasannakumari, Mrs. Hema B Nair, Mrs. Pushpa, Mrs. Usha, Mrs. Chellappan, Mrs. Jessy and Mrs. Maya for their co-operation. I acknowledge the help rendered by the office staff at the University administrative office. I thank all the staff members of physics, ISP and central library.

I thank all the M. Tech. students and M. Sc. Students who have collaborated with me either in the form of projects or discussions.

I acknowledge Council of Scientific and Industrial Research, All India Council for Technical Education, India, and Netherlands Universities Funding for International Collaboration for the financial assistance during the work of my Ph. D. I thank Dr. Mathew Malepparambil, Principal of the college where I presently work for being understandable at times of crisis.

I thank all my teammates of Shuttle Badminton and Basketball for making my leisure productive. A special note of gratitude goes to Prof. James Joseph, Director of Physical Education for all his support. I also thank all my roommates who happened to share my hostel room.

Last, but not the least I thank Ms. Jyotsna Ravi for my wonderful years at CUSAT. It is very hard for me to forget the ways she strived to make my life happy.

THOMAS LEE S.

LIST OF PUBLICATIONS

In International Journals

1. **Thomas Lee S**, Nibu A George, P Sureshkumar, P Radhakrishnan, C P G Vallabhan and V P N Nampoore, Chemical sensing with microbent optical fiber, *Opt. Lett.* **20**, 1542-1543 (2001)
2. **Thomas Lee S**, Gin Jose, V P N Nampoore, C P G Vallabhan, N V Unnikrishnan and P Radhakrishnan, A sensitive fibre optic pH sensor using multiple sol-gel coatings, *J. Opt. A: Pure Appl. Opt.* **3**, 355-359 (2001)
3. **Thomas Lee S**, Gin Jose, Manju C M, Betty Joseph, M Shelly John, V P N Nampoore, C P G Vallabhan, N V Unnikrishnan and P Radhakrishnan, A fiber optic pH sensor with dye doped multi-layer sol-gel coatings, *Proceedings of SPIE - International Society for Optical Engineering*, **4417** (2001)
4. **Thomas Lee S**, B.Aneeshkumar, P Radhakrishnan, C P G Vallabhan and V P N Nampoore, A microbent fiber optic pH sensor, *Opt. Comm.*, **205**, 253 - 256 (2002)
5. **Thomas Lee S**, K Geetha, V P N Nampoore, C P G Vallabhan and P Radhakrishnan, Microbent optical fibers as evanescent wave sensors, *Opt. Engg.* **41** 3260-3264 (2002)
6. **Thomas Lee S**, P Sureshkumar, K Geetha, P Radhakrishnan, C P G Vallabhan & V P N Nampoore, A microbent optical fiber for refractive index measurement, *Proceedings of SPIE - International Society for Optical Engineering*, **4920** (2002)
7. **Thomas Lee S**, P Radhakrishnan, C P G Vallabhan & V P N Nampoore, Macrobending in optical fiber for weight and displacement

measurement, Proceedings of SPIE – International Society for Optical Engineering, **4946** (2002)

8. **Thomas Lee S**, P Sureshkumar, K P Unnikrishnan, P Radhakrishnan, C P G Vallabhan, S Sugunan & V P N Nampoore, Evanescent Wave Fiber Optic Sensors for Trace Analysis of Fe³⁺ in water, Meas. Sci. Technol. (in press)
9. **Thomas Lee S**, P Sureshkumar, P Radhakrishnan, C P G Vallabhan V P N Nampoore, Long Period Gratings in Multimode Optical Fibers: Application in Chemical Sensing, Opt. Comm. (in press)
10. P Sureshkumar, **Thomas Lee S**, V P N Nampoore, C P G Vallabhan & P Radhakrishnan, Design and Development of an LED based fiber optic evanescent wave sensor for simultaneous detection of chromium and nitrite traces in water, Opt. Comm., **214**, 25-30 (2002)
11. Achamma Kurian, Nibu A George, **Thomas Lee S**, D Sajan George, K P Unnikrishnan, V P N Nampoore and C P G Vallabhan, Realization of logic gates using thermal lens technique, Laser Chem., **20**, 81-87 (2002)
12. Achamma Kurian, K P Unnikrishnan, **Thomas Lee S**, Sajan D George, V P N Nampoore and C P G Vallabhan, Studies on two photon absorption of aniline using thermal lens effect. J. Nonlinear Optical Physics & Materials (In Press)

Papers Presented in Conferences/ Seminars

1. **Thomas Lee S**, R Dinesh Kumar, P Radhakrishnan, C P G Vallabhan and V P N Nampoore, Long Period Grating Fibers for Chemical Sensing, Photonics 2002 International Conference On Fiber Optics And Photonics (December 14-16), Bombay.
2. **Thomas Lee S**, P Radhakrishnan, C P G Vallabhan and V P N Nampoore, Characterising a Microbent Optical fiber for chemical

sensing, National Laser Symposium 2001, December 19-21, CAT Indore. (2001)

3. **Thomas Lee S, V P N Nampoori, C P G Vallabhan and P Radhakrishnan**, A permanently microbent optical fiber for detecting chemical species, BBOFCT, December 5-7, Jalgaon, Maharashtra (2001)
4. **Thomas Lee S, Siril T George & Majo Mary Mathew**, Sol-gel technique for IO component fabrication, Second International Conference and XXVII Annual Convention of the Optical Society, August 27 - 29, Trivandrum, Kerala, India (2001)
5. **Thomas Lee S, C M Manju, Betty Joseph, Gin Jose, M Shelly John, P Radhakrishnan, V P N Nampoori, C P G Vallabhan and N V Unnikrishnan**, A fiber optic pH sensor with multi-layer sol-gel coatings, Photonics 2000-International Conference On Fiber Optics And Photonics, (December 18-20) Allied Publishers, New Delhi, (2000)
6. **Thomas Lee S, Manju C M, Betty Joseph, Gin Jose, M Shelly John**, A fiber optic pH sensor with multi-layer sol-gel coatings, Proceedings of APSYM 2000, (December 6-8), Cochin, (2000)

CONTENTS

Preface

Chapter 1 INTRODUCTION TO FIBER OPTICS

1.1 Chronological development - The History of Fiber Optics (FO)	1
1.2 Advantages of optical fiber	2
1.2.1 Large bandwidth	2
1.2.2 Immunity to external interferences:	3
1.2.3 Security or signal confinement:	3
1.2.4 Small size and weight	3
1.3 Classification of optical fibers	4
1.4 Propagation of light through a medium	5
1.4.1 Maxwell's equations:	5
1.4.2 Boundary conditions at dielectric interfaces	6
1.4.3 Total internal reflection and evanescent wave	8
1.5 Light propagation through an optical fiber	9
1.5.1 Modes in an optical fiber:	9
1.5.2 Normalized frequency and normalized propagation constant:	11
1.6 Single Mode Fibers:	11
1.7 Concepts of fiber optic communication:	12
1.7.1 Attenuation:	12
1.7.1.1 Optical absorption in Silica	12
1.7.1.2 Scattering losses	13
1.7.2 Dispersion:	14
1.7.3 Innovative technology	14
1.8 Fiber optic Sensors:	15
1.9. Classification of fiber optic sensors	16
1.9.1 Intensity modulated FOS (IMFOS)	17
1.9.1.1 Misalignment loss sensors	17
1.9.1.2 Shutter/Schlieren multimode FOS	18

1.9.1.3 Microbend loss sensors	18
1.9.1.4 Evanescent wave sensors	18
1.9.2 Phase modulated interferometric sensors	19
1.9.2.1 Phase detection	19
1.9.2.2 Mach-Zehnder interferometer	20
1.9.2.3 Michelson Interferometer	20
1.9.2.4 Fabry-Perot Interferometer	21
1.9.2.5 Sagnac Interferometer	21
1.9.3 Polarimetric sensors	22
1.9.4 Frequency modulated sensors	24
1.9.5 Wavelength modulated sensors	24
1.10 Major areas of application of fiber optic sensors	24
1.10.1 Chemical, biochemical and biomedical applications	24
1.10.1.1 Liquid phase sensing	25
1.10.1.2 Transmission spectroscopy	25
1.10.1.3 Evanescent wave spectroscopy	25
1.10.1.4 Fluorescence spectroscopy	25
1.10.1.6 In vivo medical sensors	26
1.10.2 Fiber optic gyros	26
1.10.3 Condition monitoring and engineering diagnostics	27
1.10.4 Distributed sensors	27
1.10.5 Fiber optic smart structures	28

Chapter 2 SENSITIVE FIBER OPTIC PH SENSORS USING MULTIPLE SOL-GEL COATINGS

2.1 Theory	32
2.1.1 Spectrophotometry	32
2.1.2 Evanescent wave spectroscopy	33
2.2 Indicator immobilization techniques	38

2.2.1 Immobilization by electrostatic interactions	38
2.2.2 Immobilization by hydrophobic interactions	39
2.2.3 Cellulose for covalent binding and entrapment of pH indicators	39
2.2.4 Photochemical immobilization	39
2.2.5. Electrochemical immobilization	40
2.2.6 Other organic polymeric substrates	40
2.2.7 Controlled-pore glass (CPG)	40
2.3 Sol-gel glass	40
2.3.2 Main steps involved in sol-gel process.	42
2.3.2.1 Hydrolysis and condensation of metal alkoxide	43
2.3.2.2 Polymerization	43
2.3.2.3 Gelation	44
2.3.2.4 Aging	44
2.3.2.5 Drying	45
2.3.2.6 Sintering	46
2.3.4 Thin film coating techniques	46
2.3.5 Various forms of sol-gel derived ceramics	48
2.3.5.1 Thin films	48
2.3.5.2 Monoliths	49
2.3.5.3 Powders, grains and spheres	49
2.3.5.4 Fibers	49
2.3.5.5 Composites	49
2.4 Experiment	49
2.4.1 Probe fabrication	49
2.4.2 The experimental set-up	52
2.5 Results and Discussion	56

Chapter 3. CHEMICAL SENSING USING MICROBENT OPTICAL FIBERS

3.1 Theoretical Background	69
3.1.1 Generic fiber microbend sensor	73
3.2 Experimental	74
3.3 Results and Discussion	76
3.3.1 Sensitivity dependence on bending length and bending amplitude	80
3.3.2 Microbent pH sensing	82
3.3.3 Microbent refractometry	84

Chapter 4. INTERFEROMETRIC WEIGHT & DISPLACEMENT SENSOR & POLLUTION MONITORING SENSORS FOR Fe³⁺ & Mn²⁺ DETECTION

4.1 Phase modulated optical fiber sensors	89
4.1.1 Phase modulation mechanisms in optical fibers	90
4.1.2 Experimental setup	92
4.1.3 Results and Discussion	96
4.2 Fiber optic Fe ³⁺ and Mn ²⁺ detection in aqueous environments	98
4.2.1 LabVIEW fundamentals	100
4.2.1.1 Front Panel	101
4.2.1.2 Block Diagram	101
4.2.2 Experimental	102
4.2.3 Results and Discussion	109
4.3. Referencing strategies for intensity modulated fiber optic sensors	115

Chapter 5. LONG PERIOD GRATINGS IN MULTIMODE FIBERS: APPLICATION IN CHEMICAL SENSING

5.1 Photosensitivity of glass	122
5.2 Grating Fabrication Techniques	124
5.2.1 Holographic technique	125
5.2.2 Phase Mask Technique	125

5.2.3 Amplitude mask technique	127
5.3 Other types of gratings in optical fibers	128
5.4 Theoretical Background	128
5.4.1 Coupled mode theory	128
5.4.2 Coupled mode equations for co-directional coupling	129
5.4.3 Coupling by periodic perturbation	131
5.4.3.1 Co-Directional Coupling under Phase Matching Condition	132
5.4.3.2 Coupled mode equations for contra-directional coupling	134
5.4.4 Principle of operation of Long Period Gratings	135
5.5. Sensors based on fiber gratings	138
5.5.1 Long Period Grating Sensors	141
5.6. Experimental	141
5.7 Results and Discussion	143

PREFACE

The dramatic growth in technology of optical fiber communication and optics based sensing has fuelled interest in fiber optic sensors (FOS), application of which ranges from biomedicine to defense. Since the major development of FOS in 1977, considerable effort has been expended into developing sensors based on optical fibers for both physical and chemical parameters. They are extensively used in various applications like pollution monitoring, automobile industry, aerospace, smart structures, blood analysis, remote sensing etc. The desirable features of the optical fiber include (i) non electrical nature (ii) contactless behavior (iii) small size and weight (iv) immunity to radio frequency and electromagnetic interference (v) solid state reliability (vi) secure data transmission (vii) resistance to ionizing radiation etc. However, the most attractive feature of FOS that make them suitable for sensing applications is their inherent ability to serve as both the sensing element and the signal transmission medium allowing the electronic instrumentation for signal processing to be located remotely from the measurement site. Theoretically, there exists no parameter that cannot be sensed by FOS. Light intensity, displacement, position, temperature, pressure, rotation, sound, strain, magnetic field, electric field, radiation, pH, concentration, refractive index and turbidity are some of the parameters that can be sensed using FOS with great accuracy and reliability.

An optical sensor is a transducer that converts a change in one parameter into a corresponding variation in any of the characteristics of light. FOS can be broadly classified into intrinsic and extrinsic types. In the intrinsic variety, the measurand itself changes some of the physical or chemical properties of the optical fiber which in turn modulates the guided light. In the extrinsic type the role of the fiber is restricted to just a carrier of light signal. The intrinsic FOS are again subdivided into intensity, phase, polarization, wavelength and frequency modulated sensors according to, which of these five parameters describe the light transmission through the fiber. In

the present investigation, effort has been taken for the design, fabrication and characterization of some FOS for various physical and chemical applications. The thesis is organized in six chapters.

The thesis begins with an introductory chapter that provides a general understanding of the characteristics of optical fibers and how they are used in the development of various sensors. A rigorous mathematical treatment of light propagation is used wherever necessary and emphasis is given on the physical understanding of the various properties of optical fibers. A review on FOS illustrates the historical development of FOS and state of the art technology. The classification of FOS into various types and the importance and use of each type is detailed.

Chapter II describes the design and development of a fiber optic pH sensor, based on sol-gel technology. Different technologies like evanescent wave phenomenon in optical fibers, spectrophotometry of pH sensitive dyes, and sol-gel thin film formation technique are suitably blended together in the fabrication of this sensor. Various types of fiber optic pH sensors fabricated include short-range pH sensors using single dyes and a long-range pH sensor using a dye mixture. The sensitivity of all these sensors is found to have enhanced by using multilayer sol-gel thin film coatings. The sensors are also characterized in terms of reversibility, repeatability and temporal response.

Microbending in optical fibers is conventionally used for physical sensing applications. However, work done on their chemical sensing applications is described in **chapter III**. A possible model for explaining the observed phenomenon is also suggested. Permanently micobent plastic fibers with cladding are found to be a possible substitute for unclad fibers, in chemical sensing applications that involves both absorption and refractive index measurements. Fiber optic pH sensing using unclad plastic-clad silica (PCS) fibers described earlier in chapter II, is shown to be viable with the present microbent plastic optical fibers too.

In **chapter IV**, details of the development of various FOS for physical and chemical sensing applications are provided. Chemical sensing includes detection of iron and manganese ions, using evanescent wave phenomenon. The use of various types of optical fibers such as PCS fiber and microbent plastic fiber saws the seed for a comparative study of the various detection schemes in optical absorption measurements. In addition, a comparative study between the use of a laser source and a lambertian source (LED) in driving the FOS is also included in this chapter. The fabrication and characterization of a displacement/weight sensor using interferometric phenomenon forms the sensor for physical applications. Moreover, the sensing shell fabrication and implementation of the electronic instrumentation for signal processing in the form of a fringe counter is detailed. The chapter concludes with a note on the realization of a new referencing strategy for intensity modulated FOS based on cladding mode detection.

Long period gratings (LPGs) in single mode fibers are extensively used in communication technology as well as in sensing applications. On the other hand, LPGs in multimode fibers (MMF) are in their infancy. In **chapter V**, we provide the use of LPGs in MMF for chemical sensing in the form of absorption measurements. The fabrication details and the basic mechanism of LPG formation are described along with the theory and operation of LPGs. The similarity between LPGs and microbends in chemical sensing applications is also brought out. Moreover, optical spectrum analyser plots predict their use in the field of communications as well.

Finally, a short discussion on the future prospects, based on the summary and conclusion of the present work is described in **chapter VI**.

Introduction to Fiber Optics

1.1 Chronological development - The History of Fiber Optics (FO)

The history of communication through light can be traced as far back as 6th century B.C. when fire signals were used to convey the news of Troy's downfall all the way from Asia Minor to Argos. Left alone, light will travel in straight lines. However, the bending of light when it travels through a jet of water was first shown by Daniel Colladon, a Professor at University of Geneva, in 1841 [1]. In 1880, an engineer from Massachusetts, William Wheeler patented an idea to channelize light through hollow metallic pipes. Meanwhile in Washington, a young scientist who already had an international reputation was working on what he considered as his greatest invention-the photophone consisting of a diaphragm mirror that vibrated with sound and a light beam impinged on it varied accordingly. At the distant end, a selenium detector was used to convert the light signal back to sound. The first telegraph devised by French engineer Claude Chappe in the 1870's was an optical telegraph. However, Samuel Morse's electrical telegraph followed by Bells telephone put aside the optical telegraph.

Following Colladon, bent glass rods were made to guide light. However, it was found that light could leak out whenever the rod touches something other than

air. The solution to this problem was solved by Brian O'Brien, and Harry Hopkins and Narinder Kapany in the 1950's by proposing a coating termed as cladding to the waveguide. The cladding would confine light within the core because its refractive index was below that of the core. The first use of such a clad fiber was in imaging. O'Brien bundled many fibers together so that a pattern of light formed at one end of the bundle would be recreated at the other end.

Theodore H Maiman's demonstration of the first laser in 1960 renewed interest in optical communication after about a century. However, the idea of free space communication was found to be impractical because of various losses and uncertainties involved. Hence, glass was thought to be a better alternative. However, there remained a serious problem as glass absorbed too much light. A highly transparent window itself absorbs 90% of light if its thickness is 10m, which is 1000-dB/km as against 0.2-dB/km for today's optical fiber. Nevertheless, the theoretical work by Charles K Kao and George Hockham revealed that the absorption in glass was merely due to the presence of impurities. Moreover, they predicted that fibers could be made with loss less than 20-dB/km (90%absorption for 500m). In 1969, Nippon announced a graded index fiber having 100-dB/km loss. Later in 1970, Corning came up with a still lower loss fiber with 20-dB/km thus making optical fibers usable for communication purposes. Now we are in the 3rd generation of fiber optic communication with an operating wavelength of 1.55 μ m and a loss of 0.2dB/km, after the first and second generation operating at 0.85 μ m with 22-dB/km loss and 1.31 μ m with 0.5-dB/km loss. Such a low loss of 0.2-dB/km allows the signal to propagate 80km without amplification. Metal coaxial cables that have been replaced by fibers having comparable information capacity would require dozens of amplifiers over a distance of 80 km(depending on the transmission rate) [1-18].

1.2 Advantages of optical fiber

1.2.1 Large bandwidth

The prerequisite for a good telecommunication medium is not low loss alone, but also high data transfer rate or large bandwidth. Because of high frequency of the optical

carrier signal (10^{14} Hz) and the availability of high-speed sources and detectors (mostly of semiconducting origin) large bandwidth of THz in analog communication or tera bits /second for digital communication is possible and has been achieved using dense wavelength division multiplexing (DWDM) technology. It may be noted that a typical voice signal in telephone requires a bandwidth of 4 kHz where as a video signal requires 6 MHz using analog communication. Since fiber optic communication is digital (as it is less prone to distortion than analogue) a voice channel would require 56kbits/second. That means over one lakh telephone connection can be made with a pair of optical fibers.

1.2.2 Immunity to external interferences:

Optical fibers, glass or plastic, are insulators. No electric currents flow through them, either due to the transmitted signal or due to external radiation striking it. Therefore, fibers can have excellent rejection of radio frequency interference (RFI) and electromagnetic interference (EMI). RFI refers to the interference caused by the radio and television stations, radar and other signals originating in electronic equipment. EMI includes these sources as well as those caused by natural phenomena (such as lightning) or caused unintentionally (such as sparking).

1.2.3 Security or signal confinement:

Unlike coaxial cables that radiate energy (both electric and magnetic), optical fibers confine the energy to it, thus offering a high degree of security and privacy. Any external intrusion by modifying the physical properties of the fiber will result in a loss of signal at the receiver that can be easily detected.

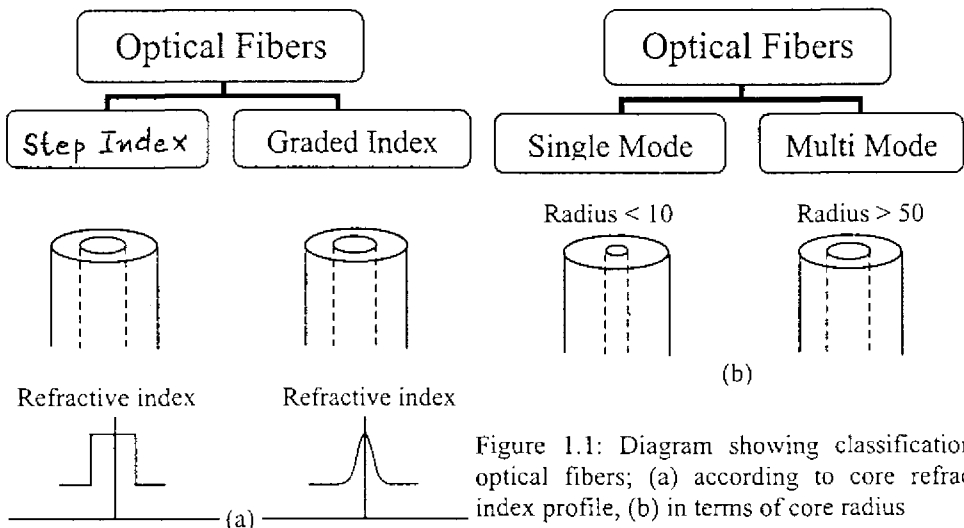
1.2.4 Small size and weight

A dramatic comparison can be made between a standard wire telephone cable and a fiber cable. The metal cable contains 900 twisted- wire pairs and its diameter is 70 mm. Each pair carries 24 channels (T1 rate – 1.56 Mbits/sec) so the cable capacity is 21600 calls. One fiber cable developed for telephone applications has a 12.7 mm diameter and contains 144 fibers, each operating at T3 rate (672 channels – 43 Mbits/sec). This fiber cable has a capacity of 96768 calls.

1.3 Classification of optical fibers

A detailed description of fiber classification is given in this section. The basic structure of an optical fiber consists of a dielectric cylinder, core, of a few micron thickness and refractive index n_1 , surrounded by another cylinder, cladding, of refractive index n_2 . Although in principle, a cladding is not necessary for the light propagation through an optical fiber it reduces scattering loss that results from dielectric discontinuities at the core surface, it adds mechanical strength to the fiber, and it protects the core from absorbing surface contaminants with which it could come in contact. In low-loss and medium-loss fibers, the core material is generally glass and surrounded by either a glass or plastic cladding. Higher loss plastic optical fibers (POF) with both core and cladding made of plastics like poly methyl methacrylate (PMMA) are also widely used. In addition, most fibers are encapsulated in an elastic abrasion resistant plastic material which gives further strength to the fiber and mechanically isolates or buffers the fiber from small geometrical irregularities, distortions or roughness of adjacent surfaces.

An optical fiber can be classified in two ways; either based on its refractive index profile or on its core radius. In the former scheme, fibers are either termed as step index and graded index depending on whether the core has a constant refractive index gradient or a graded index profile. Alternatively, fibers can be either single mode or multimode depending on the size of the core in the latter schemes.



1.4 Propagation of light through a medium

The basic mechanism by which light is transmitted through an optical fiber is total internal reflection (TIR). When light is incident on the boundary of an optically denser medium (refractive index n_1) that separates it from a rarer medium (refractive index n_2 , $n_1 > n_2$) at an angle greater than the critical angle it will be totally internally reflected back to the denser medium itself. As is the case with most of the physical phenomena, light propagation in optical fibers can be dealt with varying degrees of sophistication and accuracy. The simplest approach in this regard is that using geometrical optics, which gives satisfactory results when the propagating distance is large compared to the wavelength of light. However in dealing with optical fibers, having dimensions comparable with that of light, wave optics (physical optics) approach using Maxwell's equations is preferred. 0

1.4.1 Maxwell's equations:

The transverse nature of light is exploited in the description of light propagation through optical fibers. To make the thesis self-contained a brief account of electromagnetic waves is given below. Maxwell's equation in a medium can be written either in the differential or integral form

$$\nabla \cdot \bar{D} = \rho \quad \int \bar{D} \cdot d\bar{s} = Q_{\text{enclosed}} \quad (1.1)$$

$$\nabla \cdot \bar{B} = 0 \quad \int \bar{B} \cdot d\bar{s} = 0 \quad (1.2)$$

$$\nabla \times \bar{E} = -\frac{\partial \bar{B}}{\partial t} \quad \oint_{\text{surface}} \bar{E} \cdot d\bar{l} = -\frac{\partial}{\partial t} \int \bar{B} \cdot d\bar{s} \quad (1.3)$$

$$\nabla \times \bar{H} = \frac{\partial \bar{D}}{\partial t} + \mathbf{J} \quad \oint_{\text{loop}} \bar{H} \cdot d\bar{l} = \int_{\text{area}} \bar{J} \cdot d\bar{s} + \frac{\partial}{\partial t} \int_{\text{area}} \bar{D} \cdot d\bar{s} \quad (1.4)$$

These equations are first order-coupled differential equations. In a homogeneous medium they can be easily decoupled by differentiating them once again to get the wave equation as

$$\nabla^2 \bar{E} = \mu\epsilon \frac{\partial^2 \bar{E}}{\partial t^2} \quad (1.5)$$

$$\nabla^2 \bar{H} = \mu\epsilon \frac{\partial^2 \bar{H}}{\partial t^2} \quad (1.6)$$

or

where $\overline{E}, \overline{H}, \overline{D}, \overline{B}, \mu, \varepsilon$ have their usual meanings. The above equations are vector equations and ∇^2 is called the vector Laplacian. They can be simplified by rewriting them in terms of the components of the fields. In rectangular coordinates, the vector Laplacian breaks into three uncoupled components which is the scalar component wave equation given by

$$\nabla^2 E_i = \mu\varepsilon \frac{\partial^2 E_i}{\partial t^2}, \quad (i=x, y, z) \quad (1.7)$$

Here ∇^2 is the scalar Laplacian given by $\nabla^2 = \frac{\partial^2}{\partial x^2} + \frac{\partial^2}{\partial y^2} + \frac{\partial^2}{\partial z^2}$. The choice of coordinate system is critical to solving the wave equation. For example, choosing rectangular coordinates to describe a wave in a cylinder leads to component coupling upon reflection at the cylindrical surface. That means the Cartesian components are inseparable in such a system. When the coordinate system (for example, cylindrical co-ordinate system in this case) can be found with no coupling between orthogonal components, the individual equations can be solved independently by the scalar wave equation.

In general, it can be written as

$$\nabla^2 \psi = \mu\varepsilon \frac{\partial^2 \psi}{\partial t^2} \quad (1.8)$$

To find a solution assume that $\psi = \psi(r, t)$ and use the separation of variables to get

$$\psi = \psi(r)\phi(t) = \psi_0 e^{ikr} e^{i\omega t} \quad (1.9)$$

the constant of integration being neglected.

The term ψ_0 is the amplitude; k is the wave vector and ω is the angular or temporal frequency. The wave vector is of primary importance in waveguide calculations and its magnitude k is called spatial frequency. A wave having a single spatial frequency means that it is a plane wave (or highly spatially coherent).

1.4.2 Boundary conditions at dielectric interfaces

When light propagates through two different media which are adjacent to one another, the wave solutions in the two regions must be connected at the interface and the rules for these connecting solutions are called the boundary conditions. In general, if there is an index difference between the two media there will be a reflection which is called Fresnel reflection.

Consider the interface as shown in figure. The k vector which defines the direction of propagation of an electromagnetic wave propagates from one medium into another (accompanied by a partial reflection into the originating media).

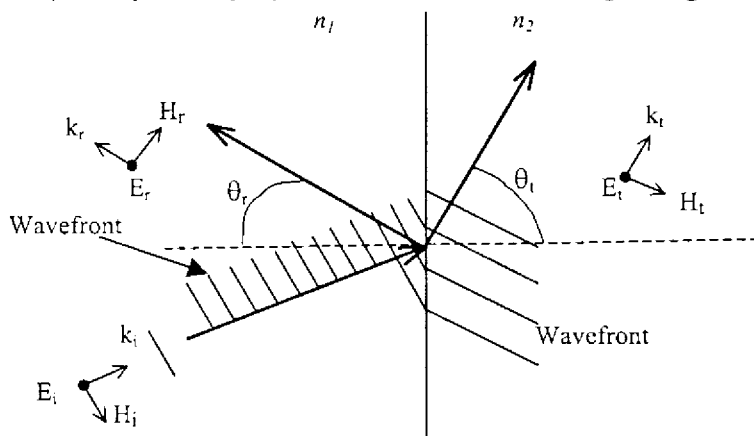


Figure 1.2: Light propagation through an interface between two media

In order to find out the transmission coefficient and the reflection coefficient, general solutions to the wave equations are assumed as

$$E_l(r, t) = E_l e^{-i(k_r \cdot r - \omega t)} \quad (1.10)$$

The subscript l refers to the three different fields that will arise. This gives the three components as

$$\bar{E}_i(x, y, z, t) = \hat{x} E_i e^{-ik_0 n_1 (z \cos \theta_i - y \sin \theta_i)} e^{i\omega t} \quad (1.11)$$

$$\bar{E}_t(x, y, z, t) = \hat{x} E_t e^{-ik_0 n_2 (z \cos \theta_t - y \sin \theta_t)} e^{i\omega t} \quad (1.12)$$

$$\bar{E}_r(x, y, z, t) = \hat{x} E_r e^{-ik_0 n_1 (-z \cos \theta_r - y \sin \theta_r)} e^{i\omega t} \quad (1.13)$$

The boundary conditions that apply to this situation can be derived from the integral form of Maxwell's equations. In a source free medium

$$\hat{n} \times (\bar{E}_2 - \bar{E}_1) = 0 \quad ; \text{ tangential components of } \bar{E} \text{ are continuous.} \quad (1.14)$$

$$\hat{n} \times (\bar{H}_2 - \bar{H}_1) = 0 \quad ; \text{ tangential components of } \bar{H} \text{ are continuous.} \quad (1.15)$$

$$\hat{n} \cdot (\bar{B}_2 - \bar{B}_1) = 0 \quad ; \text{ normal component of } \bar{B} \text{ is continuous.} \quad (1.16)$$

$$\hat{n} \cdot (\bar{D}_2 - \bar{D}_1) = 0 \quad ; \text{ normal component of } \bar{D} \text{ is continuous} \quad (1.17)$$

where \hat{n} refers to the unit normal to the interface. There are two possible excitations for the electric field with respect to the interface. The field can be either perpendicular (transverse electric, TE, or S-polarized) or parallel (transverse

$$R^{\text{TE}} = \frac{E_r}{E_i} = \frac{n_1 \cos \theta_i - n_2 \cos \theta_t}{n_1 \cos \theta_i + n_2 \cos \theta_t} \quad (1.18)$$

magnetic, TM, or p-polarized) to the plane of incidence which contains both \hat{n} and \bar{k} .

This yields the reflection coefficient, R_{TE} and the transmission coefficient T_{TE}

$$T^{TE} = \frac{E_t}{E_i} = \frac{2n_1 \cos \theta_i}{n_1 \cos \theta_i + n_2 \cos \theta_t} \quad (1.19)$$

For p-polarization correspondingly

$$R^{TM} = \frac{E_r}{E_i} = \frac{n_1 \cos \theta_t - n_2 \cos \theta_i}{n_1 \cos \theta_i + n_2 \cos \theta_t} \quad (1.20)$$

$$T^{TM} = \frac{E_t}{E_i} = \frac{2n_1 \cos \theta_i}{n_1 \cos \theta_i + n_2 \cos \theta_t} \quad (1.21)$$

1.4.3 Total internal reflection and evanescent wave

Consider a TE plane wave polarized along the x-axis with amplitude E_0 incident on a dielectric interface shown. The angle of incidence is less than the critical angle, θ_c . Only the spatial description of the two waves are considered as the phenomenon is independent of time.

$$\bar{E}_1(y, z) = \hat{x}E_0 e^{-ik_0 n_1 (z \cos \theta_i - y \sin \theta_i)} e^{i\alpha x} \quad (1.22)$$

$$\bar{E}_2(y, z) = T^{TE} \hat{x}E_0 e^{-ik_0 n_2 (z \cos \theta_t - y \sin \theta_t)} e^{i\alpha x} \quad (1.23)$$

The angles θ_i and θ_t are related by Snell's law as

$$\sin \theta_2 = \frac{n_1}{n_2} \sin \theta_1 \quad (1.24)$$

$$\cos \theta_2 = \sqrt{1 - \frac{n_1^2}{n_2^2} \sin^2 \theta_1} \quad (1.25)$$

Substituting into equation (1.23) we get an expression for the transmitted amplitude \bar{E}_2

$$\bar{E}_2(y, z) = T^{TE} \hat{x}E_0 e^{-ik_0 n_2 \left(z \sqrt{1 - \frac{n_1^2}{n_2^2} \sin^2 \theta_1} - y \frac{n_1}{n_2} \sin \theta_1 \right)} e^{i\alpha x} \quad (1.26)$$

Now consider the case when $\theta_i > \theta_c$. Then $\cos \theta_2$ becomes imaginary, so the transmitted electric amplitude is

$$\bar{E}_2 = T^{TE} \hat{x}E_0 e^{-k_0 n_2 z \sqrt{\frac{n_1^2}{n_2^2} \sin^2 \theta_1 - 1}} e^{-ik_0 n_2 y \frac{n_1}{n_2} \sin \theta_1} e^{i\alpha x} \quad (1.27)$$

This cumbersome form can be made compact as

$$\bar{E}_2 = T^{TE} \hat{x}E_0 e^{-\gamma z} e^{i\beta y} \quad (1.28)$$

and β represents the 'propagation coefficient'

$$\beta = k_0 n_1 \sin \theta_1 \quad (1.29)$$

where γ represents 'attenuation coefficient'

$$\gamma = k_0 n_2 \sqrt{\frac{n_1^2}{n_2^2} \sin^2 \theta - 1} \quad (1.30)$$

This exponentially vanishing field in (1.28) normal to the fiber axis outside the core is known as the evanescent field.

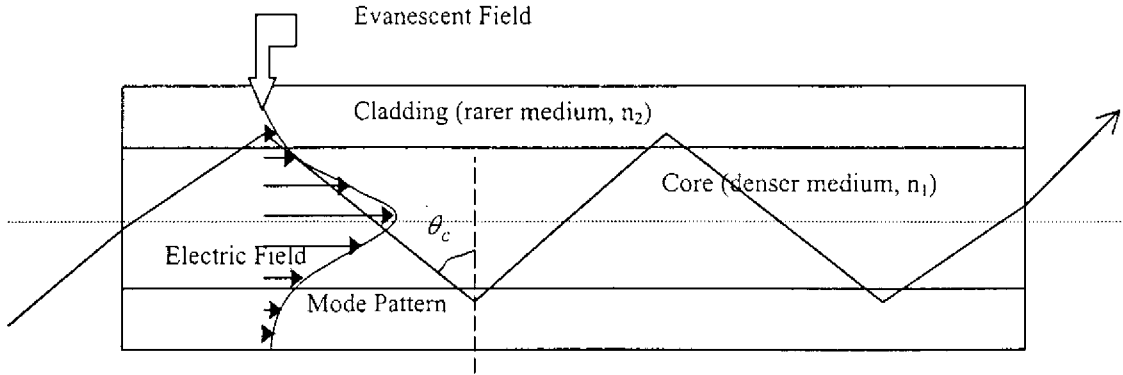


Figure 1.3: Light propagation through an optical fiber by Total Internal Reflection

1.5 Light propagation through an optical fiber

An optical fiber is a cylindrical dielectric waveguide that operates at optical frequencies. It confines electromagnetic energy in the form of light to within its surface by the phenomenon of TIR and guide the light in a direction parallel to the fiber axis.

1.5.1 Modes in an optical fiber:

The propagation of light in an optical fiber can be described in terms of a set of guided electromagnetic waves called the modes of the fiber. A mode in general represents a standing wave pattern of energy as observed in vibrating strings, resonance columns etc. Each guided mode is a pattern of electric and magnetic field distributions that is repeated along the fiber at equal intervals. For monochromatic light field of angular frequency ω , a mode traveling in the positive z direction (i.e. along the fiber axis) has a time and z dependence given by $e^{i(\alpha z - \beta t)}$

The factor β is the z component of the wave propagation constant $k=2\pi/\lambda$. For guided modes, β can assume only certain discrete values in the limit of $n_1 > \beta > n_2$, which one determines by the application of boundary conditions in the Maxwell's equations.

A guided mode traveling in z direction (along the fiber axis) can be decomposed into a family of superposed plane waves collectively form a standing wave pattern in the direction transverse to the fiber axis. In other words, the phases of the plane waves, which change as they travel along the fiber and after each reflection at the core cladding interface, are such that the envelope of the collective set of waves remains stationary. Since with any plane wave we can associate a light ray that is perpendicular to the phase front of the wave, the family of waves that correspond to a particular mode forms ray congruence. It can be seen that since each mode represents ray congruence with a particular value for angle of incidence, the above result restricts the values of the launching angle in to an optical fiber to a discrete number of finite values. This result is contrary to the ray optics approach, which predicts infinite number of angles between θ_c^0 and 90^0 . This discrepancy in the allowed values of β by using ray optics and wave optics is analogous to the case of classical and quantum mechanical results for bounded value problems.

The choice of a coordinate system to solve a particular problem depends on its symmetry. Therefore, rectangular Cartesian coordinate system is used to solve planar waveguide and cylindrical polar coordinate system for optical fibers. Similarly, the form of the solutions of Maxwell's equation for different types of modes also depends on the geometry of the waveguide. Planar waveguides, both dielectric and metallic gives transverse electric and transverse magnetic modes. However, in cylindrical fibers, the boundary condition lead to the coupling between the electric and magnetic field components to produce hybrid modes designated as HE and EH modes depending on whether the electric field (E field) or magnetic field (M field) has larger magnitude for that mode. Although the theory of light propagation is well understood, a complete description of the guided radiation modes that correspond to rays not satisfying TIR condition becomes rather complex. However, a further simplification is possible by using weakly guiding approximation i.e. $(n_1 - n_2) \ll 1$ which gives rise to linearly polarized (LP) modes.

1.5.2 Normalized frequency and normalized propagation constant:

A mode remains guided as long as β satisfies the condition $n_1 k > \beta > n_2 k$ where n_1 and n_2 are the refractive indices of the core and cladding respectively and $k = 2\pi/\lambda$. The boundary between the truly guided modes and unguided modes is defined by the cutoff condition $\beta = n_2 k$. The important parameter connected with the cutoff condition is the normalized frequency V (V number or V parameter) defined by

$$V = 2 \frac{\pi a}{\lambda} \text{NA} \quad (1.31)$$

and the normalized propagation constant is defined by

$$b = \frac{(\beta/k)^2 - n_2^2}{(n_1^2 - n_2^2)} \quad (1.32)$$

The number of modes propagating through a fiber, M is given by $M \sim V^2/2$ and the fiber becomes single moded when $V < 2.405$.

1.6 Single Mode Fibers:

Single mode fibers are constructed by letting the dimensions of core diameter be a few wavelengths (usually 8-12 μm) and by having small index differences between the core and the cladding. Light guiding in SMF can be understood based on diffraction effects which always cause divergence of a plane wave front (parallel beam of light). An optical fiber on the other hand tries to focus the wave because of the index differences between the core and the cladding. These two opposing effects cancel off thus making light guiding possible in the fiber. A fundamental parameter of a SMF is the mode field diameter (MFD). This parameter can be determined from the mode field distribution of the fundamental LP_{01} mode. MFD is analogous to the core diameter of the multimode fibers (MMF). Assuming the field inside the optical fiber to be gaussian,

$$E(r) = E_0 e^{-\frac{r^2}{\omega_0^2}} \quad (1.33)$$

where r is the radius, E_0 is the field at zero radius and ω_0 is the width of the electric field distribution. Usually $2\omega_0$ is taken as the MFD and can be obtained as

$$2\omega_0 = 2 \left[\frac{2 \int_0^{\infty} r^3 E(r) dr}{\int_0^{\infty} r E(r) dr} \right]^{1/2} \quad (1.34)$$

where $E(r)$ denotes the field distribution of the LP_{01} mode.

1.7 Concepts of fiber optic communication:

The major application of fiber optics is in telecommunication. About 400 million km of single mode fiber (SMF) has been laid as underground and under sea cables, out of which 1 million km is in India. It is estimated that 10 thousand km of fiber is laid every hour through out the world. In 2001, Alcatel demonstrated the transmission of 256 optical channels in a single fiber using DWDM technology at a rate of 10.2Tb/s which corresponds to an equivalent band width of 2.5 million phone calls. Today the technology has reached the third generation of fiber optic communication and strongly shifts towards the fourth generation which uses the DWDM technology.

Transmission of light by optical fibers is not 100% efficient. An optical signal transmitted through the fiber get attenuated as well as distorted (due to pulse dispersion). This signal degradation determines the maximum repeaterless separation between a transmitter and a receiver.

1.7.1 Attenuation:

Typical transmission loss in an optical fiber is 0.2 dB/km as against 5dB/km for copper cables. Furthermore, the signal loss in copper wires non linearly increases with modulation frequency. Attenuation determines the reduction in signal strength and is obtained by comparing output power with input power and is measured in the logarithmic unit of decibels (after Alexander Graham Bell) as

$$\text{Loss in dB} = -10 \cdot \log_{10}(\text{power out}/\text{power in})$$

Each optical fiber has a characteristic attenuation that is measured in decibels per kilometer (dB/km). The total attenuation (in dB) equals the characteristic attenuation times length. Different mechanisms responsible for attenuation in optical fibers are optical absorption in silica, linear and non-linear scattering and bending losses.

1.7.1.1 Optical absorption in Silica

After the famous work of Kao and Stocham, it was found that the major impurities that caused absorption loss in glass were OH ions and transition metal ions, such as iron, chromium, cobalt and nickel. The transition metal impurities that are present in

the starting materials with concentration levels of 1 to 10 ppb causes loss of 1 to 10 dB/km. Early optical fibers had high levels of OH ions that resulted in large absorption peaks. They occur at 1400, 950, 725 nm which respectively correspond to the first, second and third overtones of the fundamental absorption peaks of water near 2.7 μm . By reducing the residual OH content of fibers to around 1ppb, standard SMF have nominal attenuations of 0.5 dB/km at 1310 nm. The presence of germanium in the fiber core which is used to make an index difference between the core and cladding also causes some signal attenuation due to scattering. This may be reduced by the use of fluoride ions where fluoride ions are instead doped in the cladding for the guiding property of the fibers.

1.7.1.2 Scattering losses

Glass is made by fusing mixtures of metal oxides, sulfides or selenides. The resulting material is a randomly connected molecular network rather than a well defined ordered structure as found in crystalline materials. Scattering losses in glass wire result from these microscopic variations in the material density, from compositional fluctuations and from structural inhomogeneties or defects occurring during fiber manufacture. Whenever there is a refractive index variation over scales smaller than the wavelength of light, there arises Rayleigh scattering which is inversely proportional to the fourth power of wavelength. Structural inhomogeneties and defects created during fiber fabrication can also cause scattering of light out of the fiber. However, their size may be comparable to the wavelength of light propagated through the fiber and therefore the scattering is mainly due to Mie scattering.

Not only the above mentioned linear scattering processes occur in the fiber, but also nonlinear (or inelastic) scattering (NLS) processes arise in the fiber at moderate laser powers of 10 mW. The NLS process is an inelastic stimulated scattering process in which the optical field transfers part of its energy to the nonlinear medium. Two important nonlinear effects in optical fibers which are related to the vibrational modes of silica fall in this category;. These phenomena are known as stimulated brillouin scattering (SBS) in which an acoustic phonon is involved and

stimulated Raman scattering (SRS) in which an optical phonon take part. SBS is mainly exhibited as a backward scattering process whereas SRS takes place in all directions.

1.7.2 Dispersion:

Low attenuation alone is not enough to make optical fibers invaluable for telecommunications. They should also have high information capacity (or bandwidth). Optical fiber communication uses digital signals as pulses of light because they are less liable for distortion than analog signals. It is observed that these pulses undergo broadening in time as they propagate along the fiber. Such a broadening of the optical pulse is known as dispersion. In optical fibers it is of two types, inter modal dispersion and intra model dispersion (or group velocity dispersion) subdivided into material dispersion and waveguide dispersion. All these dispersion effects are due to the variation in the time taken by the different frequency components (both spatial as well as temporal) of a light pulse to cover a given length of the fiber. Intermodal dispersion arises due to difference in the time taken by the different modes (i.e. spatial frequencies) in a step index fiber to travel through the fiber and is therefore absent in graded index and single mode fibers. Material dispersion is a result of the variation of the refractive index of the core material as a function of the wavelength. This type of pulse spreading occurs even when different wavelengths follow the same path. In a single mode fiber, about 20% of the guided light travels through the cladding. Since the core and cladding have different indices of refraction, the pulse travel with different velocities though the core and cladding resulting in what is known as the waveguide dispersion. This type of dispersion is negligible in multimode fibers.

1.7.3 Innovative technology

The second generation of fiber optic communication system uses a single mode fiber at a wavelength of $1.31 \mu\text{m}$ which corresponds to the zero dispersion region in an optical fiber. The zero dispersion region is a result of the cancellation of waveguide dispersion and material dispersion. Eventhough the lowest wavelength attenuation

wavelength in the fiber occurs at $1.55\mu\text{m}$, the fiber has finite dispersion there. Therefore, in order to minimize the dispersion at $1.55\mu\text{m}$, new fiber geometries are used to fabricate dispersion-shifted fibers (DSF). One problem with the usage of DSFs is the wastage of already laid SMFs that operate at $1.31\mu\text{m}$. Therefore a new type of fiber called the Dispersion compensating fiber (DCF), which has an opposite dispersion characteristic compared to a SMF so that it can be used in conjunction with a SMF, is also getting some attention. The most recent development envisages the use of dispersion-flattened fibers to use multiple wavelengths as carriers in a single fiber using the DWDM technology.

1.8 Fiber optic Sensors:

Fiber Optic Sensors (FOS) represent a technology base that can be applied to myriad varieties of applications [19-35]. According to J P Dakin, "A sensor can be defined as a device which has the role of connecting a change in magnitude of one physical parameter into a change in magnitude of a second parameter which can be measured more conveniently and perhaps more accurately". In recent years, the scope of optical sensing techniques has made a quantum leap with the availability of low loss fibers and associated optoelectronic components. During early seventies, when the technology of fiber optic communication was evolving, the transmission characteristic of the fiber was found to be liable to change with external perturbations like bends, microbends, pressure, temperature etc.

Capitalizing on this observation of exceptional sensitivity of optical fibers to external perturbations, an alternate school of thought began to exploit this sensitivity of optical fibers to construct a large variety of sensors. This offshoot of optical fiber communication (OFC) soon saw a flurry of R&D activity around the world, which led to the emergence of the field of FOS and devices. The main advantage of FOS is the inherent property of an optical fiber to act as both sensing arm and signal transmission medium. Some of the key features of this new technology, which offers substantial benefits as compared to conventional electronic sensors, are

1. Sensed signal is immune to EMI and RFI

2. Intrinsically safe in explosive environments.
3. Highly reliable and secure with no risk of fire/sparks.
4. High Voltage insulation and absence of ground loops and hence obviate any necessity of isolation devices like optocouplers.
5. Low voltage and weight, for example one kilometer of 200 μ m silica fiber weighs only 70 gm and occupies a volume~ 30cm³.
6. As a point sensor, they can be used to sense normally inaccessible regions without perturbation of the transmitted signal.
7. Potentially resistant to nuclear or ionizing radiations.
8. Can be easily interfaced with low loss optical fiber telemetry and hence affords remote sensing by locating the control electronics for LED/lasers and detectors away from the sensor head.
9. Large bandwidth and hence offers possibility of multiplexing a large number of individually addressed point sensors in a fiber network or distributed sensing i.e. continuous sensing along the fiber length.
10. Chemically inert and they can be readily employed in chemical process and biomedical instrumentation due to their small size and mechanical reliability.

1.9. Classification of fiber optic sensors

Broadly, FOS may be classified as either intrinsic (active) or extrinsic (passive). In an intrinsic sensor, the physical or chemical parameter/effect (measurand) to be sensed modulates the transmission properties of the sensing fiber whereas in an extrinsic sensor, the modulation takes place outside the fiber, making fiber to just act as a carrier of the optical signal. The intrinsic sensor is again classified based on which of the characteristics of the electromagnetic field viz. amplitude/intensity, phase, polarization, wavelength or frequency, is modulated by the measurand.

The electric field of light can be written as

$$\vec{E}(x, y, z, t) = \vec{E}_0 e^{-i(k \cdot r - \omega t)} \quad (1.35)$$

The modulation of various parameters that represent the optical field forms the basis for different class of sensors shown below.

$\overline{E}(x, y, z, t)$	Amplitude	Intensity modulated sensors
\overline{E}_o	Polarization	Polarimetric sensors
$(k.r - \omega t)$	Phase	Interferometric sensors
k	Wave vector	Wavelength modulated sensors
ω	Angular frequency	Frequency modulated sensors.

1.9.1 Intensity modulated FOS (IMFOS)

Almost all of the extrinsic and some of the intrinsic FOS involve intensity modulation. In IMFOS, the measurand changes the intensity of light coming at the receiving end of the fiber. IMFOS are the simplest and most economical, even though they have low sensitivity which makes them the most widely studied of all the FOS. Reports of thousands of IMFOS may be found in literature, but the basic design may only be a few such as microbend and macrobend loss, moving masks, evanescent wave absorption etc.

1.9.1.1 Misalignment loss sensors

It is well known that coupled light intensity across a fiber joint is liable to vary through transverse, longitudinal or angular misalignments or through a combination of them between the axes of the two fibers.

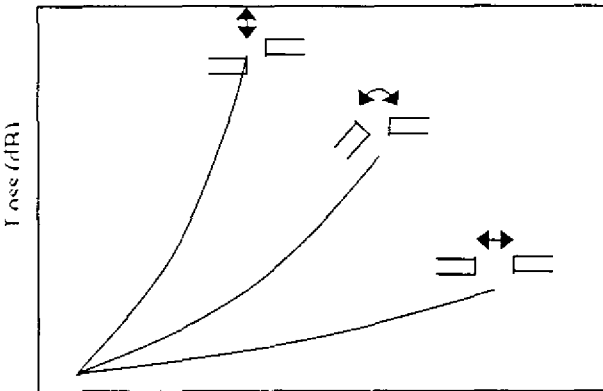


Figure 1.4: Various types of fiber misalignment losses

Fig 1.4 is a representation of the transmission loss versus misalignments along any three orientations between two 50 μ m quasi parabolic graded index multimode fibers.

Here the loss on dB scale is calculated relative to intensity transmitted across the joint for zero misalignment between fiber axes. The longitudinal displacement of one fiber relative to the other can be used to measure the axial displacement. On the other hand, it is apparent from the figure that joint loss is also sensitive to transverse misalignments between their axes. This phenomenon can be exploited to configure an a.c. pressure or an acoustic sensor in which two fiber and faces are kept close to each other whose axes are otherwise well aligned.

1.9.1.2 Shutter/Schlieren multimode FOS

In this type of extrinsic FOS, light intensity from one fiber to another is modulated by a shutter which is actuated by the measurand as shown in fig 1.4. A grating can also be used instead of the shutter. Here the sensitivity of the sensor is enhanced by the reduction in the width of the grating element at the expense of a corresponding decrease in the overall dynamic range.

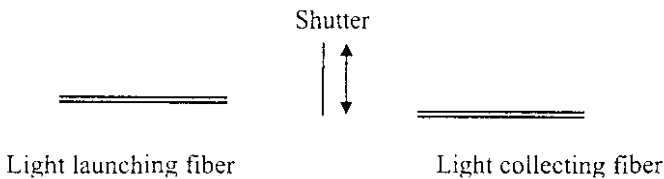


Figure 1.4: Shutter multimode FOS

1.9.1.3 Microbend loss sensors

Microbend loss has always been an undesirable effect causing problems in fiber optic communication links. However, this phenomenon has been exploited profitably in the fabrication of a variety of fiber optic sensors to measure pressure, temperature, displacement, electric field, chemical detection etc. In fact, fiber optic hydrophone is one of the earliest of FOS. Essentially, microbend sensors are based on coupling and leakage of modes that propagating in a deformed fiber.

1.9.1.4 Evanescent wave sensors

Although electromagnetic radiation that strikes the core-cladding interface of a multimode optical fiber at angles greater than the critical angle is totally internally

reflected, there is an electromagnetic field, called the evanescent wave that penetrates a small distance into the cladding. Such a wave which decays exponentially from the core-cladding interface and propagating parallel to it, can interact with the species surrounding the core region where the cladding has been stripped off. These species can absorb the evanescent field which gives rise to the phenomena of attenuated total internal reflection (ATR) and the optical power at the output end will be correspondingly reduced.

1.9.2 Phase modulated interferometric sensors

Phase modulation of light as a highly sensitive monitor of environmental changes has been increasingly exploited over the past hundred years. The principal attraction of optical phase modulation is its intrinsically high sensitivity to make a very high-resolution measurement possible as well as their large dynamic ranges. The incorporation of optical fibers into interferometers was initially suggested for the Sagnac rotation sensor. Generally, the sensor employs a coherent light source, the light from which is split and fed to two single mode fibers, and again recombined to produce interference fringes. If the environment perturbs one fiber relative to the other, a phase shift occurs and that can be detected precisely by an interferometric configuration so that phase variation can be transformed into an intensity variation. The various interferometers used are the Mach-Zehnder (MZ), the Michelson, the Fabry-Perot (FP) and the Sagnac of which the Mach-Zehnder and the Sagnac are the most widely used. They are mainly employed in hydrophone and gyroscope applications respectively. The FP is the most sensitive of all interferometers. The advantages of using fibers in interferometric sensors lie both in easing the alignment difficulties inherent in assembling interferometers with long arms and in increasing the sensitivity of the phase modulation to the environmental parameters simply by increasing the optical path length exposed to the measurand.

1.9.2.1 Phase detection

The phase angle, φ for a light wave with a given wavelength, λ and length, L is given by

$$\varphi = \frac{2\pi\lambda}{L} \quad (1.36)$$

This means that a change in phase can be brought about by a change in length or change in refractive index. It may be noted from fig 1.5 that the maximum sensitivity of the device will be at the quadrature point.

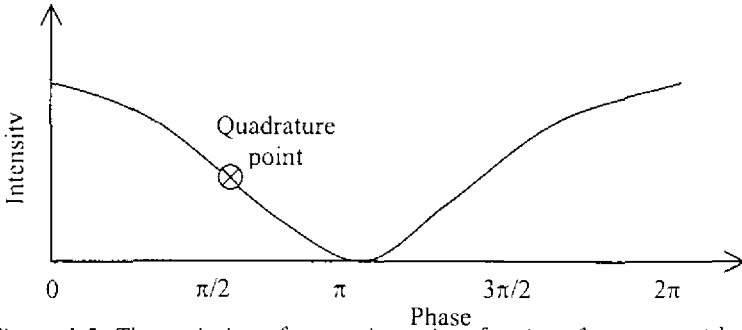


Figure 1.5: The variation of output intensity of an interferometer with respect to phase difference of the two arms of the interferometer

1.9.2.2 Mach-Zehnder interferometer

A schematic of the MZ interferometers is given in fig 1.6. If the path length of the sensing and reference fibers are exactly the same length or differs by an integral number of wavelengths, the recombined beams are exactly in phase and the beam intensity is at its maximum. However if the two beams are one half wavelength out of phase, the recombined beam is at its minimum value. A modulation of 100% occurs over half wavelength of light change in fiber length. This much sensitivity allows movements as small as 10^{-15} m to be detected.

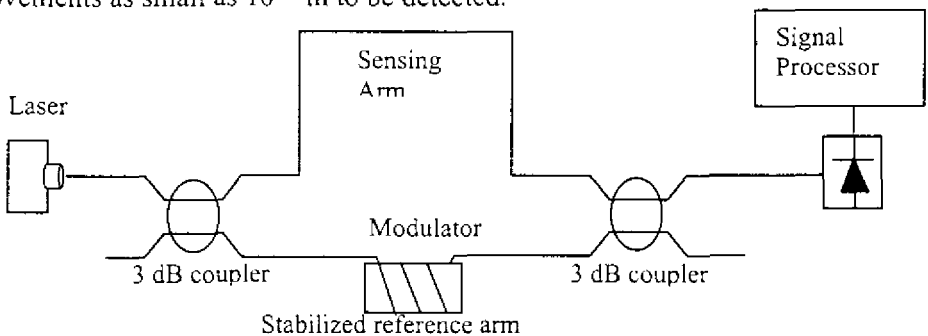


Figure 1.6: Fiber optic Mach-Zehnder interferometer

1.9.2.3 Michelson Interferometer

This configuration is similar to the MZ interferometer configuration except the use of only a single coupler instead of two in MZ and the use of two mirrors as shown in fig

1.7. For the Michelson interferometer a path length difference of $\frac{1}{4} \lambda$ in fiber length results in $\frac{1}{2} \lambda$ path length change due to the second pass of the reflected beam. The comparison of the MZ and the Michelson interferometers is somewhat analogous to the comparison of transmissive and reflective intensity modulated sensors.

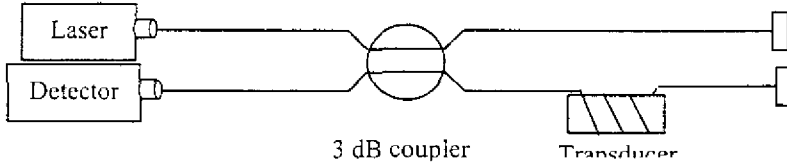


Figure 1.7: Fiber optic Michelson interferometer

1.9.2.4 Fabry-Perot Interferometer

Here the interference results from successive reflection of the initial beam as shown in fig 1.8. The multiple passes along the fiber magnify the phase difference, which results in extremely high sensitivity. Generally, the FP sensor has twice the sensitivity of the other interferometers discussed. A typical FP interferometer is shown.

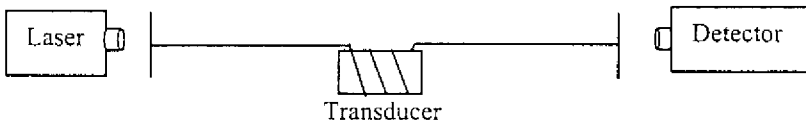


Figure 1.8: Fiber optic Fabry-Perot interferometer

1.9.2.5 Sagnac Interferometer

The major advantages of fiber optic gyroscopes over mechanical devices include: no moving parts, no warm-up time, unlimited shelf life, minimal maintenance, large dynamic range and small size. Most of the applications are in military, automobile industry and aviation.

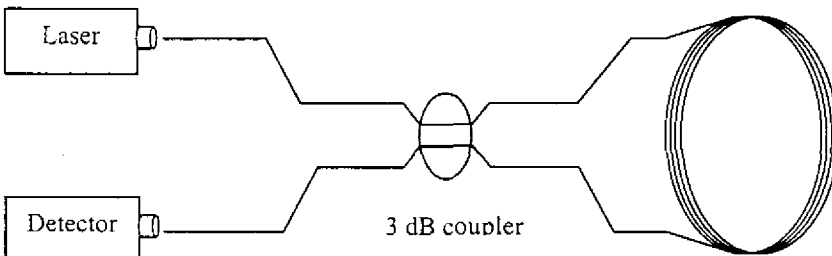


Figure 1.9: Fiber optic Sagnac interferometer

A beam is split into two by a coupler and allowed to travel in a fiber in coiled configuration as shown in the fig 1.9. One path is clockwise and the other anticlockwise. When the fiber is not rotating, both beams take same amount of time T , to complete one closed path. If the fiber rotates clockwise, then the clockwise beam takes longer time whereas the anticlockwise beam takes lesser time to complete one complete closed path, than the time they would have taken under stationary conditions. In other words, in a given time say T , the light beam effectively covers two distances, the clockwise beam covers $2\pi R + \Delta S$ while the anticlockwise beam covers $2\pi R - \Delta S$. This path difference results in a phase difference which is given by

$$\Delta L = 2\Delta S \quad (1.37)$$

$$\Delta L = c\Delta T = 4A\Omega/c \quad (1.38)$$

where ΔT is the time difference, A is the area of the coil given by, $A = \pi D^2/4$, D is the coil diameter, Ω is the angular velocity of the coil and c the velocity of light.

For a coil with N turns

$$\Delta L = 4AN\Omega/c \quad (1.39)$$

Substituting $N = L/\pi D$ and for A we get

$$\Delta L = \left(\frac{LD}{c} \right) \Omega \quad (1.40)$$

Usually a spatial filter and polarizer are used in the gyroscope to ensure that it is not affected by any external unwanted perturbation which also creates a path difference between the two beams.

1.9.3 Polarimetric sensors

Polarization plays an important part in a variety of optical fiber systems, especially those in which single mode fibers are involved. An understanding of the role of polarization in fiber systems and the means, Stokes parameters, Jones matrix and Poincare sphere representation, by which polarization properties may be characterized are of central importance.

A single mode fiber itself is capable of transmitting light in two orthogonal modes (HE_{11x} having a propagation constant β_x and HE_{11y} with $\beta_y = \beta_x$). Eventhough light is launched only to one of these modes, power coupling takes place between these

modes due to the irregularities present in the fiber in the form of refractive index variations (axial as well as azimuthal) or physical deformations such as deviation from perfect circular geometry. Therefore, in almost all the polarimetric sensors, polarization-maintaining fibers (PMFs) are used so that the polarization modulation can be easily detected. Intentionally in this type of fibers, the propagation constants are so chosen that $\beta_y \neq \beta_x$. Basically, there are two types of PMFs; high birefringent (HiBi) fibers and low birefringent (LoBi) fibers depending on the magnitude of $(\beta_y - \beta_x)$.

Usually a circularly polarized light is launched into the optical fiber in order to excite both eigen modes equally. The state of polarization at the output is determined using wollastom prism or Soleil-Babinet compensator or a simple analyzer, which varies in accordance with the measurand. This is because when a birefringent fiber is subjected to a lateral stress, the beat length

$$L_b = \frac{2\pi}{\beta_y - \beta_x} \quad (1.41)$$

and the birefringent axes of the stressed fiber are changed relative to an unstressed one. As a result coupling of power between the orthogonal polarization states takes place. By monitoring the output at the analyzer the amount of stress or pressure can be measured.

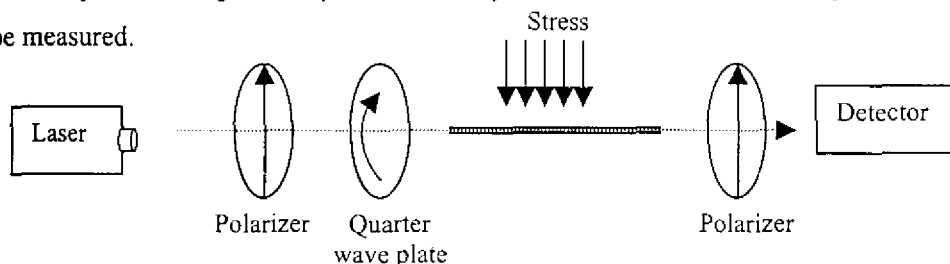


Figure 1.10: Schematic diagram of a typical fiber optic polarimetric sensors

Optical activity and Faraday effect are two other mechanisms by which the state of polarization of a linearly polarized light is rotated and hence used with optical fibers to have various sensors that detects chemical species, measure electric and magnetic fields etc. It should be noted, however, that, the objective here is not to have a complete understanding of the state of polarization of the output light.

1.9.4 Frequency modulated sensors

Frequency modulation of light occurs under a limited range of physical conditions. Different effects like Doppler effect, Brillouin scattering, Raman scattering etc. are used in these types of sensors. In Doppler effect, if a radiation at a frequency f is incident upon a body moving at a velocity v , then the radiation reflected from the body appears to have frequency f_1

$$f_1 = \frac{f}{1 - v/c} = f \left(1 + \frac{v}{c} \right) \quad (1.42)$$

Doppler shifts provide a very sensitive detection of target motion. For instance, with He-Ne laser as the source, a frequency shift of 1.6 MHz per m/s of target motion is observed. Doppler velocimetry is widely used in applications such as flow measurement etc.

1.9.5 Wavelength modulated sensors

In this type of sensors, the change in value of measurand is converted to a variation in wavelength of light as in Bragg grating sensor. Bragg gratings can be created in a fiber by periodic modulation of the core refractive index of the fiber. When light from a broadband source is transmitted through such a fiber, some wavelengths are not allowed to pass through the core of the fiber, thus forming dips at certain wavelengths in the transmission spectrum of the fiber. On the application of temperature and/or pressure there will be a shift in the dip wavelength that eventually forms the basis of wavelength modulated fiber optics sensors.

1.10 Major areas of application of fiber optic sensors

Depending on the area of application of FOS, they are divided into medical or biomedical, chemical, environmental, interferometric gyros or hydrophones, smart structures and electrical. They are extensively used in pollution monitoring, structural monitoring, automobile industry, blood analysis etc. Following are the major areas of application of FOS.

1.10.1 Chemical, biochemical and biomedical applications

FOS used in chemical, biochemical and biomedical applications are mostly of the intensity modulated type, which employ optical spectroscopy as the basic tool. In this

respect two basic approaches are possible: either direct optical interaction with the analyte or indirect analysis using chemical indicators which are compounds that change their optical properties on reaction with the analyte. Both approaches have their merits and demerits. Eventhough, the direct spectroscopic method is non-destructive to the sample under test and is usually very rapid, it is not as selective as indicator chemistry.

1.10.1.1 Liquid phase sensing

Many liquid-sensing applications may be carried out using extension-leads from a commercial spectrophotometer. Some manufacturers now sell such attachments as optional extras for their commercial products. The measured spectra can be used for the simultaneous detection of several absorbing solutes by using multivariate analysis methods.

1.10.1.2 Transmission spectroscopy

This technique has found wide applications in chemical, biological and environmental monitoring and process control due to its generic nature, intrinsic safety and ease of applications. In this technique, any change in the parameters of the analyte modulates the properties of the beam propagating through it. For example for a simple fiber optic probe, changes in the refractive index of the analyte can modify the output light cone angle to different extent at the reference wavelength than at the measurement wavelength.

1.10.1.3 Evanescent wave spectroscopy

Here, an unclad fiber is placed inside an analyte, the light passing through which will be modified through evanescent wave phenomena. Details are given in Chapter 2.

1.10.1.4 Fluorescence spectroscopy

Remote monitoring of sample fluorescence via optical fiber is a long-standing in situ monitoring technique. Measurements made by fiber probes can provide qualitative and quantitative information, with an additional degree of selectivity provided by the choice of excitation wavelength and the fluorescent lifetime of a particular analyte.

Although broadband sources can be used to produce fluorescence, lasers are usually preferred for use with optical fibers.

1.10.1.5 In vivo medical sensors

Among the advanced technologies in health care, fiber optics is a major contributor to the development of advanced diagnostic and therapeutic techniques. Fiber optic methods are providing ideal, not only for intra-cavity imaging and safe laser delivery for angioplasty, but also for monitoring critical physiological parameters mainly because of the following reasons.

- ❖ Unclad fibers are so small and flexible that they can be inserted inside very thin catheters and hypodermic needles, thereby ensuring highly localized and minimally invasive monitoring.
- ❖ Fibers are not toxic, chemically and electromagnetically inert and intrinsically safe for the patient.
- ❖ Since cross talk is absent in fibers, several sensing fibers can be grouped in a single catheter.

In vivo medical applications include oximetry of circulatory-respiratory systems, blood gases like CO₂, blood pH, respiration monitoring, angiology, gastroenterology, ophthalmology, oncology, neurology, dermatology etc.

1.10.2 Fiber optic gyros

In the family of FOS, the fiber optic gyro (FOG) has become the most sophisticated type. It provides a rotation detection function with respect to an inertial frame. FOGs have been extensively studied and developed for about 20 odd years. The first generation of FOG called interferometer FOG (I-FOG) has been successfully used in aircraft navigation like the one in Boeing-777, rocket control and ship navigation. The FOGs have several advantages over the traditional spinning mass gyros, in particular short warm-up time, light weight, low power consumption, wide dynamic range, large power benefit an low cost.

1.10.3 Condition monitoring and engineering diagnostics

For condition monitoring and engineering diagnostics, optical measurement techniques have performed a special role. The ability to operate without contacting or mechanically loading the measurement volume is their most powerful advantage. Some of the measurands determined using this technique include optical path length, velocity, vibration, electric and acoustic measurements. FOS are extensively used in surface profiling, laser Doppler anemometry (LDA), thermal measurements, electronic speckle pattern interferometry (ESPI), sheorography etc.

1.10.4 Distributed sensors

Distributed sensing, a unique property of FOS, involves the measurement of measurands at various positions along the fiber length. The only contact between the point to be measured and the observation area is the optical fiber. The read-out is usually done by a optical time domain reflectometer (OTDR) from which the signal is processed to produce the value of the parameter of interest as a function of linear position. The time domain reflectometer usually gives a value of the intensity of the returned signal as a function of time. The basic mechanism by which an OTDR works is that when light propagates through a fiber, scattering occurs in all directions which causes some light to be back reflected to the source and the time required for this signal is a function of time (or position = velocity of light * time). In distributed sensing both linear (Rayleigh) and nonlinear (Brillouin and Raman) scattering can be used.

In principle, it is possible to determine the value of a wanted measurand continuously as a function of position along the length of the fiber, with arbitrarily large spatial resolution. Additionally the temporal variation is determined simultaneously. Such a facility opens up a myriad number of possibilities for industrial application. For example, it would allow the spatial and temporal strain distributions in large critical structures such as multi-story buildings, bridges, dams, aircraft, pressure vessels, and electrical generators and so forth to be monitored continuously. It would allow the temperature distribution in boilers, power

transformers, power cables, airfoils, and office blocks to be determined. Electrical and magnetic field distribution could be mapped in space so that electromagnetic (EM) design problems would be eased and source of EM interference would be quickly available.

1.10.5 Fiber optic smart structures

In recent years, a new interdisciplinary field called smart structures has emerged from a synergistic combination of research in designed materials, and advanced sensing, actuation and communications, and artificial intelligence. The aim of this field is the creation of active structures that perform better and cost less than their passive counterparts designed for the same purpose. A smart structure will adapt to changes in its environments and its internal state, to optimize itself in order to achieve some purpose. The field of smart structures began in the early 1980s by developing radar antennas that were conformally integrated into the skins of military aircraft. Since that time, civil, marine, automotive and other structures have been the subject of smart structures research.

In the near term, smart structures can have a significant impact in two areas. The first of these involves high-performance composite structures fabricated from the new designed materials while the second involves the design, construction and maintenance of large civil structures such as rails, bridges, roads and dams.

The following chapters describe the design and fabrication of some fiber optic sensors for various physical and chemical applications.

REFERENCE:

1. V P N Nampoory, *Dream Merchants – History of Fiber Optics*, <http://www.photonics.cusat.edu/Article1.html>
2. M Shelly John, *Evanescence Wave Fiber Optic Sensors: Design, Fabrication and Characterization*, Ph. D. thesis, Cochin University of Science and Technology, India.
3. A K Ghatak and K Thyagarajan, *Introduction to Fiber Optics*, Cambridge University Press, New Delhi (1999)
4. A K Ghatak and M R Shenoy, *Fiber Optics through Measurements*, Viva Books, New Delhi (1994)
5. A K Ghatak, A Sharma and R Tewari, *Fiber Optics on a PC*, Viva Books, New Delhi (1994)
6. G P Agarwal, *Nonlinear Fiber Optics (II Ed.)*, Academic Press, San Diego (1995)
7. G Keiser, *Optical Fiber Communications (III Ed.)*, McGraw Hill, Boston (2000)
8. J M Senior, *Optical Fiber Communications (II Ed.)*, Prentice Hall India, New Delhi (2001)
9. J C Palais, *Fiber Optic Communications (IV Ed.)*, Pearson Education, New Delhi (2001)
10. S D Personick, *Fiber Optics - Technology and Applications*, Plenum Press, New York (1988)
11. A H Cherin, *An Introduction to Optical Fibers*, McGraw Hill, Auckland (1983)
12. J Hecht, *Understanding Fiber Optics*, Prentice Hall, New Jersey (1993)
13. C R Pollock, *Fundamentals of Optoelectronics*, IRWIN, Chicago (1995)
14. J Wilson, J F B Hawkes, *Optoelectronics*, Prentice Hall India, New Delhi (1996)
15. J Powers, *Fiber Optic Systems*, McGraw Hill, Singapore (1999)
16. P Diamant, *Wave Transmission and Fiber Optics*, Macmillan Publishing, New York (1990)
17. D Derickson, *Fiber Optic Test and Measurement*, Prentice Hall, New Jersey (1998)
18. I P Kaminow and T L Koch, *Optical Fiber Communications IIIB*, Academic Press, San Diego (1997)
19. F de Fornel, *Evanescence Wave From Newtonian Optics to Atomic Optics*, Springer (1997)
20. B P Pal, *Fundamentals of Fiber Optics in Telecommunication and Sensor Systems*. New Age International, New Delhi (1992)
21. D A Krohn, *Fiber Optic Sensors – Fundamentals and Applications*, Instrument Society of America (1988)
22. B Culshaw, *Optical Fiber Sensing and Signal Processing*, Peter Peregrinus, London (1984)
23. B Culshaw and J P Dakin, *Optical Fiber Sensors – Vol III*, Artech House, Boston (1996)
24. J P Dakin and B Culshaw, *Optical Fiber Sensors – Vol IV*, Artech House, Boston (1996)
25. K T V Grattan and B T Meggitt, *Optical Fiber Sensor Technology*, Kluwer Academic Publishers, London (1998)
26. O S Wolfbeis, *Anal. Chem.* **74**, 2663 (2002)
27. A G Mignani and F Baldini, *IEEE J. Lightwave Technol.* **13**, 1396 (1995)
28. D A Jackson and J D C Jones, *Opt. Laser Technol.* **18**, 299 (1986)
29. I P Kaminow, *IEEE J. Quantum Electron.* **QE-17**, 15 (1981)

30. Y N Ning, Z P Wang, A W Palmer and K T V Grattan, *Rev. Sci. Instrum.* **66**, 3097 (1995)
31. E Udd, *Fiber Int. Opt.* **11**, 319 (1992)
32. F Ansari, *Cement and Concrete Composites*, **19**, 3 (1997)
33. D A Jackson, *Meas. Sci. Technol.* **5**, 621 (1994)
34. D A Jackson, *J. Phys. E: Sci. Instrum.* **18**, 981 (1985)
35. P A Payne, *J. Phys. E: Sci. Instrum.* **16**, 947 (1983)

Sensitive Fiber Optic pH Sensors Using Multiple Sol-Gel Coatings

Introduction

One of the most commonly monitored chemical parameter of a fluid is its pH value. Different types of pH sensors like indicator strips, pH electrodes etc. are now easily available for commercial use. Notwithstanding their wide distribution, pH electrodes suffer certain limitations such as (a) they require a reference electrode, (b) the liquid-liquid junction of the electrode can easily be perturbed by external factors, (c) the signal can be subjected to electrical interferences, (d) they are expensive and (e) they cannot be easily miniaturized.

The concept of immobilizing an indicator dyestuff, whose color change might be used to observe variation in pH, dates back at least to the use of litmus paper. The integration of this principle with fiber optic techniques represents an important extension of pH measurement that can complement and improve conventional potentiometric methods. Fiber optic pH sensors are extensively developed for various physiological applications [1-3] like brain pH monitoring [4], blood pH and gas (O_2 and CO_2) monitoring and gastric pH sensing, because of their miniature size, intrinsically inert and rugged nature and immunity to all kinds of interferences. A notable advantage is that they do not require a reference electrode for the pH

measurement. Moreover, unlike the conventional potentiometric electrodes they can be used for on-line monitoring of pH, especially in-situ and in-vivo measurements. Such optrodes are frequently used in all kinds of hazardous environments such as deep-water analysis, chemical reactors or wastewater monitoring.

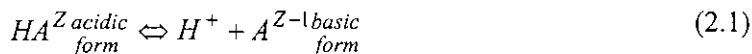
Most of the fiber optic pH sensors are of the intrinsic variety. Different portions of the optic fiber can be used for sensing, such as the end face or the core-cladding interface. In addition, various phenomena like optical absorption, reflection or fluorescence can be exploited for the sensor fabrication. The use of optical absorption at the core-cladding interface has paved the way for a relatively new class of sensors known as the evanescent wave fiber optic sensors (EWFS) [5-38].

All fiber optic pH sensors are based on the reagent mediated sensing technique where a fluorophoric or chromophoric dye is immobilized on an optical fiber and the recorded fluorescence signal [1,2] or color change [3,4] accounts for the concentration of H^+ of the element of interest. pH indicators (represented by HA^z) are mostly weak acids (less often, weak bases) whose color or fluorescence is different in the dissociated, A^{z-1} and the associated (protonated) form, HA^z [39]. The fact that optical pH sensors can only measure over a limited range of pH is disadvantageous but inevitable. No single indicator is available that allows measurements to be performed over the pH range of 1 to 13, as electrodes do. Rather, different indicators have to be employed. The most important range is the one in the near neutral (physiological) pH range. However, only a few indicators meet the requirements for use in pH sensors for physiological samples.

2.1 Theory

2.1.1 Spectrophotometry

The development of the present fiber optic probe is basically an extension of the spectrophotometric determination of pH. A pH indicator dye HA^z which is usually a weak acid or a weak base, entrapped in solution or sol-gel matrix will exist in two



forms as H^+ and A^{z-1} . The acidic form and basic form of the dye have absorption peaks at two wavelengths; for example at 420 nm and 616 nm in the case of bromocresol green (BCG) dye. The optical absorption at a wavelength λ can be written as

$$A(\lambda) = \alpha_{\lambda}^A [A^{z-1}] * l + \alpha_{\lambda}^{HA} [HA^z] * l \quad (2.2)$$

A is the absorbance, α_{λ}^A and α_{λ}^{HA} are the absorption coefficients of basic and acidic forms of the dye, respectively. $[A^{z-1}]$ and $[HA^z]$ are the respective concentrations of the basic as well as the acidic forms of the dye and l is the length of interaction region of light with the dye. The rate constant of the pH dissociation in solution is given by

$$K_a = \frac{[H^+][A^{z-1}]}{[HA^z]} \quad (2.3)$$

An important parameter for characterization of a pH indicator is its pK_a value (i.e. the pH at which the dye is present in the undissociated and the dissociated form 50% each), which is the negative log of K_a .

2.1.2 Evanescent wave spectroscopy

To make the thesis self contained, an outline of the theory is provided in the following section. Although electromagnetic radiation that strikes the core-cladding interface of a multi-mode optical fiber at angles greater than the critical angle is totally internally reflected, there is a field, called evanescent field that penetrates to a small distance into the cladding. This evanescent wave, which decays exponentially from the core-cladding interface and propagating parallel to the fiber axis, can interact with the chemical species surrounding the core region where the cladding has been stripped off. If this evanescent wave is absorbed by the species surrounding the core region it gives rise to the phenomenon of attenuated total reflection (ATR) and therefore the output power of the optical fiber will be correspondingly reduced. In order to evaluate the expression involving evanescent wave absorption we review the theoretical approach developed by Gloge [5] and Kychakoff [6]. Let us consider a cylindrical optical fiber of core radius a and diameter d , with core refractive index n_{co}

and cladding refractive index n_{cl} which guides light along the z-direction. We define the parameters

$$U = a(k^2 n_{co}^2 - \beta^2)^{1/2} \quad (2.4)$$

$$W = a(\beta^2 - k^2 n_{cl}^2)^{1/2} \quad (2.5)$$

where β is the propagation constant of any mode of the fiber which is limited within the interval $n_{co}k \geq \beta \geq n_{cl}k$ where $k = 2\pi/\lambda$. The mode field can be expressed by Bessel function $J(Ur/a)$ inside the core and modified Hankel function $K(Wr/a)$ in the cladding.

The quadratic summation

$$V^2 = U^2 + W^2 \quad (2.6)$$

leads to a third parameter

$$V = \pi a / \lambda (n_{co}^2 - n_{cl}^2)^{1/2} \quad (2.7)$$

which is defined as the normalized frequency. By matching the fields at the core-cladding interface, we obtain characteristic functions $U(V)$ or $W(V)$ for every mode; so that the propagation constant and all other parameters of interest can be determined.

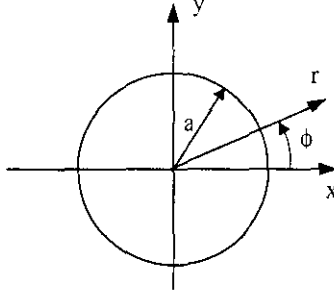
Maxwell's equations have exact solutions for light propagation through a dielectric cylinder, but even with the simplifying assumption that the cladding is infinitely thick, these solutions are too complicated to be evaluated without a computer. Therefore a weakly guiding approximation is taken where the parameter

$$\Delta = (n_{co} - n_{cl})/n_{cl} \quad (2.8)$$

is assumed to be much less than one, to solve the Maxwell's equations in an optical fiber. Under this approximation the various HE modes and EH modes can be approximated to linearly polarized (LP) modes.

The transverse field components of light inside the fiber in the Cartesian co-ordinate system is given by

$$E_y = H_x \begin{Bmatrix} Z_0/n_{co} \\ Z_0/n_{cl} \end{Bmatrix} = E_l \begin{Bmatrix} J_l(Ur/a)/J_l(U) \\ K_l(Wr/a)/K_l(W) \end{Bmatrix} \cos l\phi \quad (2.9)$$



Here, as well as in the following equations the upper line holds for the core and the lower line for the cladding; Z_0 is the plane wave impedance in vacuum, and E_l is the strength of the electric field component at the interface. Since we have the freedom of choosing either $\sin l\phi$ or $\cos l\phi$ in the previous equation and two orthogonal states of polarization exists, we can construct a set of four modes for every l as long as $l > 0$. For $l = 0$, we have only a set of two modes polarized orthogonally with respect to each other.

The longitudinal field components can be obtained as

$$E_z = \frac{iZ_0}{k} \begin{Bmatrix} 1/n_{co}^2 \\ 1/n_{cl}^2 \end{Bmatrix} \frac{\partial H_x}{\partial y}, \quad (2.10a)$$

and
$$H_z = (i/kZ_0)(\partial E_y/\partial x) \quad (2.10b)$$

Substituting the values of H_x and E_y from (2.9) we can obtain expressions for E_z and H_z , in terms of the Bessel functions and Hankel functions multiplied by factors U/ak and W/ak respectively. From (2.4) and (2.5) it is clear that both U/ak and W/ak are of the order of $\Delta^{1/2}$ which means that the longitudinal field components are negligibly small with respect to the transverse components and hence we can safely use the approximation that the fields inside an optical fiber are transverse with linearly polarized (LP) modes.

The characteristic equation, which matches all the tangential components at the interface for the LP modes, is given by

$$U \frac{J_{l-1}(U)}{J_l(U)} = -W \frac{K_{l-1}(W)}{K_l(W)} \quad (2.11)$$

The Bessel functions $J_l(U)$ are similar to harmonic functions since they exhibit oscillatory behavior for real k values. Hence there will be m roots for a given l value and each value represent a LP_{lm} mode. The different LP modes for $l=0,1$ and their corresponding real field pattern (EH, HE, TE or TM) are given in the fig 2.1.

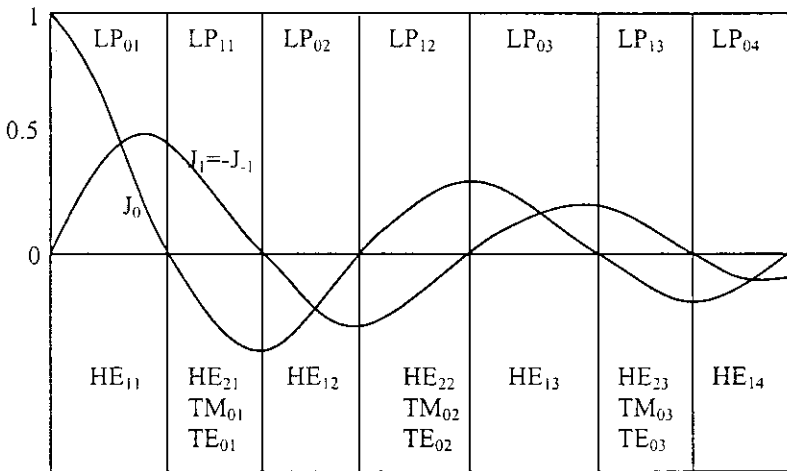


Figure 2.1: Field pattern of various LP modes

The Poynting vector in the axial direction can be calculated from the cross product of the transverse fields given in (9), the integration of which over the cross-section of core and cladding leads to the power in the core, P_{core} and P_{clad} respectively as

$$P_{core} = \left[1 + \left(\frac{w^2}{u^2} \right) \left(\frac{1}{\kappa_1} \right) \right] \left(\frac{\pi a^2}{2} \right) (Z_0 / n_{co}) E_l^2 \quad (2.12)$$

$$P_{clad} = \left[\left(\frac{1}{\kappa_1} \right) - 1 \right] \left(\frac{\pi a^2}{2} \right) (Z_0 / n_{co}) E_l^2 \quad (2.13)$$

where
$$\kappa_l = K_l^2(W)/K_{l+1}(W)K_{l-1}(W) \quad (2.14)$$

If we ignore the small difference between n_{co} and n_{cl} the total power in a certain mode becomes

$$P_{total} = P_{core} + P_{clad} = \left(\frac{u^2}{v^2}\right) \left(\frac{1}{\kappa_l}\right) \left(\frac{\pi a^2}{2}\right) \left(Z_0/n_{co}\right) E_l^2 \quad (2.15)$$

The fraction of the power flowing in the cladding for a linearly polarized (LP) mode of a step index optical fiber under the weakly guiding approximation

$$\eta_{lm} = \left(\frac{P_{clad}}{P_{total}}\right)_{lm} = (U^2/V^2)(1-\kappa_l) \quad (2.16)$$

$(1-\kappa_l)$ can be approximated to be

$$(1-\kappa_l) \cong (V^2 - U^2 + l^2 + 1)^{-1/2} \quad (2.17)$$

A simple estimate of η can be provided by considering a step-index fiber with large V number. With the total number of modes given by $N \propto V^2/2$, (2.16) can be integrated to yield

$$\eta = 4\sqrt{2}/(3V) = (4/3)N^{-1/2} \quad (2.18)$$

For a fiber with $V=100$, approximately 2% of the total power flows in the cladding and is therefore available for evanescent wave absorption which occurs when the material forming the cladding of the fiber absorbs light at the wavelength being transmitted. If the imaginary parts of the core and cladding refractive indices are small compared to the real parts, the power attenuation coefficient is given by

$$\alpha = (1-\eta)\alpha_{co} + \eta\alpha_{cl} \quad (2.19)$$

where η is the fraction of power flowing in the cladding, α_{co} is the core bulk absorption coefficient, and α_{cl} is the cladding bulk absorption coefficient. If the range of α_{cl} is small, then the power transmission through an optical fiber, having a lossy cladding can be approximated by the modified Beer – Lambert’s law,

$$P(l) = P_0 \exp(-\gamma z) \quad (2.20)$$

where z is the length of the lossy cladding or unclad portion of the fiber, P_0 is the power transmitted in the absence of an absorbing species and γ is the evanescent wave absorption coefficient. Since $\gamma = \eta\alpha$, the above equation can be rewritten as,

$$P(l) = P_0 \exp(-\eta\alpha z) \quad (2.21)$$

η is the fraction of the power transmitted through the cladding and α is the bulk absorption coefficient. It is (2.21) that helps us to develop an evanescent wave fiber optic sensor. Since $\alpha = \alpha(\lambda)$ one can have a spectroscopic measurement using evanescent waves.

2.2 Indicator immobilization techniques

Immobilization of pH indicators is a key step in the development of optical and fiber optic pH sensors, and will largely determine the characteristics of the sensors. There are three widely used methods for immobilization of a pH indicator on / in a solid substrate: adsorption, covalent binding and entrapment. In the adsorption method, a pH indicator is adsorbed physically or chemically, e.g. via electrostatic or hydrophobic interactions, on a solid substrate; it is simple but not very reliable since the adsorbed indicator may leach out. In the covalent binding method, a pH indicator is covalently bound on a solid substrate; it is usually complicated and time-consuming but very reliable since the indicator is not likely to leach out. In the entrapment method, a pH indicator is entrapped in a porous polymeric substrate; it is quite easy and reliable but is slow and indicator leaching can be a problem.

2.2.1 Immobilization by electrostatic interactions

Commercial ion-exchangers (such as Amberlite XAD1180, IRA400, IRA401 and Dowex-1) continue to be used for electrostatic immobilization of pH indicators [40-43]. Other materials were also developed, e.g. sulfonated polystyrene [44] and polyelectrolyte-containing silica [45]. In one study, it was found that the pH sensors thus developed could be used in solution with low concentrations of electrolytes but leaching of pH indicators became a problem at high concentrations of electrolytes [45]. In another study, the pH indicator was absorbed on an ion-exchanger and

entrapped in an organic copolymer [46], which should be considered an improved combination method.

2.2.2 Immobilization by hydrophobic interactions

Hydrophobic interactions (i.e. chemical adsorption) can be used for adsorption of hydrophobic pH indicators on hydrophobic organic polymers. Amberlite XAD2 and XAD4 resins have been used for immobilization of pH indicators [47-49]. Recently, Kuswandi and Narayanaswamy have developed a so-called 'polymeric encapsulated membrane', in which the pH indicator is first adsorbed on XAD4 resin which is then encapsulated within porous poly vinyl chloride (PVC) membrane [50]. By combining the adsorption and entrapment methods, the reagent leaching can be largely reduced or eliminated.

2.2.3 Cellulose for covalent binding and entrapment of pH indicators

Cellulose continued to be used widely in the development of pH sensors, particularly by Wolfbeis and co-workers [51-60]. It is believed to be an ideal support for pH indicators since it has a high permeability for water and ions, and it can be used in both acidic and basic pH ranges. Various pH indicators can be either covalently bound to it [51-57] or physically entrapped in it (where the hydrophobic interactions may also be involved) [58-60]. In the covalent binding method, the cellulose is first hydrolyzed and then activated, followed by soaking in an indicator solution. In the entrapment method, some reagents can be added to improve the performance of the sensing membranes; (1) a coagulating agent such as chloroform to reduce the response time by reducing the thickness and increasing the porosity [58], (2) a plasticizer such as diethyl phthalate to improve the transparency [59], (3) a wetting agent such as ethylene glycol to enhance the hydrophilicity [60], and (4) an ion-balance reagent such as sodium tetra phenyl borate, to increase the sensor response by promoting electroneutrality in the membrane during the changes of pH [59,60].

2.2.4 Photochemical immobilization

Walt's group has developed a photopolymerization method for immobilization of pH indicators to an optical fiber and used it to fabricate imaging fiber-optic pH sensors

[61-67]. In this method, a pH indicator can be immobilized to an optical fiber at its silanized end by illuminating the fiber dipped in a polymerization solution containing a pH indicator [61].

2.2.5. Electrochemical immobilization

Recently, Millar et al. have employed electrochemical polymerization to immobilize fluorescein- substituted thiophene on Pt-coated glass [68]. Electro-polymerization is a simple and attractive method for immobilization since the process can be controlled by electrode potential and allows accurate control of the amount of pH indicator being immobilized by time.

2.2.6 Other organic polymeric substrates

Chlorosulfonated polystyrene fibers [69] and polyacrylamide microspheres [70] have been used for covalent binding of pH indicators. Poly methyl methacrylate (PMMA) [71,72], agarose gel [73], polyurethane hydrogel [74,75] and plasticized PVC [76] have been used for entrapment of pH indicators (in which the hydrophobic interactions may also be involved).

2.2.7 Controlled-pore glass (CPG)

Bacci and Baldini et al. have developed a silylation technique for immobilizing pH indicators on CPG [77,79]. However, the immobilization procedure is quite complicated and time-consuming, which involved silylation, amidization and diazotization of the CPG prior to covalent binding of pH indicator [77].

2.3 Sol-gel glass

The sol-gel process is a liquid-phase method of preparing glasses and ceramics at ambient temperatures, by the hydrolysis and polymerisation of organic precursors followed by room temperature curing. Although, most of the reported sol-gel based sensors are concerned with pH measurement [80-89], they also find application in hydrazine sensing [90], hydrogen peroxide sensing [91], oxygen sensing [92-96], ammonia sensing [97,98] etc. This is probably due to the importance of pH measurement and the availability of a wide variety of suitable dyes. Sol-gel materials used for sensor applications are usually in the form of bulk glass or thin films,

although the latter is most often used because of the shorter response time. Apart from simplicity, the films produced by sol-gel process are tough, inert, intrinsically bound to the fiber core and more resistant than polymer films in aggressive environments. Compared with organic polymers, solgel glass as an inorganic solid substrate offers numerous advantages: (1) higher chemical, photochemical and thermal stability, as well as mechanical strength, (2) optical transparency (down to 250 nm), (3) compatibility with various pH indicators, and (4) feasibility of direct coating on glass and silica fibers. Similar to the polymeric support, the indicator phase is confined within a tubular membrane, which is permeable to the analyte (the hydrogen ions in this case). Since, unlike in polymers the indicator and the analyte are in the same phase, the response time of the sensor is small.

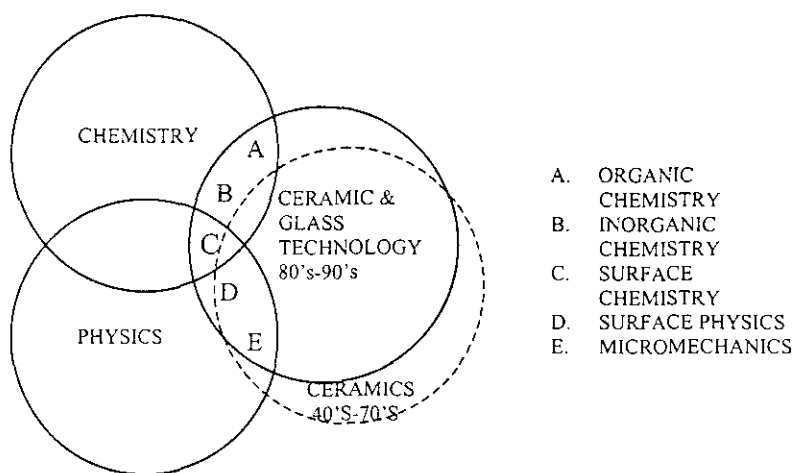


Figure 2.2: Change in the roles of physics and chemistry as ceramics move toward ultrastructure processing.

Sol-gel process is a colloidal route used to synthesize ceramics with an intermediate stage including a sol/gel transition. It is used for the room temperature production of ceramics especially glass [99-106]. This type of glass, viz. sol-gel glass can be porous, whose porosity and hence the refractive index can be controlled over a wide range by adjusting the manufacturing conditions such as temperature or pressure. A flow chart of the process is shown in fig 2.3. Infact the solgel process is not a new

method for the preparation of materials. As early as 1864, Thomas Graham had prepared gels of silica. However, the main disadvantage with this technique was the long period needed for the process. Therefore, this technology was abandoned until around 1980 when new methods with less preparation time were discovered. About 18 million different types of materials have been fabricated using this method.

2.3.2 Main steps involved in sol-gel process.

The various processes involved in the ceramic production through this route are hydrolysis, condensation, gelation, aging, drying (syneris) and finally sintering. Each of these processes can be controlled to get ceramics of various types.

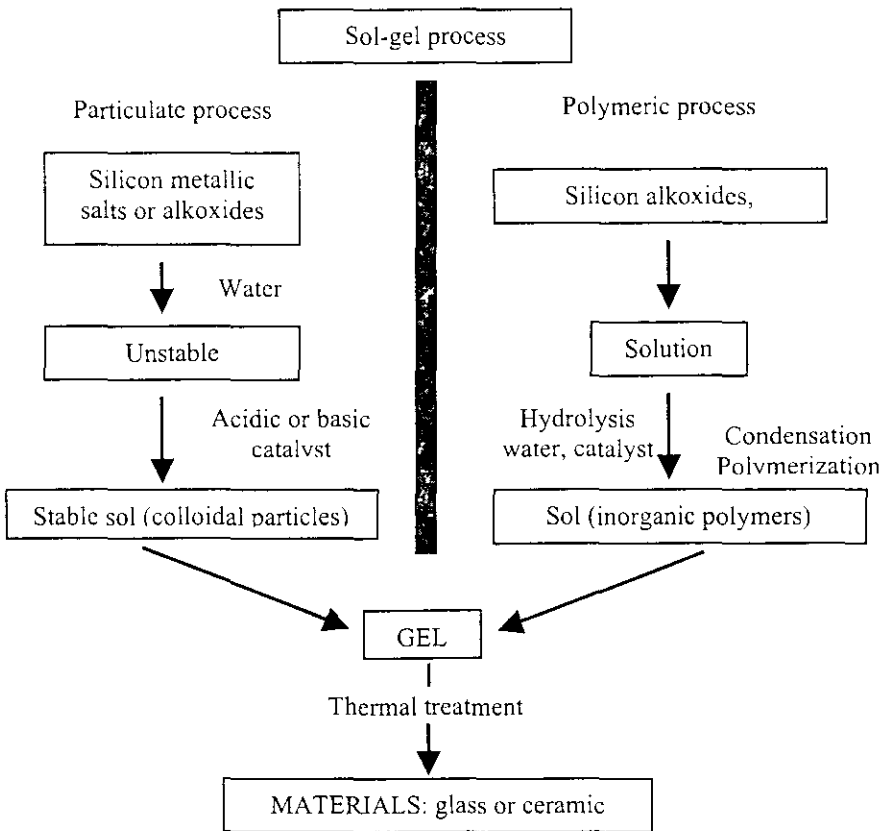
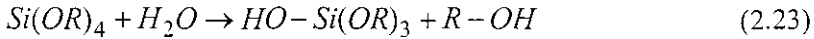


Figure 2.3: Flow chart diagram showing the sol-gel process

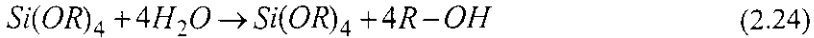
2.3.2.1 Hydrolysis and condensation of metal alkoxide

The degree of hydrolysis of the metal alkoxide of our interest, Tetra Ethyl Ortho Silicate ($\text{Si}(\text{OR})_4$), depends on the amount of water added and is measured in terms of molar ratio

$$r_w = \frac{[\text{H}_2\text{O}]}{[\text{TEOS}]} \quad (2.22)$$

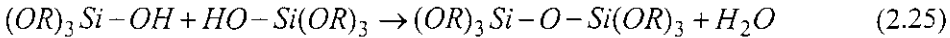


Depending on the amount of water and catalyst present, hydrolysis may go to completion

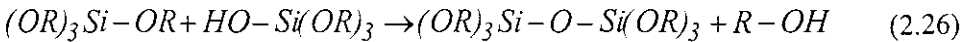


or stop while the metal is only partially hydrolysed, $\text{Si}(\text{OR})_{4-n}(\text{OH})_n$

Two partially hydrolysed molecules can link together in a condensation reaction



or



By definition, condensation liberates smaller molecules than the reactants.

Functionality f is the number of bonds that a monomer can form. A fully hydrolysed silicon alkoxide is tetra functional. A poly functional unit with $f > 2$ can be formed from monomer by cross links to form a 3D picture. With low water concentration, only a little branching occurs. When sufficiently interconnected Si-O-Si bonds are formed in a region, they respond co-operatively as colloidal particles or a sol. The size of the sol particles and the cross linking between them greatly depend on the pH and the molar ratio r_w , which directly influences the physical characteristics of the gel network.

2.3.2.2 Polymerization

Polymerisation of silicates occurs in 4 stages.

- a) Polymerisation of monomers to form particles

- b) Growth of particles
- c) Linking of particles into chains
- d) The extension of the network through the liquid medium to form a gel. When poly functional ($f > 2$) monomer forms bonds at random, it is common to form fractal structures. A mass fractal is distinguished from conventional Euclidean object by the fact that the mass of the fractal increases with its radius according to

$$m \propto r^{d_f} \quad (2.27)$$

where d_f is the fractal dimension which is less than 3. Therefore, its density decreases ($\rho \propto m/r^3$) as the object gets bigger as in the case of a tree. In other words, the area of the fractal increases greater than r^2 . i.e.

$$s \propto r^{d_s} \quad (2.28)$$

where d_s is the surface fractal dimension and $d_s > 2$

2.3.2.3 Gelation

During condensation, if one molecule reaches macroscopic domains so that it extends throughout the solution, the substance is said to be a gel. The gel point is the time at which the last bond is formed that completes this giant molecule. Thus, a gel is a substance that contains a continuous solid skeleton enclosing a continuous liquid phase. The continuity of the solid structure gives elasticity to the gel. The viscosity of sol increases till the gel point and the time required is defined as gelation time t_g which becomes a minimum when $r_w = 7$. Therefore, r_w can be controlled to get different t_g which in turn influences the gel characteristics. The structure of the gel also depends upon whether the sol-gel transition is acid catalyzed or base catalyzed.

2.3.2.4 Aging

Bond formation does not stop at the gel point. There is still a sol within the gel network and those smaller polymers or particles continue themselves to attach to the network. The term aging is applied to the process of change in structural properties of the gel in sol even a long time after gelation. Some gels exhibit spontaneous

shrinkage, called syneresis, as bond formation or attraction between particles induces contraction of the network and expulsion of the liquid from the pores.

2.3.2.5 Drying

The difference in drying procedure gives rise to two types of porous ceramics – xerogel and aerogel.

Xerogel:- drying by evaporation under normal conditions give rise to capillary pressure that causes shrinkage of the gel network. The resulting dried gel called a xerogel is often reduced in volume by a factor of 5 to 10 compared to the wet gel.

Aerogel:- if the wet gel is placed in an autoclave and dried under supercritical condition of high pressure and temperature, there is no interface between liquid and vapor and there is little shrinkage to give an aerogel of density $\sim 0.08 \text{ g/m}^3$ and refractive index 1.008.

The process of drying of a porous material can be divided into several stages. At first it shrinks by an amount equal to the volume of the liquid that evaporates. The second stage begins when the body is too stiff to shrink and the liquid recedes into the interior, leaving air filled pores near the surface. The liquid films in the air filled pores supports further flow of liquid to the exterior and subsequent evaporation. In the final stage of drying, the liquid evaporates within the network and then liquid can escape only by diffusion of its vapor to the surface. If there were no interaction between the solid and liquid components, the liquid would evaporate from the pores leaving the network exposed, but otherwise unchanged. In reality, adsorption and capillary forces oppose exposure of the solid phase, so liquid flows from the interior to replace the liquid which gets evaporated. The tension in the liquid is supported by the solid phase, which therefore goes into compression. As drying proceeds, the network becomes increasingly stiff because new bonds are formed and the porosity is decreased. The tension in the liquid rises correspondingly. Once the radius of the meniscus becomes equal to the radius of the pores in the gel, the liquid exerts the maximum force. After that, the meniscus recedes into the pores, leaving air filled pores near the outside of the gel. The exterior of the gel shrinks faster than the

interior. Therefore, there is high probability for cracking. Aging a gel before drying helps to strengthen the network and thereby reduce the risk of fracture. Surfactants can be added to the pore liquid to reduce stress. DCCA is reported to allow faster drying. DMF also can be added to avoid cracking.

2.3.2.6 Sintering

Densification is the last treatment in sol-gel process, which occurs between 1000^oC and 1700^oC depending upon the radii of the pores and the surface area. Controlling the gel-glass transition is a difficult problem, if one wants to retain shape of the starting material. It is essential to eliminate volatile species prior to pore closure and eliminate density gradients due to non-uniform thermal or atmosphere gradients.

The amount of water in the gel has a major role in the sintering behavior. The viscosity is strongly affected by the concentration of water, which in turn determines the temperature of the beginning of densification. For example, a gel prepared in acidic conditions which has a linear structure has higher surface area and larger water content than gel prepared in basic conditions having a cross-linked structure and starts to densify at about 200^oC sooner than the latter. The higher the temperature to which a gel is exposed, the more nearly it approaches the behavior of an ordinary ceramic.

2.3.4 Thin film coating techniques

Two of widely accepted routes used for thin film production are dip coating and spin coating.

(a) Dip coating

Dip coating is a simple and old way of depositing onto a substrate such as small slabs and cylinders, a uniform thin film of liquid for solidification into a coating. Immersion, start-up, deposition, drainage and evaporation are the processes involved in ordinary dip coating as shown in fig 2.4. The continuous dip coating is simpler as it eliminates start-up and hides drainage in the deposited film. The thin film thickness, h is related to the various parameters as

$$h = C_1 \left(\frac{\eta^4}{\rho g} \right) \quad (2.29)$$

where C_1 is a constant, χ is the viscosity of the sol, u is the drawing speed, ρ is the density of the sol and g is the acceleration due to gravity.

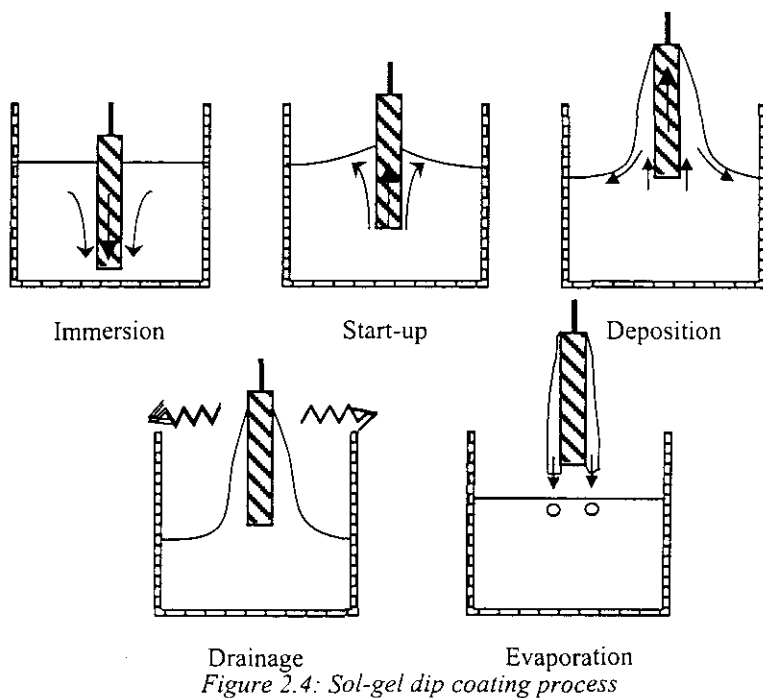


Figure 2.4: Sol-gel dip coating process

(b) Spin coating

Deposition, spin-up, spin-off and evaporation are the various steps involved in spin coating and is shown in fig 2.5.

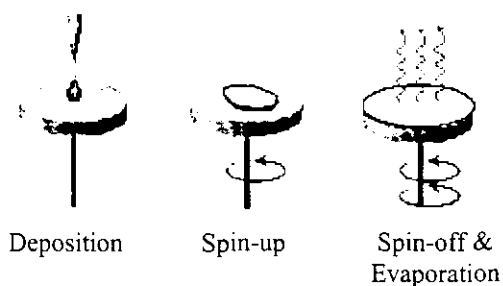


Figure 2.5: Spin coating process

2.3.5 Various forms of sol-gel derived ceramics

Thin films, monoliths, powders, fibers and composites are some of the forms of sol-gel synthesis which are pictorially shown in fig 2.6.

2.3.5.1 Thin films

Sol-gel films alter the reflection, transmission or absorption of light by the substrate. The refractive index of thin films can vary from 1-1.4 by using silicates alone and from 1.4-2.2 by using silica-titania binary system. Antireflection (AR) coatings form another important class of sol-gel application. The refractive index of the sol-gel derived film can be tailored to obtain AR coatings. Active electronic thin films include high temperature superconductors, conductive indium tin oxide (ITO) and V_2O_5 . They impart corrosion resistance or abrasion resistance, promote adhesion, increase strength etc. Pore volumes of the thin film can be controlled to get various refractive indices. Control of the pore size by adding various additives like hydrofluoric acid prior to gelation or by controlled drying, is used in sensor application or as catalytic surfaces due to their large surface area.

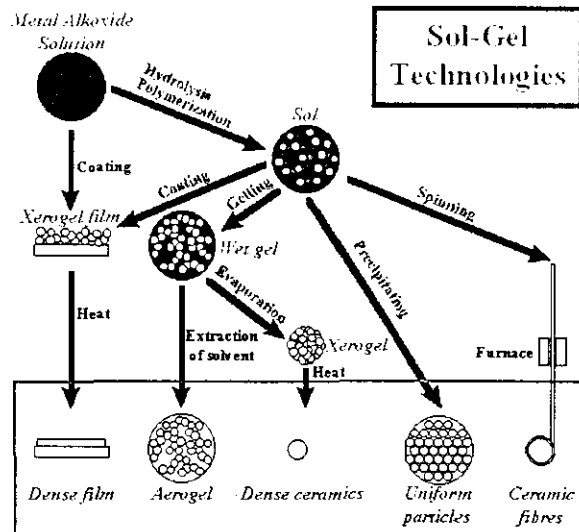


Figure 2.6: Various forms of sol-gel derived ceramics

2.3.5.2 Monoliths

Monoliths are defined as bulk gels (smallest dimension greater than 1 mm) cast to shape. They are applied in fiber optic preforms, lenses and other near net-shape optical components or in graded index glasses (GRINs). Three approaches are used to make sol-gel monoliths; viz. gelation of solution of colloidal powders, hydrolysis and poly condensation of alkoxide or nitrate precursors followed by hypercritical drying of gels, aging and drying under ambient atmospheres.

2.3.5.3 Powders, grains and spheres

Powders are the starting point for most poly crystalline ceramic processing schemes. They are also used as catalysts, pigments, and abrasives. The potential advantage over conventional powders include controlled size and shape, molecular scale homogeneity and enhanced reactivity. Uranyl spheres are used as nuclear fuels and porous beads are used in chromatography.

2.3.5.4 Fibers

In addition to high temperature fiber formation from sol-gel derived preforms, two other methods used for fiber fabrication are drawing of fibers from viscous sols at room temperature and unidirectional freezing of sols.

2.3.5.5 Composites

Sol-gel composites combine different types of materials to obtain synergistic properties unattainable by one material alone. Mixed organic-inorganic or metal-ceramic composites are possible. ORMOSILS and CERAMERS are names coined for describing mixed organic-inorganic composites prepared by sol-gel methods.

2.4 Experiment

2.4.1 Probe fabrication

Tetra Ethyl Ortho Silicate (TEOS) is used as the precursor for sol preparation since the refractive index of the porous silica film produced is less than that of the fiber core. Two sulfonaphthalene dyes, Bromocresol purple (BCP) and bromocresol green (BCG) are first used independently in two pH regions of operation for the pH probe fabrication and then a

Indicator	Color of Acid/Base form	pK_a value of pH range
Methyl violet	Yellow/blue	0.0-1.6
Malachite green	Yellow/blue-green	0.2-1.8
Cresol red	Red/yellow	1.0-2.0
M-cresol red	Yellow/blue	2.8-4.8
Bromophenol blue	Blue/red	3.0-5.0
Congo red	Yellow/blue	4.6
Bromocresol green	Red/yellow	4.0-5.6
4-phenylazo-1-naphthylamine	Yellow/purple	4.0-5.6
Bromocresol purple	Yellow/purple	6.3
Meta-cresol purple	Yellow/purple	7.4-9.0
Naphthollbenzein	Orange/blue	8.2-10.0
Alizarin yellow	Yellow/red	10.0-12.0
Alizarin	Red/purple	11.0-12.4
Indigo carmine	Blue/yellow	11.4-13.0
Tetraethyl aniline sulfonaphthalein	Blue/yellow	13.2

Table 2.1: List of commonly used pH indicator dyes

mixture of three dyes, viz. BCP, BCG and cresol red (CR) are used to develop a sensor to have large dynamic range of operation. Table 2.1 summarizes some of the commonly used pH absorption indicators which if immobilized on a solid support, may undergo significant shifts in their pK_a values (and hence pH transition ranges) and-less-so-their absorption maxima.

The phenolic form predominates in basic conditions, whereas the hydroquinonic form is dominant in low acid concentrations; those forms are

responsible for the colour change in the pH range ($pK_a = 6.3$). Similarly BCG and CR which are shown in fig 2.8 also exist in two forms.

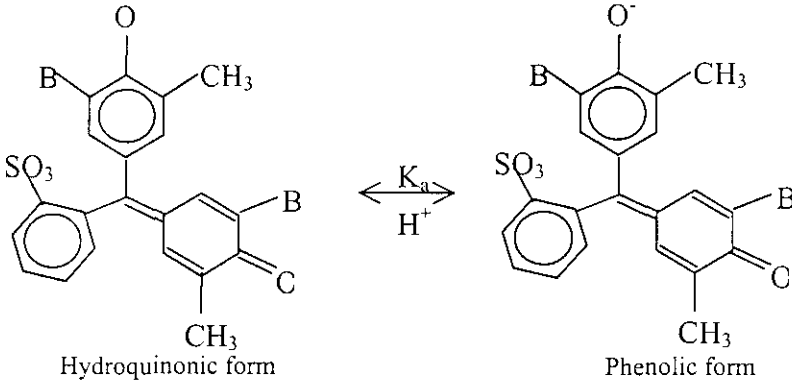


Figure 2.7: Equilibrium of two protonated forms of Bromo Cresol Purple

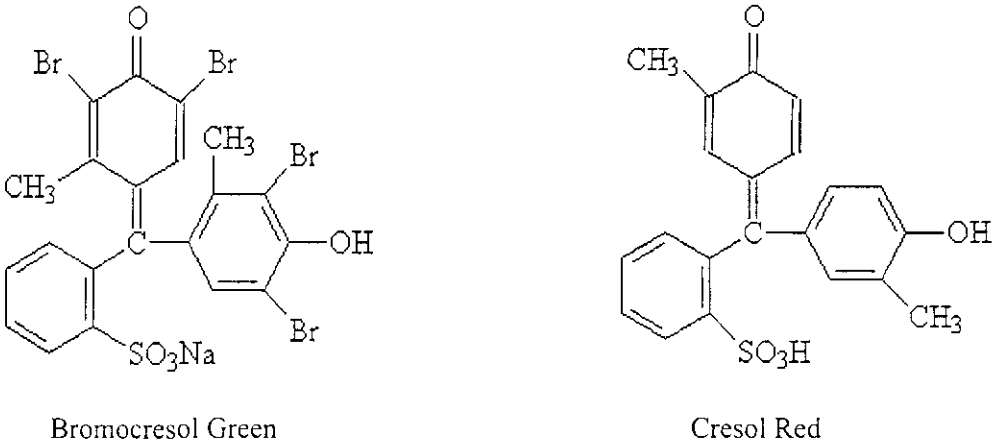


Fig 2.8: Diagrams showing the chemical structure of bromocresol green and cresol red

For fabricating the sensor probe a plastic clad silica (PCS) fiber with core diameter $200\mu\text{m}$ and numerical aperture (NA), 0.22 is used. The total length of the fiber taken is 35cm of which about 5cm in the middle portion is unclad. TEOS, anhydrous ethanol, water, HCl and the indicator dye are mixed in the molar ratio $1:4:1:0.02:10^{-4}$ at room temperature with the help of a magnetic stirrer. Ethanol acts as a common solvent for TEOS and water while HCl is used as a catalyst. The porous

silica is coated on the unclad portion of the fiber using the dip coating technique with a PC controlled stepper motor. In this technique, the dipped fiber is pulled upwards at an optimized rate of 100-mm/ minute. Interferometric technique is employed to find out the thickness of the thin film and it has been found to be ~ 200 nm for a single layer. The second layer is coated over the first one only after the complete curing of the latter and the third layer is coated in the same fashion. As a result, there exists an interface between different layers. These fibers are then kept for 15 days for the dye to be stabilized in the gel matrix and this reduces leaching of the dye molecules. Additionally, the porosity increases to an optimum value of 33% and refractive index reduces to a value of 1.21 for maximum sensitivity [77]. It is then washed in water to remove the excess and unbound dye. The coated region is again dried at 50° C.

2.4.2 The experimental set-up

A 50 W tungsten halogen lamp with a monochromator (McPherson UV 275) and PMT (Oriel) are used to record the evanescent wave (EW) absorption spectrum of the fiber optic sensor as shown in fig 2.9. The pH of the solution is monitored by a pH electrode (pH scan 2, MERCK), which has a sensitivity of 0.1 units. The pH value of the solution is varied by adding either HCl or NaOH.

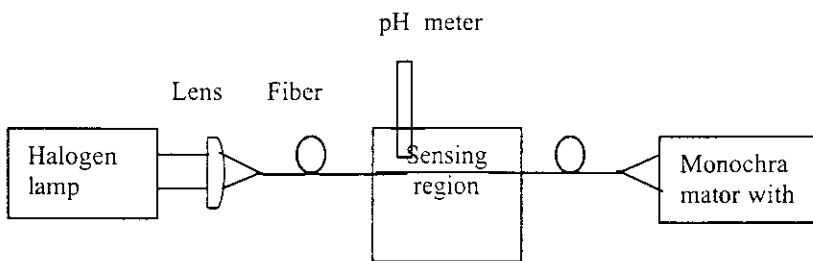


Figure 2.9: Experimental setup to record evanescent wave absorption spectrum

Fig 2.10 shows the normalized EW absorption spectrum of the fiber optic pH sensor using immobilized BCP dye for solutions having different pH surrounding the sensing region. The normalization is achieved by using the absorption spectrum of a

fiber coated with an undoped sol-gel thin film. The EW absorption spectrum of the sensor is found to match well with that of a thin film of the dye coated on a glass substrate, recorded using a spectrophotometer (Jasco V-570). As the pH of the solution surrounding the fiber increases, the absorbance of the alkaline form of the indicator increases and that of the acidic form decreases, but with smaller relative change than the former. Similar type of plot is obtained for BCG dye as well and is shown in fig 2.11.

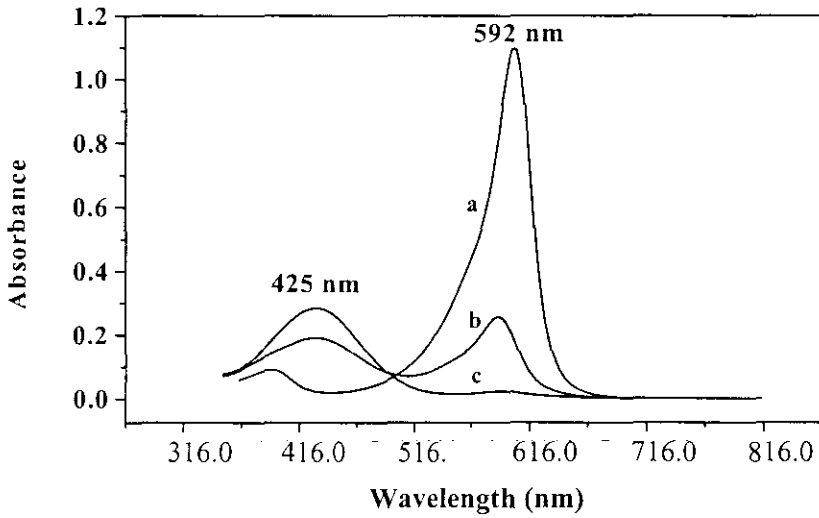


Figure 2.10 : EW absorption spectrum of pH sensor with BCP in different pH environments ($a = 11$, $b = 8$, $c = 5$)

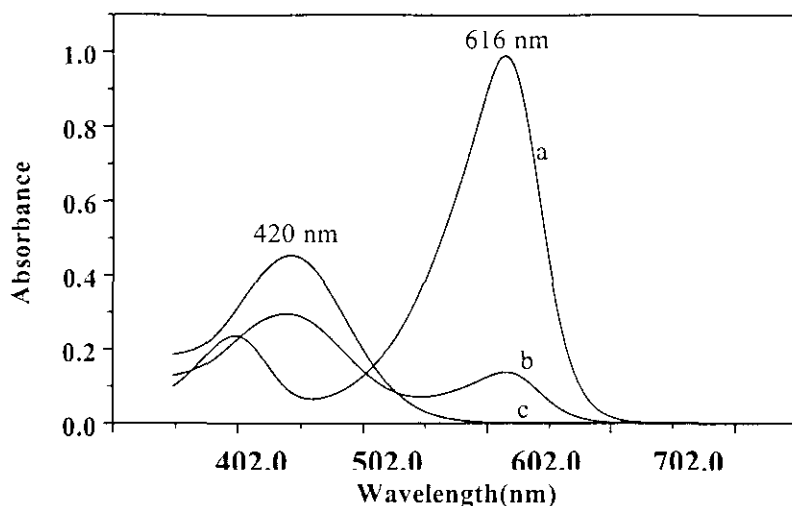


Figure 2.11: EW absorption spectrum of pH sensor with BCG in different pH environments ($a = 11$, $b = 8$, $c = 5$)

As the relative change in absorbance with respect to the pH of the solution is greater for the alkaline form of both the dyes, the wavelength of the light used to characterize the fiber optic pH sensor is selected to be near the absorption peak of the alkaline form of the indicator dye. This is the motivation for using He-Ne laser (633 nm) as the source for the present work. Some of the properties of the sol-gel immobilized indicator dye differ from those in solution. For example, the pK_a value of BCP in solution is 6 and that in sol-gel matrix is 9 whereas for BCG it is 4.4 and 8 respectively. The pH range of BCP in solution is 5.2 - 6.8 and in sol-gel, it is 7.5 - 10.5. BCG has a pH range of 3.6 - 5.2 in solution and 6.5 - 9.5 in sol-gel matrix.

Fig 2.12 shows the absorption spectra of a mixture of dyes (bromocresol green, bromocresol purple and cresol red) doped in multi-layer sol-gel thin film that is coated over a glass substrate under different pH environments. It can be clearly seen that as the pH of the solution surrounding the film containing the mixture of dyes increases, the absorbance of the alkaline form of the dye increases and vice versa. The peak absorption of the alkaline form of the dye mixture is at a wavelength 589 nm. Even though the operating wavelength in the present case does not correspond to the

peak absorption, it can be seen that there is considerable amount of absorption even at 633 nm.

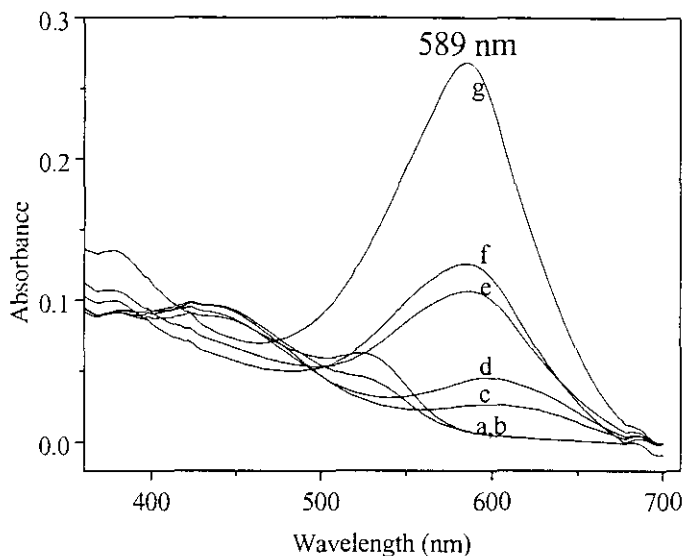


Figure 2.12: Variation of absorption spectrum of dye mixture in sol-gel thin film with respect to various pH environments (a = pH 3, b = pH 5, c = pH 7, d = pH 9, e = pH 11, f = pH 13)

The experimental set-up used to calibrate the pH sensor is shown in fig 2.13.

The laser emission at 633 nm of a He-Ne laser is coupled to the optical fiber (OF) using a microscopic objective (MO) having almost the same NA as that of the fiber. Light intensity at the output of the fiber is measured using a power meter (Metrologic 45 - 545) and simultaneously the pH of the solution is monitored by a pH electrode (pH scan 2, MERCK), which has a sensitivity of 0.1 units. The pH value of the solution is varied by adding either HCl or NaOH.

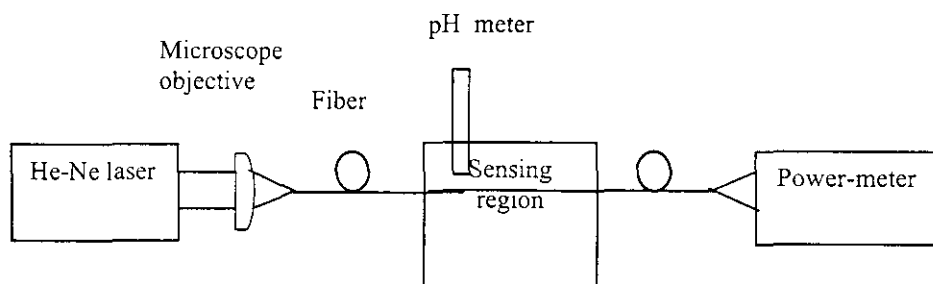


Figure 2.13: Experimental setup for characterizing pH sensor

2.5 Results and Discussion

Single layer coatings of BCP doped sol-gel thin film in the unclad portion of the optical fiber gives only a poor sensitivity for the fiber optic sensor (FOS) as can be inferred from fig 2.14. Similar kind of device performance has been observed for BCG also. This is evidently due to insufficient film thickness of about 200 nm acting as the lossy cladding. The penetration depth of the EW is of the order of the wavelength of light used, i.e. about 600 nm, which is much greater than a single layer thickness. Therefore, the evanescent wave entering the sensing region penetrates it and escapes into the surrounding medium (solution). In other words, with insufficient thin film thickness the sensing region as well as the solution acts as the cladding. However, only the portion of the evanescent wave in the sensing region will be absorbed to modify the output intensity. Hence, the modified Beer-Lambert law cannot be applied here in the strictest sense.

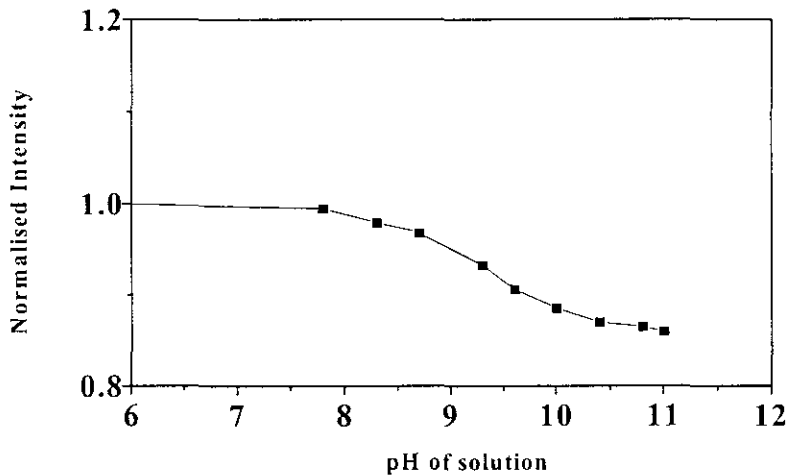


Figure 2.14: Sensor response with a single layer of BCP doped sol-gel thin film

Even though increasing the withdrawal rate can enhance the thickness of the thin film (2.30), it is found that thicker films are found to crack during the sintering process due to high mechanical stress induced by the large shrinkage of the densifying film. These cracks cause a decrease in the effective coupling of the evanescent field, which reduces the sensitivity of the device in addition to increased

scattering losses. Therefore, we have adopted a new method to increase the thickness of the cladding (thin film) by using multiple sol-gel coatings. The existence of interfaces between different layers suppress cracking of the film. Thick films produced by multiple sol-gel coatings are observed to be less prone to cracking. This procedure has been found to enhance the sensitivity of the device fabricated with BCP (an increase of $\sim 70\%$ fractional change in intensity). The plots in fig 2.17 illustrate the above-mentioned improvement in the device performance. It is observed that a similar kind of behavior is obtained with the pH sensor fabricated using BCG dye also as shown in fig 2.16. Two as well as three layers of dye doped sol-gel thin films have been coated on the unclad portion of the fiber to provide a systematic study of the effect of multiple sol-gel coatings.

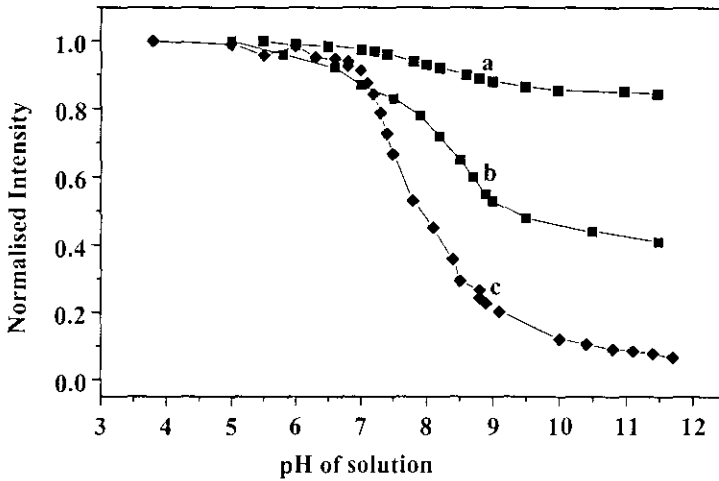


Figure 2.15: Response of the sensor fabricated with different layers of thin film containing BCP ($a = 1$ layer, $b = 2$, $c = 3$ layer)

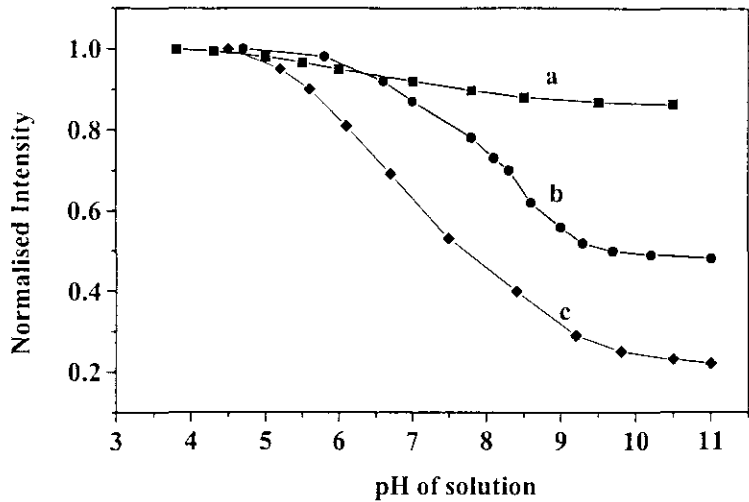


Figure 2.16: Response of the sensor fabricated with different layers of thin film containing BCG ($a = 1$ layer, $b = 2$, $c = 3$ layer)

Figure 2.17 shows the variation of the output intensity of the wide range fiber optic pH sensor with a mixture of dyes having a sensing length of 5 cm, with a change in pH value of the solution surrounding the sensing region. It is evident that the sensitivity increases with the number of thin film layers that constitute the sensing membrane.

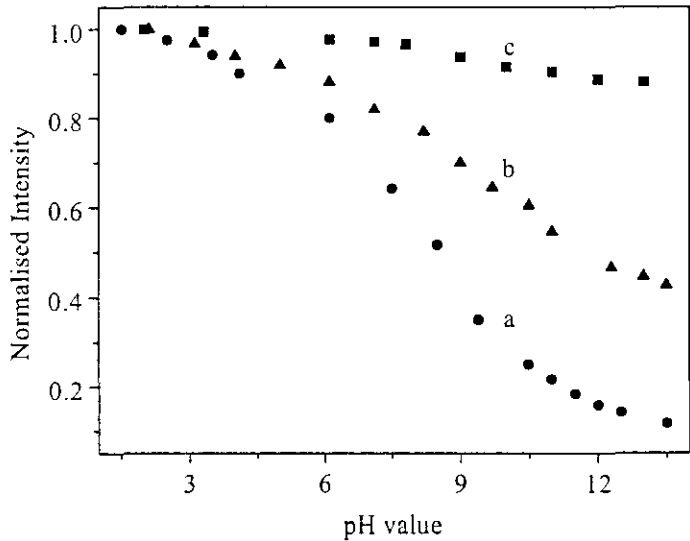


Figure 2.17: Response of the sensor with sensing length of 5 cm fabricated with different layers of thin film containing a mixture of dyes ($a = 1$ layer, $b = 2$, $c = 3$ layer)

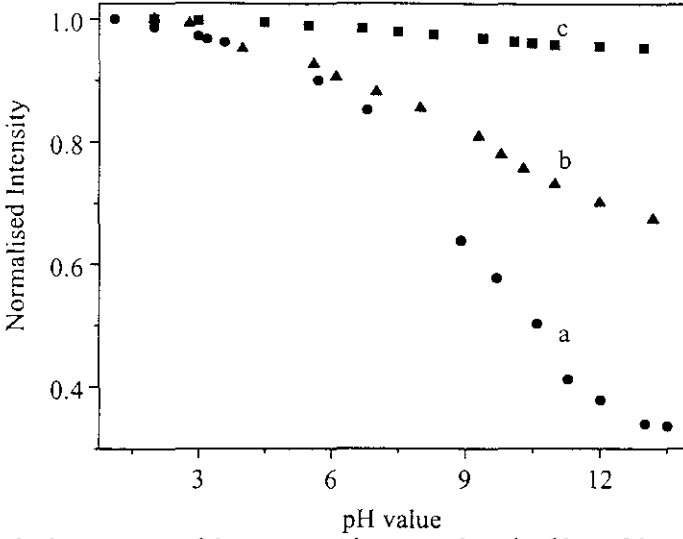


Figure 2.18: Response of the sensor with sensing length of 3 cm fabricated with different layers of thin film containing a mixture of dyes (a = 1 layer, b = 2, c = 3 layer)

Figure 2.18 shows the performance of the wide range sensor under different pH environments with a reduced sensing length l of 3 cm. It is to be noted that eventhough the sensitivity with a single layer is low, it can be increased by multiple sol-gel coatings and the sensitivity is almost same as that obtained with 5 cm sensing length. By comparing the two figures, it can be seen that sensitivity of 3-layered sensor with 3 cm sensing length is comparable to that of 3-layered sensor with 5 cm sensing length. Thus it is quite evident that eventhough the sensitivity with a single layer is low, it can be enhanced by employing multiple sol-gel coatings without increasing the sensing length.

Such a behavior is attributed to the insufficiency in the thickness of the single layer or two layer sensing membrane (sol-gel film) to confine the evanescent field. If the thickness of the sensing region is less than the penetration depth d_p of the evanescent field then equation (2.20) can be modified as,

$$P(l) = P_0 \exp[-(\gamma_1 + \gamma_2)z] \quad (2.30)$$

where γ_1 and γ_2 are the evanescent wave absorption coefficients of the sensing membrane and that of the surrounding solution. $\gamma_1 = \eta_d \alpha_d$ and $\gamma_2 = \eta_s \alpha_s$; η_d , being the fraction of the guided power within the sensing membrane and α_d is the corresponding absorption coefficient; η_s is the fraction of the guided power outside the sensing membrane and α_s is the corresponding absorption coefficient. Since the absorption coefficient of solution will be negligibly small compared to that of the sensing element (31) is reduced to

$$P(l) = P_0 \exp(-\eta_d \alpha_d z) \quad (2.31)$$

Again, the fraction of the guided power through the sensing element is proportional to the thickness t of the sensing membrane.

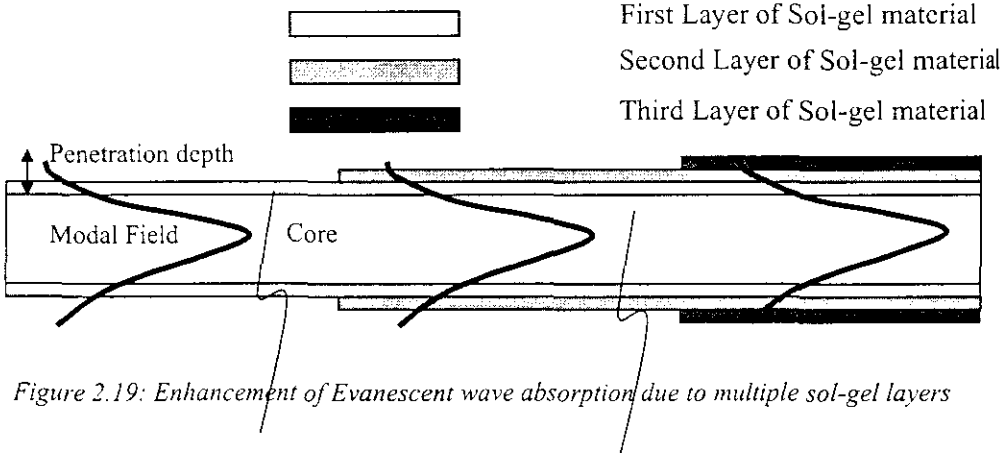


Figure 2.19: Enhancement of Evanescent wave absorption due to multiple sol-gel layers

Nevertheless α_d is a constant for a particular dye. Therefore, the only parameter that can be varied to get a better sensitivity is η_d . This can be achieved by increasing the thickness of the sensing region. When the sensing region thickness is less than the penetration depth d_p as in the case with one layer or two layer thin film coating, η_d is less than the actual fractional power η . Therefore, the effective fractional power in the sensing region, which is available for intensity modulation at the fiber output, increases with increase in the number of thin film layers. The optimum thickness of the thin film is nearly equal to the penetration depth of the evanescent wave. When the film thickness becomes greater than the penetration depth, the temporal response

of the sensor may be adversely affected, as the analyte has to traverse a longer distance through the gel matrix. The EW absorption spectra of BCG show that absorbance of the sol-gel thin film increases with increase in the number of layers as shown in fig 2.21 which is similar to the results obtained for BCP (fig 2.20)

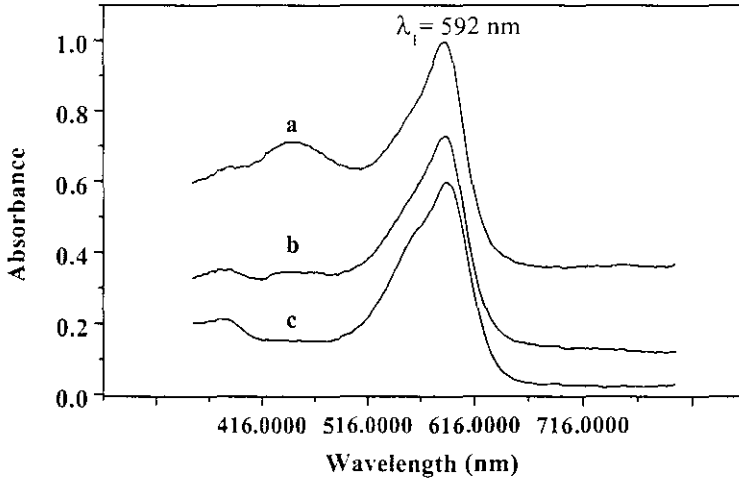


Figure 2.20: EW absorption spectrum of pH sensor with BCP in pH 10 with different thin film layers (a = 3 layer, b = 2 layer, c = 1 layer)

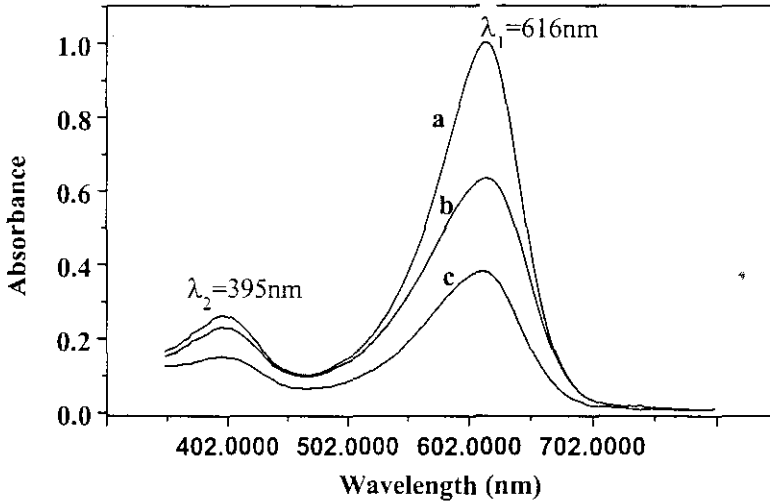


Figure 2.21: EW absorption spectrum of pH sensor with BCG in pH 10 with different thin film layers (a = 3 layer, b = 2 layer, c = 1 layer)

The improved sensitivity also indicates that there is a high level of interconnectivity between pores in different layers of the sol-gel thin film. The analyte (H^+ and OH^- ions) diffuses through the pores of the outer layer of the pH sensor and interacts with the indicator molecules present there. It then enters the inner layer and traverse through it and enters further into the next inner layer. Hence the dye in the innermost layer also is brought into interaction with the analyte. It can be assumed that the analyte molecules entering the outermost layer do not encounter the barrier between different layers of thin film and hence can react with the sensing species even near the core effectively. Since the fraction of EW power is maximum in the inner most layer, the interconnectivity between pores has a significant role in the increased sensitivity of the present multi-layer fiber optic pH sensor.

The sensitivity of the device is found to be unaffected even after keeping it in low pH (acidic regime) environments for several days. Nevertheless, when the sensor is kept in alkaline solution for a long time the sensitivity is found to be reduced. This reduction in intensity is due to the leaching of the dye molecules from the gel matrix. The important factors that determine the leaching of a dopant from sol-gel derived film include the size of the dopant, the pore diameter of the sol-gel material and the solubility of dopant in the solution. Since the first two factors are constants for a once fabricated thin film, the only factor that may depend on the pH of the surrounding solution is the solubility of the dye in different pH environments. Similar results were observed by Butler et al [78] for another pH indicator dye, bromophenol blue, in sol-gel matrix. From this it can be inferred that the leaching of the dye is significant at higher pH. The solubility dependence of BCP and BCG on pH value of the solution is the key factor. At very high pH increased leaching would be expected from sol-gel silica films due to alkaline attack, which results in dissolution of silica. This also contributes to the observed effect of decrease in sensitivity at very high pH environments. The sensor is found to give similar results even after storage for a period of three months.

This chapter describes the fabrication of a highly sensitive evanescent wave fiber optic pH sensor using sol-gel technology. Different sensors are detailed using various dyes and mixture of dyes. Moreover, the temporal response of the sensor also has been studied. The obtained results are explained based on absorption spectrum of the dye impregnated sol-gel films.

REFERENCES

1. Andrej Holobar, Bernhard H Weigl, Wolfgang Trettnak, Roman Benes, Hartmut Lehmann, Nena V Rodriguez, Arnold Wollschlager, Paul O Leary, Peter Raspor, Otto S Wolfbeis, *Sens. Act. B*, 425 (1993)
2. David M Jordan and David R Walt, Fred P Milanovich, *59*, 437 (1987)
3. Christopher G Cooney, Bruce C Towc, *Sens. Act. B*, 62, 177 (2000)
4. J I Peterson, S R Goldstien, RV Fitzgerald, D K Buckhold, *Anal. Chem.* 52, 864 (1980)
5. Philip H Paul and George Kychakoff, *Appl. Phys. Lett.* 51, 12 (1987)
6. D Gloge, *Appl. Opt.* 10, 2252 (1971)
7. V Ruddy, B D MacCraith and J A Murphy, *J. Appl. Phys.* 67, 6070 (1990)
8. C S Villarruel, D D Dominguez and A Dandridge, *Proc. SPIE*, 798, 225 (1987)
9. Lisa C Shriver-Lake, Robert A Ogert and Frances S Ligler, *Sens. Act. B*, 11, 239 (1993)
10. B D Gupta, C D Singh and Anurag Sharma, *Opt. Engg.* 6, 1864 (1994)
11. A Messica, A Greenstein, A Katzir, U Schiessl and M Tacke, *Opt. Lett.* 19, 1164 (1994)
12. A Messica, A Greenstein and A Katzir, *35*, 2274 (1996)
13. R Simhi, Y Gotshal, D Bunimovich, B Sela and A Katzir, *Appl. Opt.* 35, 3421, (1996)
14. N Nath and S Anand, *Opt. Engg.* 37, 220 (1998)
15. S K Khijwania and B D Gupta, *Opt. Comm.* 152 259 (1998)
16. V Ruddy, *Fiber Integrated Opt.* 9, 143 (1990)
17. B D Gupta, S K Khijwania, *Fiber Integrated Opt.* 17, 63 (1998)
18. B Culshaw, F Muhammad, G Stewart, S Murray, P Pinchbeck, J Norris, S Cassidy, M Wilkinson, D Williams, I Crisp, R V Ewyk and A McGhee, *Elec. Lett.* 28, 2232 (1992)
19. A P Russel and K S Fletcher, *Anal. Chimica Acta*, 170, 209 (1995)
20. Matsuo H, Kuniyoshi S, Kudo K and Tanaka K, *Synthetic Metals*, 115, 37 (200)
21. Bariatian C, Matias I R, Romeo I, Garrido J and Laguna M, *App. Phys. Lett.* 77, 2274 (2000)
22. S K Khijwania and B D Gupta, *Opt. Quan. Elec.* 31, 625 (1999)
23. Otsuki S, Adachi K and Taguchi T, *Sens. Act. B*, 53, 91 (1998)
24. Campbell M, Yang Y T, Wallace P A, Holmes Smith A S, *Opt. Rev.* 4, 111 (1997)
25. Woerdeman D L, Flynn K M, Dunkers J P and Parnas R S, *J. Reinforced Plastics and Composites*, 15, 922 (1996)
26. Egalon C O, Mendoza E A, Khalil A N and Lieberman R A, *Opt. Engg.* 34, 3583 (1995)
27. Rontrrioli C, Kherrat T and Jaffrezi C and Renault N, *Sensors and Materials*, 7, 383 (1995)
28. Feldman S F, Uzgiris E E, Penney C M, Gui J Y, Shu E Y and Stokes E B, *Biosensors and Bioelectronics*, 10, 423 (1995)
29. B D MacCraith, O' Keeffe G, A K McEvoy, C M McDonagh, F McGilp, B O'Kelly, J D Omahony and M Cavanagh, *Opt. Engg.* 33, 3861 (1994)
30. Hale Z M, Payne F P, *Anal. Chimica Acta*, 293, 49 (1994)
31. J Rayss and G Sudolski, *Opto-electronics review*, 8, 129 (2000)
32. H P Kao, N Yang and JS Schoeniger, *J. Opt. Soc. Am. A*, 15, 2163 (1998)
33. D Jose, M Shelly John, P Radhakrishnan, V P N Nampoore and C P G Vallabhan, *Thin Solid Films*, 325, 264 (1998)
34. M Shelly John, P Radhakrishnan, V P N Nampoore and C P G Vallabhan, *Meas. Sci. Technol.* 10, N13-N20 (1999)
35. P Sureshkumar, C P G Vallabhan, V P N Nampoore, V N Sivasankara Pillai and P Radhakrishnan, *J. Opt A*, 4, 247 (2002)

36. P Sureshkumar, Thomas Lec S, V P N Nampoore, C P G Vallabhan & P Radhakrishnan, *Opt. Comm.*, 214, 25 (2002)
37. P Radhakrishnan, V P N Nampoore and C P G Vallabhan, *Opt. Eng.* 32, 692 (1993)
38. M Jakusch, B Mizaikoff, R Kellner and A Katzir, *Sens. Act. B*, 38-39, 83 (1997)
39. M J P Leiner and P Hartmann, *Sens. Act. B*, 11, 281 (1993)
40. A. Dybko, R.S. Romaniuk, J. Maciejewski, Z. Brzozka, *Int. J. Optoelectron.* 7, 443 (1992)
41. G. Vishnoi, T.C. Goel, P.K.C. Phillai, *Proceedings SPIE* 3538, 319 (1998)
42. A. Dybko, J.Maciejewski, R.S. Romaniuk, W. Wroblewski, *Proceedings SPIE* 2085, 131 (1993)
43. S. Zhang, S. Tanaka, Y.A.B.D. Wickramasinghe, P. Rofe, *Med. Biol. Eng. Comput.* 33,152 (1995)
44. S. Igarashi, K. Kuwae, T. Yotsuyanagi, *Anal. Sci.* 10, 821 (1994)
45. Y. Shi, C.J. Seliskar, *Chem. Mater.* 9, 821 (1997)
46. N. Takai, T. Hirai, I. Sakuma, Y. Fukui, A. Kaneko, T. Fujie, *Sens. Actuators B* 13-14, 427 (1993)
47. G. Serra, A. Schirone, R. Boniforti, *Anal. Chim. Acta* 232, 337 (1990)
48. S. Motellier, M.H. Michels, B. Dureault, P. Toulhoat, *Sens. Actuators B* 11, 467 (1993)
49. S. Motellier, M.H. Noire, H. Pitsch, B. Dureault, *Sens. Actuators B* 29, 345 (1995)
50. B. Kuswandi, R. Narayanasway, *Fresenius J. Anal. Chem.* 364, 605 (1999)
51. O.S. Wolfbeis, N.V. Rodriguez, T. Werner, *Mikrochim. Acta* 108, 133 (1992)
52. Y. Kostov, S. Tzonkov, L. Yotova, M. Krysteva, *Anal. Chim. Acta* 280,15 (1993)
53. T. Werner, O.S. Wolfbeis, *Fresenius J. Anal. Chem.* 346, 564 (1993)
54. G.J. Mohr, O.S. Wolfbeis, *Anal. Chim. Acta* 292, 41 (1994)
55. A. Safavi, M. Pakniat, *Anal. Chim. Acta* 335, 227 (1996)
56. A. Safavi, H. Abdollahi, *Anal. Chim. Acta* 367, 167 (1998)
57. A.A. Ensafi, A. Kazemzadeh, *Microchem. J.* 63, 381 (1999)
58. Y.V. Kostov, *Sens. Actuators B* 8, 99 (1992)
59. T.J. Cardwell, R.W. Cattrall, L.W. Deady, M. Dorkos, G.R. O'Connell, *Talanta* 40, 765 (1993)
60. W. Wroblewski, E. Roznicka, A. Dybko, Z. Brzozka, *Sens. Actuators B* 48, 471 (1998)
61. S.M. Barnard, D.R. Walt, *Nature* 353, 338 (1991)
62. K.S. Bronk, D.R. Walt, *Anal. Chem.* 66, 3519 (1994)
63. P Pantano, D.R. Walt, *Anal. Chem.* 67, 481A (1995)
64. J.A. Ferguson, B.G. Healey, K.S. Bronk, S.M. Barnard, D.R. Walt, *Anal. Chem.* 340, 123 (1997)
65. B.G. Healey, D.R. Walt, *Anal. Chem.* 69, 2213 (1997)
66. K.S. Bronk, K.L. Michael, P. Pantano, D.R. Walt, *Anal. Chem.* 67 2750 (1995)
67. A. Panova, P. Pantano, D.R. Walt, *Anal. Chem.* 69, 635 (1997)
68. D. Millar, M. Uttamlal, R. Henderson, A. Keeper, *Chem. Commun.* 477, (1998)
69. B.S. Rao, J.B. Puschett, K. Matyjaszewski, *J. Appl. Polym. Sci.* 43, 925 (1991)
70. D. Cui, Q. Cao, J. Han, J. Cai, Y. Li, Z. Zhu, *Sens. Actuators B* 12 29(1993)
71. C. Egami, K. Takeda, M. Isai, M. Ogita, *Opt. Commun.* 122, 122 (1996).
72. C. Egami, Y. Suzuki, O. Sugihara, H. Fujimura, N. Okamoto, *Jpn. Appl. Phys.* 36, 2902 (1997)
73. T. Hao, X. Xing, C.C. Liu, *Sens. Actuators B*, 10, 155 (1993)
74. T. Werner, C. Huber, S. Heini, M. Kollmannsberger, J. Daub, O.S. Wolfbeis, *Fresenius J. Anal. Chem.* 359, 150 (1997)

75. S. Draxler, M.E. Lippitsch, Proceedings SPIE 2388, 363 (1995)
76. D.B. Papkovsky, G.V. Ponomarev, O.S. Wolfbeis, J. Photochem. Photobiol. A Chem. 104, 151 (1997)
77. M. Bacci, F. Baldini, S. Bracci, Appl. Spectrosc. 45, 1508 (1991)
78. F. Baldini, S. Bracci, F. Cosi, Sens. Actuators 37-38, 180 (1993)
79. F. Baldini, S. Bracci, F. Cosi, P. Bechi, F. Pucciani, Appl. Spectrosc. 48, 549 (1994)
80. B D MacCraith, V Ruddy, C Potter, B O' Kelly, J F McGlip, Elect. Lett. 22, 1247 (1991)phsol
81. B D Gupta, D K Sharma, Opt. Comm. 140, 32 – 35 (1997)
82. B D Gupta, Sonu Sharma, Opt. Comm. 154, 282 – 284 (1998)
83. J Y Ding, M R Shahriari and C H Siger, Jun. Elec. Lett. 27, 1560 (1991)
84. C Gagnadre, M Billon, S Thuillier, Elec. Lett. 34, 1991 (1998)
85. O Lev, B I Kuyavskaya, Y Sacharov, C Rottman, Kuselman, D Anvir, M Ottolenghi, Proc. SPIE, 1716 (1982)
86. B D MacCraith, V Ruddy, C Potter, B O' Kelly and J F McGilp, Elec. Lett. 27, 1247 (1991)
87. Leonardo R Allain, K Sorasaenee and Z Xue, Anal. Chem. 69, 3076 (1997)
88. C Malins, HG Glever, E Keyes, J G Vos, W J Dressick and B D MacCraith, Sens. Act. B, 67, 89 (2000)
89. C A Browne, D H Tarrant, M S Olteanu, J W Muulens and E L Chronister, Anal. Chem. 68, 2289 (1996) solph
90. C Gojon, B Durealt, N Hovanian and C Guizard, Sens. Act. B, 38-39, 154 (1997) hydrazine
91. A Lobnik and M Cajlakovic, Sens. Act. B, 3682, 1 (2000) sol hy per
92. B D MacCraith, C McDonagh, G O'Keefe, A K McEvoy, 30, 888 (1994)
93. B D MacCraith, G O'Keefe, C McDonagh, A K McEvoy, J F McGilp, B O' Kelly, J D O'Mahony, M Cavanagh, Opt. Engg. 33, 3861 (1994)
94. M K Krihak and M R Shahriari, Elec. Lett. 32, 240 (1996) sol oxy
95. A K McEvoy, C McDonagh, B D MacCraith, Analyst, 121, 785 (1996)
96. R Klein, E Voges, Sens. Act. B 11, 221 (1993) ammonia
97. A Lobnik and O S Wolfbeis, Sens. Act. B, 51, 203 (1998) ammonia
98. C Jefferey Brinker, George W Sherer, Academic Press (1990)
99. A. Lobnik, I. Oehme, I. Murkovic, O.S. Wolfbeis, Anal. Chim. Acta 367, 159 (1998)
100. J Livage, Bull. Mater. Sci. 22, 201 (1999)
101. Larry L Hench, John K West, Chem. Rev. 90, 33 (1990)
102. Ginancarlo C Righni and Stefano Pelli, J. Sol-Gel Scie. Tech. 8, 33 (1997)
103. Alain C Pierre, Kluwer Academic Publishers (1998)
104. Paras N Prasad, Plenum Press, New York, 1998.
105. M R Shahriari, Optical fiber sensor technology Vol 4, Edited by K T V Grattan and B T Meggitt, Kluwer Academic Publishers, London (1998)
106. T M Butler, B D MacCraith, C McDonagh, J. Non-Crys. Solids, 224, 249 (1998)

Chemical Sensing Using Microbent Optical Fibers

Introduction

Microbend loss has always been an undesirable effect causing problems in fiber optic communication links. However, this phenomenon has been exploited profitably in fabricating a variety of fiber optic sensors [1-46] and in other applications such as development of mode strippers and mode scramblers [47], mode filters, phase shifters [48,49], signal processing [50] etc. The sensing applications include the measurement of physical parameters such as pressure, temperature, displacement, acceleration, electric and magnetic fields etc. Moreover, they have been used in distributed sensing applications [4,7]. In addition, microbend sensors have been used in hostile environment applications such as pollution monitoring, high temperature zone monitoring, explosion hazard areas, adverse environments [12] etc. Microbend sensors have interesting properties with some outstanding performance characteristics that have made them successful in several commercial applications. Microbend fiber optic acoustic sensor is one of the earliest forms of FOS; sensors based on microbend loss in optical fibers were first proposed and demonstrated as early as 1980 [40-42].

The early interest in microbend sensors was for acoustic and hydrophone applications and ever since that, much has been done to understand the basic mechanism of microbend sensors and how to increase the dynamic range and improve sensitivity. More than 100 research articles have been published in this regard.

In addition to the general advantages of fiber optic sensors so often mentioned (EMI interference, electrical isolation and freedom from ground loops, small size and weight), microbend sensors have been demonstrated to have their own unique set of advantages, which include:

- mechanical and optical efficiency that leads to low parts count and low cost.
- easy mechanical assembly that does not require fiber bonding to other components and thus avoids differential thermal expansion problems.
- fail-safe fiber sensor which either produces a calibrated output signal or fails to a state of no light output.

What is microbending? In simplest terms, it is the bending of a fiber (single or multimode) with very small bending radius of the order of the diameter of the fiber. In a bent fiber, the more severe the mechanical perturbation or bending, the more light is coupled to radiation modes and is lost. Essentially microbend sensors are based on coupling and leakage of modes propagating in a deformed fiber. Usually this deformation is achieved by employing corrugated plates, which deforms the fiber into a series of sharp bends with small bending radii as shown in fig 3.1. Such periodic bending causes coupling of energy between various guided (core) modes as well as between guided modes and leaky modes (consists of both cladding and radiation modes); the latter causing a loss in transmission as shown in fig 3.2. Thus, the important characteristic of a microbend fiber optic sensor (microbender) are that it generally uses a multimode optical fiber, and the intensity decreases with mechanical bending.

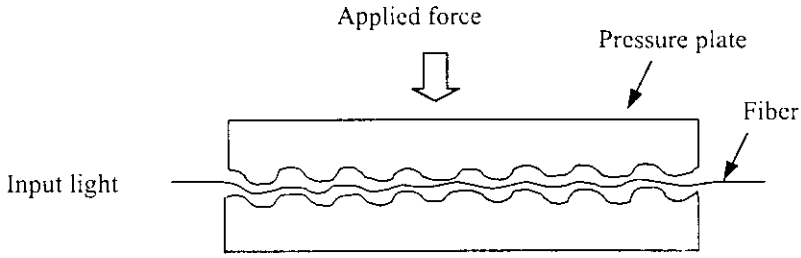


Figure 3.1: Original diagram of microbend fiber optic sensor

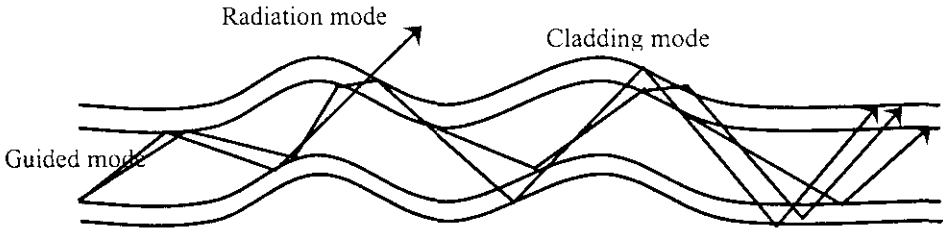


Figure 3.2: ray diagram representation of mode coupling in a periodic bent fiber

In most of the cases the bends made on the fiber are temporary since the deformations made on the fiber will vanish if the pressure applied on the corrugated plates is removed, provided the pressure applied is within the elastic range of the fiber. However, a few investigations have been carried out with permanent microbend fibers also [13,14]. Nevertheless, these are essentially an extension of what is done with temporary microbend fibers and are mainly used for measuring physical parameters. Moreover, almost all of the microbend sensors are used for the detection and measurement of physical parameters. In this context, it would be interesting to examine the losses in such a permanently bent fiber when it is subjected to different chemical environmental conditions and the subsequent development of different microbend sensors for various chemical applications.

3.1 Theoretical Background

In order to explain and characterise the performance of a microbend fiber sensor, both ray and wave approach can be used. It is found that both approaches give mutually

agreeable results with experimental observations. The modal approach developed by Marcuse and Lagakos is followed and is given below [26, 50-56].

When a fiber is bent into a periodic series of bends having small radii, optical power transmitted through the fiber is coupled between the m^{th} and n^{th} mode so that the spatial frequency of the perturbation satisfies the condition

$$\lambda = \frac{2\pi}{\beta_m - \beta_n} \quad (3.1)$$

where each mode has a propagation constant $\beta_m = n_1 k \cos(\theta_m)$, with θ_m representing the angle which the mode's equivalent ray makes with the fiber axis. If the core index is n_1 and the cladding index is n_2 , each guided mode has discrete propagation constant between $n_1 k$ and $n_2 k$. Energy coupled into a radiation mode, $\beta < n_2 k$, is lost. There are no modes with $\beta > n_1 k$, and there is a continuum of radiation modes with $\beta < n_2 k$. Furthermore, many degenerate modes exist; each m represents a group of modes with nearly identical propagation constants. The total number M of such modal groups is a not the same as the total number of guided modes. A general fiber will have a power law refractive index profile as,

$$n^2(r) = n^2(0) * [1 - 2\Delta(r/a)^\alpha] \quad (3.2)$$

where

$$\Delta = \frac{n^2(0) - n^2(a)}{2n^2(0)} \quad (3.3)$$

Here $n(0)$, $n(r)$ and $n(a)$ are the refractive indices at distances $0, r$ and a from the fiber axis, respectively, a is the core radius and α is a constant. Applying the WKB approximation to the solution of the dielectric waveguide problem, it can be shown that the distance in β space between adjacent guided modes is given by

$$\beta_{m+1} - \beta_m = \frac{2}{a} \left(\frac{\alpha\Delta}{\alpha+2} \right)^{1/2} \left(\frac{m}{M} \right)^{(\alpha-2)/(\alpha+2)} \quad (3.4)$$

In the case of step index fibers where $\alpha = \infty$, the spacing is given by

$$\beta_{m+1} - \beta_m = \frac{2\sqrt{\Delta}}{a} \frac{m}{M} \quad (3.5)$$

This means that the separation of modes in β space depends on the order of the modal groups m . In the case of a graded-index fiber (parabolic) with $\alpha=2$, the spacing is given by

$$\beta_{m+1} - \beta_m = \frac{\sqrt{2\Delta}}{a} \quad (3.6)$$

Therefore, the distance between modal groups in β space is a constant. In other words, the modes are spaced evenly in β space. This means that one fixed spatial frequency of the microbends will transfer power back and forth between all pairs of adjacent modes. For the step index case, however, the spacing between modes is dependent on the mode index. A particular λ will couple light between one specific pair of modes. Fig 3.3 shows how the modes are spaced for each type of the fiber; each vertical line indicates the location of β_m as a function of m . The total number of modal groups M can be determined by ascertaining how many modes will fit into the allowed β space ($n_2 k < \beta < n_1 k$), and the number of modal groups is related to the total number of modes by

$$N = M^2 \text{ (step index or graded index fiber)} \quad (3.7)$$

For the step index case, in theory, energy will be transferred back and forth in one specific mode pair. In practice, therefore, mode coupling is induced among the modes in the neighbourhood of β space, and this region will be somewhat wider in the higher order mode regime than among the lower order modes, whose spacing varies more rapidly. As the number of modes in a step index fiber becomes larger, the mode spacing for the higher order modes varies much more slowly from mode to mode than for a step index fiber supporting a small number of modes. For many mode step index fiber, the highest order modes are spaced at virtually identical intervals.

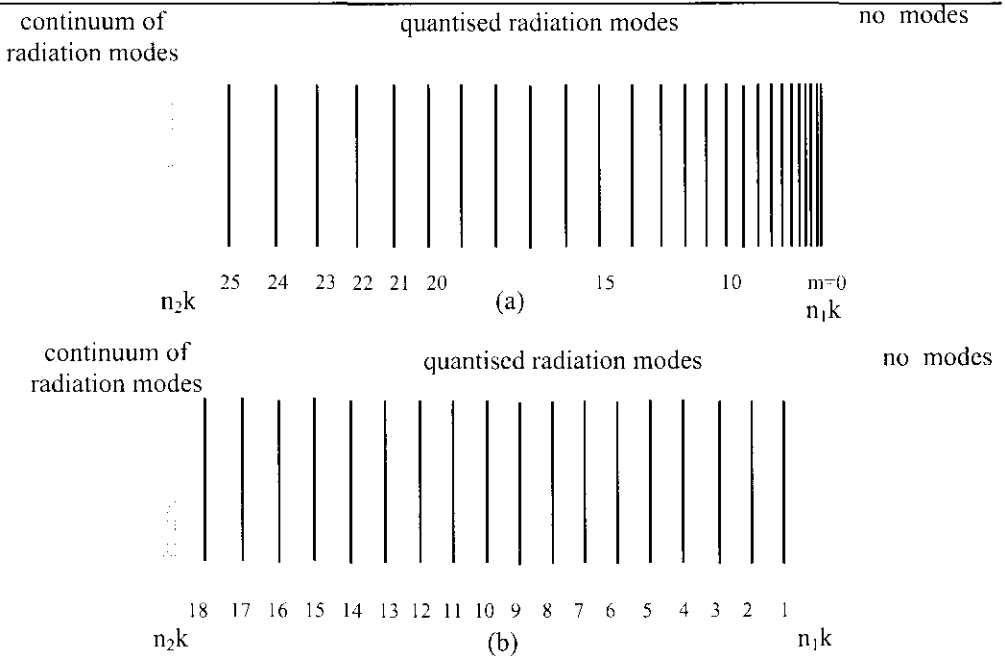


Figure 3.3: Mode group spacing for two fibers of the same parameters ($a=25 \mu\text{m}$, $n_1=1.45$, $n_2=1.4316$, $\Delta=0.01267$, $\lambda=1 \mu\text{m}$). (a) Graded index fiber carries $N=328$ modes or $M=18$ modal groups. (b) Step index fiber carries $N=656$ modes or $M=25$ modal groups.

We can see that in the case of a step index fiber, higher order modes having large m can be coupled with small periodicity λ . The critical value of λ (λ_c) which is required for coupling of guided power to leaked power occurs when $m=M$ and can be found out by equating (1) and (5) to obtain

$$\lambda_c = \frac{\pi a}{\sqrt{\Delta}} = \frac{\sqrt{2}\pi a n_0}{NA} \quad (3.8)$$

However, for a parabolic index fiber the critical value of periodicity λ is

$$\lambda_c = \frac{\sqrt{2}\pi a}{\sqrt{\Delta}} = \frac{2\pi a n_0}{NA} \quad (3.9)$$

This implies that for a reasonable multimode fiber (N in thousands), the difference in microbend sensor sensitivity between step index and graded fibers will be small. The graded index fiber exhibits a resonant response whereas the step index fiber exhibits a threshold response for the detection of various physical variables. However, a graded index fiber will ultimately have a greater dynamic range, due to the accessibility of

the power from the low-order modes, which can be coupled into higher modes by the same spatial bend frequency that causes the loss.

This approach of mode coupling between neighbouring modes is valid for small bending amplitudes only. However, for larger bending amplitudes, the guided power from even lower order modes can be coupled to leaky modes and back. Since the bending is periodic, this coupling from the core to cladding modes is of oscillatory nature. The leaky modes thus generated consist of both cladding and radiation modes. The radiation modes escape out of the core and the cladding, whereas the cladding modes continue to propagate along the fiber. After the bent portion of the fiber, there is little power- coupling between guided and unguided modes and they continue to propagate without much interaction. This power in the cladding modes can be measured by placing an index matching liquid over the cladding of the fiber just beyond the bent portion. Such a measurement scheme is termed as the dark field detection configuration. Likewise, the power that is carried by the core modes is determined in the bright-field detection configuration.

3.1.1 Generic fiber microbend sensor

Consider an idealised generic microbend sensor consisting of a sensing fiber sandwiched between a pair of deformer plates. The deformer, in response to an appropriate environmental change ΔE , applies a force ΔF to the bent fiber causing the amplitude of the fiber deformation X to change by an amount ΔX . The transmission coefficient T for light propagating through the bent fiber is in turn changed by an amount ΔT so that

$$\Delta T = \left(\frac{\Delta T}{\Delta X} \right) D \Delta E \quad (3.10)$$

where

$$D \Delta E = \Delta X \quad (3.11)$$

Here D is a constant which depends on the given environment change ΔE . In terms of the applied force ΔF , (10) becomes

$$\Delta T = \left(\frac{\Delta T}{\Delta X} \right) \Delta F \left(K_f + \frac{A_s Y_s}{l_s} \right)^{-1} \quad (3.12)$$

where K_f is the bent fiber force constant and $A_s Y_s / l_s$ is the force constant involved in changing the length of the deformer spacers. Here A_s , Y_s and l_s are the cross-sectional area, Young's modulus and length of the deformer spacers. Depending on the construction of the deformer, various environmental parameters can be sensed in principle. The deformer converts the change in the environmental parameter ΔE to a force ΔF on the bent fiber, i.e.

$$\Delta F = \Delta E C \quad (3.13)$$

For a pressure sensor, C is simply equal to the area of the deformer A_p . Thus (3.12) becomes

$$\Delta T = \left(\frac{\Delta T}{\Delta X} \right) A_p \left(K_f + \frac{A_s Y_s}{l_s} \right)^{-1} \Delta P \quad (3.14)$$

where ΔP is the change in pressure. Thus, a high sensitivity pressure sensor should have $A_s Y_s / l_s$ small so that the effective compliance is determined by that of the bent fiber which itself is quite large. In this case (14) becomes

$$\Delta T = \left(\frac{\Delta T}{\Delta X} \right) \cdot A_p K_f^{-1} \Delta P \quad (3.15)$$

Similarly for a temperature sensor

$$\Delta T = \left(\frac{\Delta T}{\Delta X} \right) \cdot \alpha_s l_s \Delta \theta \quad (3.16)$$

α_s is the thermal expansion coefficient of the spacers and $\Delta \theta$ is the temperature change.

For an acceleration sensor

$$\Delta T = \left(\frac{\Delta T}{\Delta X} \right) \cdot m_p K_f^{-1} \Delta a \quad (3.17)$$

m_p is the mass of the deformer plate and Δa is the acceleration level. Hence, by knowing the performance of the generic sensor, the response of a specific sensor can be separately determined.

3.2 Experimental

The deformer plates are made with a high tensile plastic material. A series of permanent microbends are introduced onto a 30 cm bare step index plastic fiber of

core diameter 380 μm and numerical aperture 0.3, by sandwiching the fiber with a pair of corrugated plates and applying moderately high pressures of a few atmospheres. The pitch of the corrugation is 1 mm and total length of three different plates used are 20 mm, 40 mm and 60 mm. A schematic diagram of the experimental setup is shown in fig 3.4.

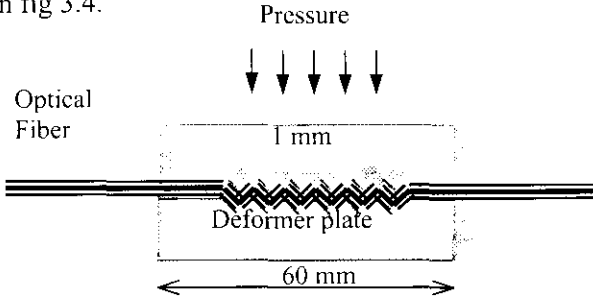


Fig 3.4: The schematic sketch of the corrugation plate used for deformations

A typical plot obtained for a weight sensor is given in fig 3.5 which is obtained by placing standard weights over the deformer plate covering the fiber.

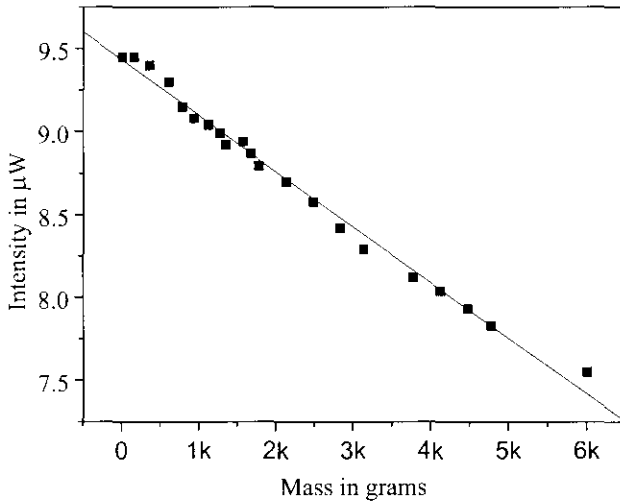


Figure 3.5: The response of a fiber optic weight sensor

The bent portion of the fiber is immersed in a cell containing methylene blue dye (Qualigens, India) dissolved in water, the absorption peak of which is at 664 nm. This is obtained using a spectrophotometer and is shown in fig 3.6. A 5 mW laser

diode (Imatronic, UK) operating at 670 nm is used to power the sensor since this wavelength is near the peak absorption wavelength of methylene blue (MB) dye.

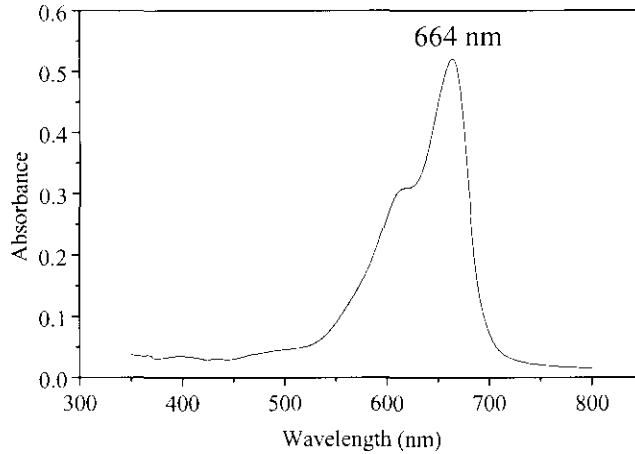


Fig 3.6: Absorption spectrum of Methylene blue dye in water

The cladding modes generated at the sensing region are detected by placing a liquid crystal, which acts as an index matching liquid, just beyond the sensing region. The power carried by the cladding modes and core modes are independently measured for various concentrations of MB dye by two laser power meters D_1 (EG&G Gamma Scientific 460-1A) & D_2 (Metrologic 45-545) respectively. The schematic of the experimental set-up is shown in fig 3.7.

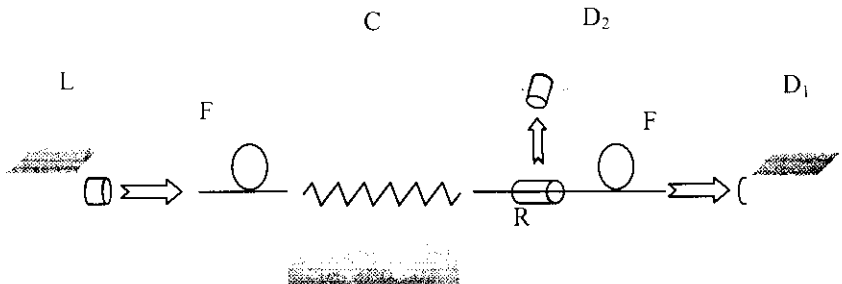


Figure 3.7: Experimental Set-up L: Diode Laser (670 nm), C: Cell containing the dye methylene blue, F: Optical Fiber, R: Index Matching Liquid, D_1 : Detector 1, D_2 : Detector 2

3.3 Results and Discussion

The measurements are carried out in two detection configurations. The first one is the bright field detection scheme in which we measure the core mode intensity by using

the detector D_1 . Figure 3.8 shows variation of core mode intensity from the microbent fiber as a function of logarithm of concentration of the absorbing species (MB dye) surrounding the bent portion of the optical fiber. From the plot, it is clear that the dynamic range of the present sensor is about 6 orders of magnitude.

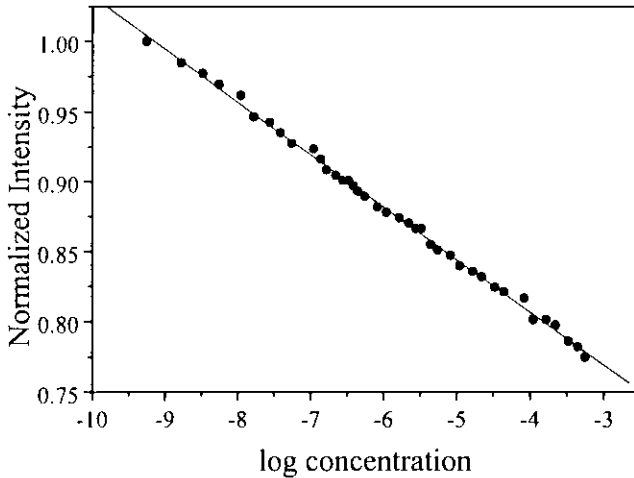


Fig 3.8: Plot showing the core-mode intensity variation with dye concentration

The observed effect can be explained as follows. It has been proven theoretically as well as experimentally that when periodic microbending is induced along the fiber axis, light power is coupled between modes. Conventional microbend sensors work on the principle that when a fiber is subjected to squeezing in between a pair of corrugated plates, a loss of transmitted intensity takes place by virtue of mode coupling between guided modes (core modes) and the leaky modes consisting of both cladding modes and radiation modes. Of these two, the radiation modes will leak out of the fiber, core as well as cladding, into the surrounding medium whereas the cladding modes will travel through the fiber. The functioning of the present sensor can be attributed to the absorption of evanescent waves which penetrate out from the cladding to the surrounding medium. Therefore, the behaviour of the present sensor is expected to be similar to that of an evanescent wave fiber optic sensor, which is usually fabricated by removing the cladding from a portion of the optical fiber.

The experimental observations confirm the fact that the bent portion of the fiber essentially behaves as an unclad region of a multimode fiber which is conventionally used for evanescent wave spectroscopy. The behaviour of such a fiber in the bright field configuration can be approximated by the relation

$$P(l) = P_0 \left[\sum_i \exp(-\gamma_i Cl) \right] \quad (3.18)$$

where P_0 is the output power obtained without any absorbent surrounding the sensing region, which is the bent portion or the unclad portion. γ_i are the molar evanescent wave absorption coefficients of different modal groups in a multimode fiber having different penetration depths, C is the concentration of the absorbing species, l is the length of the sensing region and $P(l)$ is the power output in the presence of an absorbent. The conventionally used expression for evanescent wave spectroscopy is²¹

$$P(l) = P_0 \exp(-\gamma Cl) \quad (3.19)$$

This is valid only in a small range of operation of approximately one order of magnitude. This can be readily seen as an approximation of the equation (18). So, in a short range of operation, the above equation is valid, but the value of γ changes with the region of operation.

Fortunately, this kind of behaviour makes it possible for the present sensor to act as a logarithmic detector with a large dynamic range as shown in fig 8. However, the mode coupling process is a reversible phenomenon so that the power transferred to the cladding modes will again be coupled back to the core modes. The radiation intensity thus coupled back will depend on the absorption of the medium surrounding the cladding. Such a recoupling of the cladding mode power is considered to be the major contributing factor to the observed variation of guided mode intensity with change in absorbance of the surrounding medium.

It should be noted that the amount of power recoupled from cladding modes to core modes need not be cent percent. Hence, beyond the sensing region some power will be transmitted through the fiber as cladding modes also, which is utilised in the second configuration called dark field detection scheme.

To detect the power carried by the cladding modes, an index matching liquid is placed surrounding the bare optical fiber just beyond the sensing region. A part of the power leaked out through the index matching liquid is detected using the detector D_2 . The plot showing the dependence of the intensity of the cladding modes on the dye concentration is given in fig 3.9.

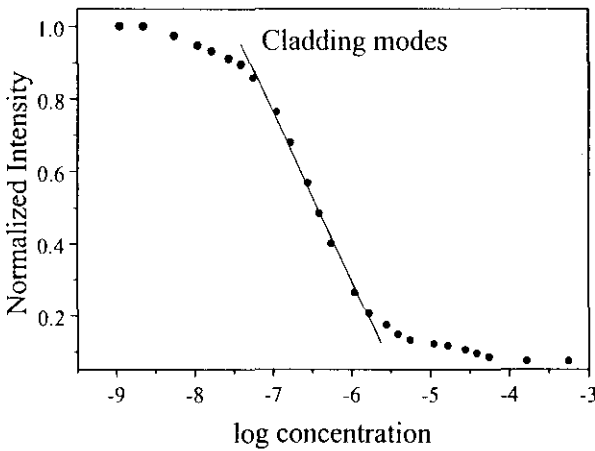


Fig 3.9: Plot showing the cladding-mode intensity variation with dye concentration

It can be clearly seen that the sensitivity using dark field detection scheme is higher in the concentration range 10^{-7} to 10^{-5} moles/litre compared to the bright field detection technique. Comparison of figs 3.8 and 3.9 shows that the bright field detection configuration has a larger dynamic range.

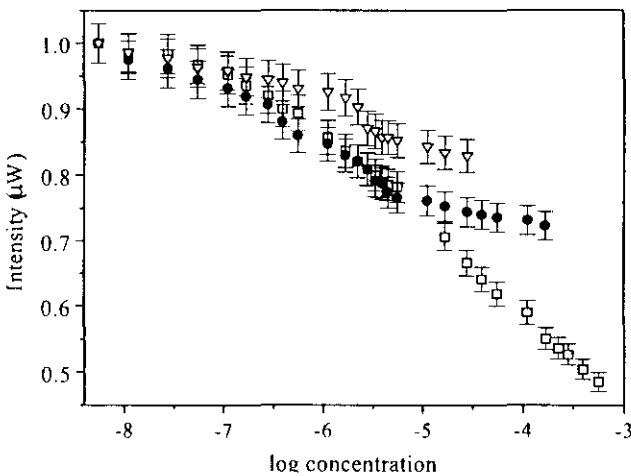


Fig 3.10: The influence of bent length on the sensitivity of the sensor in the bright field detection scheme ($a = 70$ mm $b = 40$ mm $c = 60$ mm)

3.3.1 Sensitivity dependence on bending length and bending amplitude

Fig 3.10 shows the variation of the bright field intensity as a function of concentration of MB dye for different sensing lengths. The minimum detectable limit of the sensors of various lengths is about 10 ppb. It may be noted that the variation in the output power is a logarithmic function of concentration and hence the sensitivity is range dependent. The detection level for a 60 mm microbent fiber in the concentration range 10ppb-100ppb is about 10ppb, where as in the concentration range 100ppb-1ppm it is 100ppb and in the 1ppm-10ppm range, 1ppm. Moreover, the detection level of the sensor changes with the length of the microbent region of the fiber. The detection levels for 60 mm, 40 mm and 20 mm microbent fibers in the range 100ppb-1ppm are 100ppb, 150 ppb and 200ppb respectively. The coupling strength of optical power between the guided modes and leaky modes is dependent on the periodicity of deformation and the amplitude of deformation, but not on the length of deformation or the total number of bends. However, mode coupling is a periodic phenomenon, so that as the number of bends increases, the number of times core modes being coupled to clad modes also increases. The evanescent field of these cladding modes determines the sensitivity of the device which will increase with the deformation length also. Therefore, the sensitivity in a particular range of the sensor can be expected to be directly proportional to the number of bends which in turn is determined by the length of the corrugations.

The fig 3.11 shows the effect of bending amplitude on the sensitivity in the bright field detection scheme. The detection limit of the sensors fabricated with large bending amplitude and small bending amplitude in the range of concentration 1ppm-10ppm are 0.7ppm and 5ppm respectively. It can be readily seen that the sensitivity increases with the bending amplitude. This may be because, as the bending amplitude increases, more and more lower order guided modes get coupled to cladding modes. Hence, the evanescent field at the cladding-absorbing solution increases resulting in a larger attenuation of evanescent field of cladding modes resulting in an enhanced sensitivity.

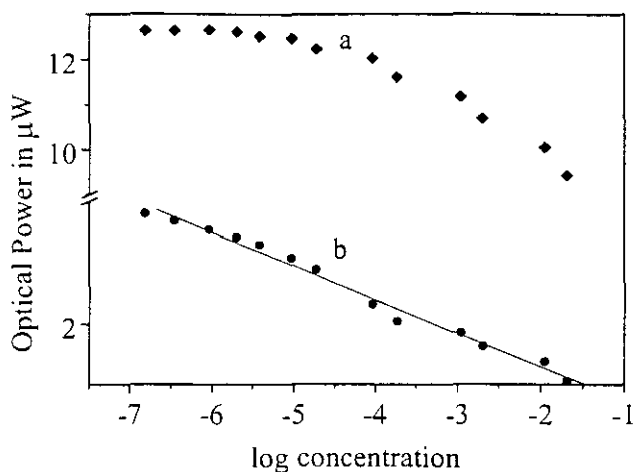


Figure 3.11: The effect of bending amplitude on the sensitivity of the microbent fiber optic sensor in the bright field detection configuration for a sensing length of 60 mm (a = low pressure, b = high pressure)

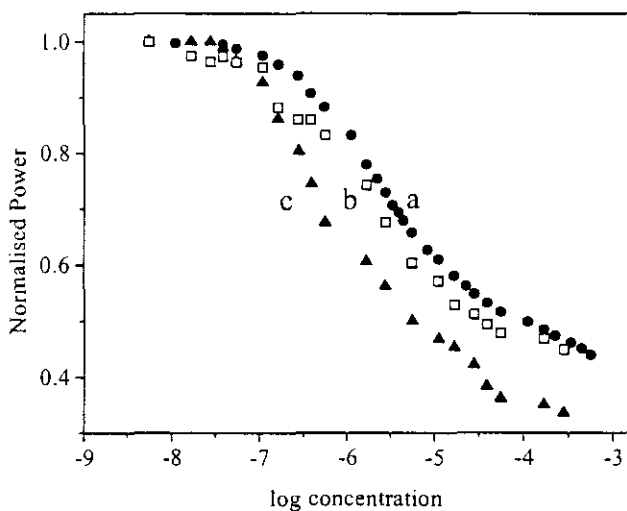


Figure 3.12: The effect of effect of bent length for the sensor in the dark field detection configuration. (a = 60 mm, b = 40 mm, c = 20 mm)

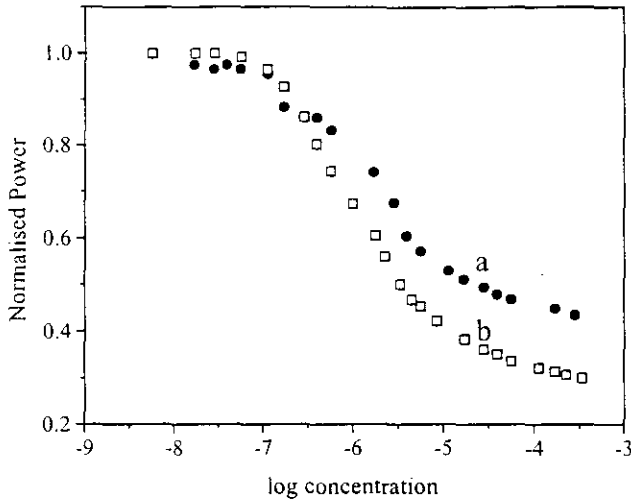


Figure 3.13: The effect of bending amplitude on the sensor response for the dark field detection configuration (relatively low pressure (a) and high (b))

The figs 3.12 and 3.13, respectively gives the effect of number of bents and bending amplitude on the sensitivity in the dark field detection scheme. The profiles for the dark filed configuration at different bending amplitudes and bent lengths are more or less the same. This suggests that the sensitivity is independent of both these parameters at least in the range of values used in the present investigation. This is understandable because, the total power coupled to the cladding modes is governed by the bending amplitude and the number of times this coupling takes place is determined by the bent length. Nevertheless, the fraction of the cladding power that will be modulated by varying the absorbance of the medium surrounding the bent portion is independent of both these parameters. This may be the reason for the observed effect of non-dependence nature of sensitivity on the bending amplitude and bent length in the dark field detection technique.

3.3.2 Microbent pH sensing

Figs 3.14 and 3.15 show the variation of the optical power corresponding to the core modes and cladding modes respectively, with respect to different values for pH of the solution surrounding the sensing region of the fiber. The sensor is fabricated by

coating the bent portion of the fiber with dye doped sol-gel material. It can be seen that the core mode

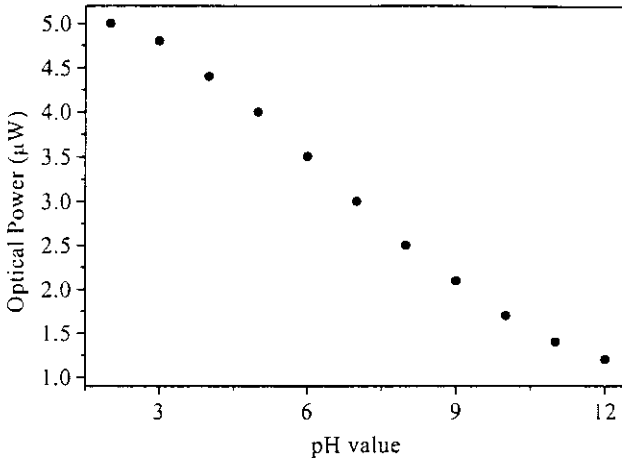


Figure 3.14: The variation of core mode power with respect to the pH of the surrounding solution

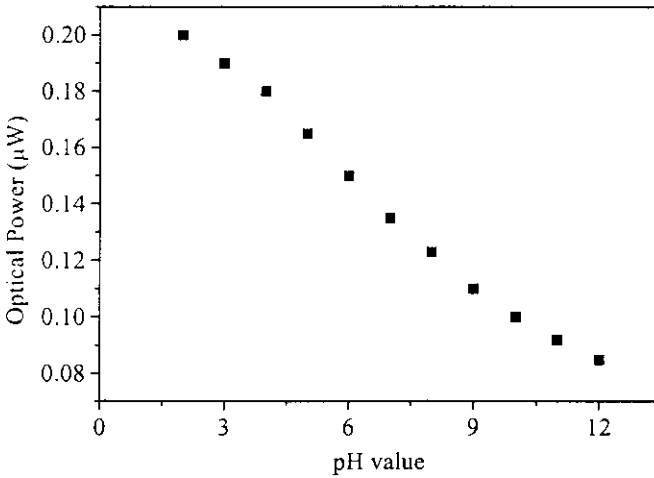


Figure 3.15: The variation of cladding mode power with respect to the pH of the surrounding solution

power variation and the cladding-mode power variation are similar to that obtained with a conventional unclad EWFS [57-61]. However, it may be noted that the sensitivity in the bright-field detection scheme is greater than that in the dark field detection scheme. The apparent contradiction in the case of sensitivity against that

described in [62] is a result of the effect of the microbending amplitude, which has lesser effect on the optical power in the cladding mode. The dynamic range of the present sensor system is large and it covers 3-11 pH units. It should also be noted that the present sensor uses a double detection scheme which is certainly an advantage over conventional sensors. This aspect provides a double check and thus greater reliability for the measurements. It is also observed that the graphs obtained are independent of the direction of the change in pH value of the solution. i.e. a low to high pH variation gives the same curve as a high to low pH variation.

3.3.3 Microbent refractometry

The variation of the cladding mode power with respect to the refractive index of the medium surrounding the bent portion of length 60 mm of the fiber is shown in fig 3.16. Standard solutions of different refractive indices are prepared by dissolving known quantity of NaCl and CaCl₂ in water.

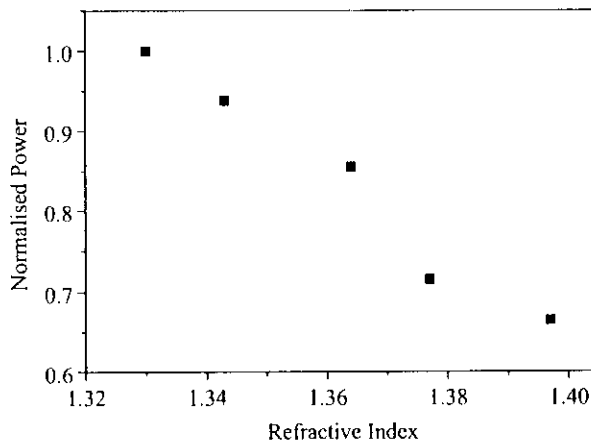


Figure 3.16: The variation of cladding mode power with respect to the refractive index of the surrounding solution (sensing length = 60 mm)

The finite thickness of the cladding makes the effective refractive index of the cladding to be a function of the refractive index of the surrounding medium also. Therefore, the fraction of the power coupled to the cladding modes is dependent on the refractive index of the medium surrounding the bent portion. The variation of the power can be attributed to this change in the effective refractive index of the cladding

of the fiber. Figs 3.17 and 3.18 show the power variation of the bent sensor with sensing length 40 mm and 20 mm respectively.

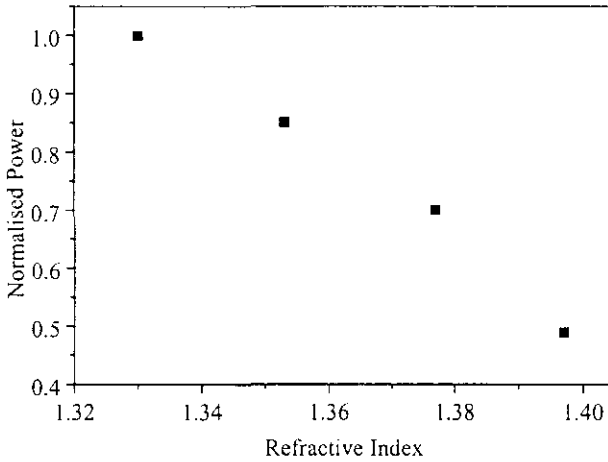


Figure 3.17: The variation of cladding mode power with respect to the refractive index of the surrounding solution (sensing length = 40 mm)

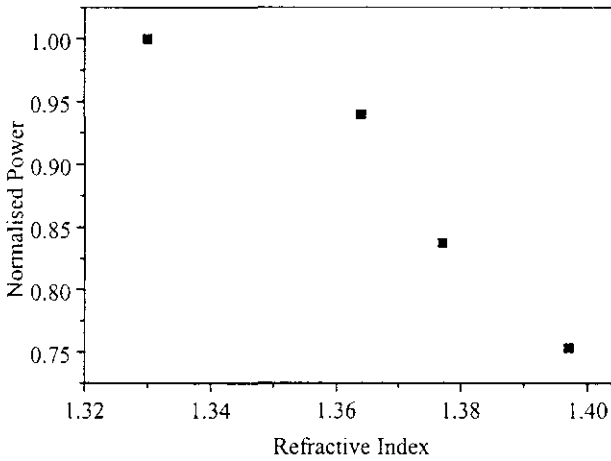


Figure 3.18: The variation of cladding mode power with respect to the refractive index of the surrounding solution (sensing length = 20 mm)

The core mode intensity also shows some variation with respect to the refractive index of the solution surrounding the bent portion of length 60 mm, but with less repeatability and sensitivity, which is shown in fig 3.19.

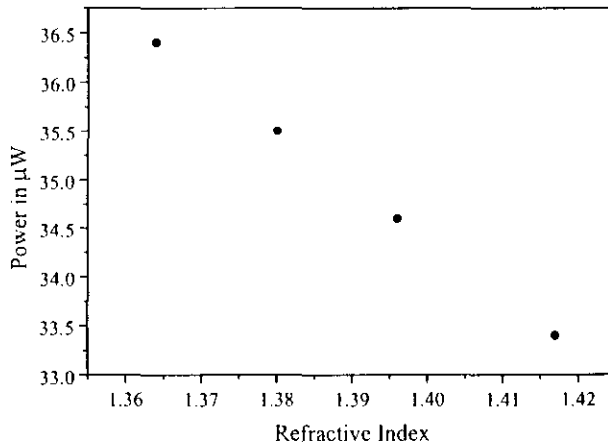


Figure 3.19: The variation of core mode power with respect to the refractive index of the surrounding solution (sensing length = 60 mm)

This chapter details the development of fiber optic chemical sensors based on permanently microbent multimode plastic fibers. A Microbent fiber is used for measuring both the real and imaginary part of the refractive index of the medium surrounding its bent portion. They are as competitive as conventional evanescent field fiber sensors, since in addition to a double detection scheme they employ inexpensive plastic fibers.

References:

1. Murtaza G, Jones S L and Senior J M, *Fiber and integrated optics* **20**, 53 (2001)
2. Pierce S G, MacLean A and Culshaw B, *App. Opt.* **39**, 4569 (2000)
3. Xie G P, Keey S L and Asundi A, *Optics And Lasers In Engineering*, **32**, 437 (1999)
4. Donlagic D and Culshaw B, *Phys. Lett.* **76**, 2331 (2000)
5. Donlagic D and Culshaw B, *J. Lightwave Tech* **17**, 1856 (1999)
6. W C Michie, B Culshaw, I McKenzie, M Konstantakis, N B Graham, G Moran, F Santos, E Bergqvist and B Carlstrom, *Opt. Lett.* **20**, 103 (1995)
7. A. MacLean, C. Moran, W. Johnstone, B. Culshaw, D. Marsh, V. Watson and G. Andrews, OFS 2000, 14th International Conference on Optical Fiber Sensors, 11-13 October 2000, Venice, Italy
8. Luo F, Liu J Y, Ma N B and Morse T F, *Sens. Act. A*, **75**, 41 (1999)
9. Stolken J S and Evans A G, *Acta Materialia*, **46**, 5109 (1998)
10. Yoshino T, Inoue K and Kobayashi, *IEE Proc.-Optoelectronics*, **144**, 145 (1997)
11. Donlagic D and Završnik M, *Opt. Lett.* **22**, 837 (1997)
12. Hastings M C, Chiu B and Nippa D W, *Nuclear Engineering And Design*, **167**, 239 (1997)
13. Jonathan D Weiss, *J. Lightwave Tech.* **7**, 1308 (1989)
14. Betty Lise Anderson, Jill A Brosig, *Opt. Engg.* **34**, 108 (1995)
15. Jones S L, Murtaza G, Senior J M and Haigh N, *Opt. Fib. Tech.* **4**, 471 (1998)
16. Kumar S and Dixit H K, *J. Inst. Elec. Tele. Engineers*, **40**, 197 (1994)
17. Arya V, Murphy K A, Wang A B and Claus R O, *J. Lightwave Tech.* **13**, 1998 (1995)
18. Suopajarvi P, Lyori V, Nissila S, Kopola H and Johansson R, *Indicating Opt. Engg.* **34**, 2587 (1995)
19. McCollum T, Spector G B, *Rev. Sci. Instru.* **65**, 724 (1994)
20. Sampson D D, Read I J, *Elec. Lett.* 1992, Vol 28, Iss 21, Pp 1961-1962
21. Emge S R and Chen C L, *Array Sens. Act. B*, **3**, 31 (1991)
22. Vengsarkar A M, Murphy K A, Tran T A and Claus R O, *J. Acou. Soc. Am.* **88**, 419 (1990)
23. Jenstrom D T; Chen C L, *Sens. Act.* **20**, 239 (1989)
24. Lagakos N; Bucaro J A, *ISA Trans.* **27**, 19 (1988)
25. Wlodarczyk M T, *Opt. Lett.* **12**, 741 (1987)
26. Nicholas Lagakos, J H Cole and J A Bucaro, *App. Opt.* **26**, 2171 (1987)
27. Berthold J W, Miers D R and Varshneya D, *Am Cer. Soc. Bull.* **64**, 1337 (1985)
28. Mavadat R, *Sens. Act.* **6**, 289 (1984)
29. Callaghan M A, *Sens. Act.* **6**, 113 (1984)
30. Diemeer M B J and Trommel E S, *Opt. Lett.* **9**, 260 (1984)
31. Horsthuis W H G and Fluitman J H J, *Sens. Act.* **3**, 99 (1983)
32. Yao S K, Asawa C K and Lipscomb G F, *Elec. Lett.* 1983, Vol 19, Iss 7, Pp 257-258
33. Yao S K and Asawa C K, *Proc. SPIE*, **412**, 9 (1983)
34. Yao S K, Asawa C K and Lipscomb G F, *Appl. Opt.* **21**, 3059 (1982)
35. Asawa C K, Yao S K, Stearns R C, Mota N L and Downs J W, *Elec. Lett.* **18**, 362 (1982)
36. Lagakos N, Trott W J, Hickman T R, Cole J H and Bucaro J A, *IEEE J. Quan. Elec.* **18**, 1633 (1982)
37. W B Spillman Jr., *Opt. Lett.* **7**, 388 (1982)

38. J W Berthold III, IEEE J. Lightwave Tech. **13**, 1193 (1995)
39. N Chandrasekaran and Pradeep Kumar, J. Instrum. Soc. India, **30**, 151 (2002)
40. W B Spillman Jr. and D H McMahon, Appl. Phys. Lett. **37**, 145 (1980)
41. W B Spillman Jr. and D H McMahon, Appl. Opt. **19**, 113 (1980)
42. J N Fields and J H Cole, Appl. Opt. **19**, 3265 (1980)
43. S T Shiue and T Y Shen, Modelling and Simulation in Materials Science and Engineering, **9**, 207 (2001)
44. T G Giallorenzi, J A Bucaro, A Dandridge, G H Sigel, J H Cole, S C Rashleigh and R G Priest, IEEE Trans. On Microwave Theory and Tech. **30**, 472 (1982)
45. R M Bunch, Am. J. Phys. **58**, 870 (1990)
46. N Lagakos, T Litovitz, P Macedo, R Mohr and R Meister, Appl. Opt. **20**, 167 (1981)
47. Anderson B L and Qi Z, O Appl. Opt. **34**, 8082 (1995)
48. Czaplak D S, Rashleigh S C, Taylor H F and Weller J F, J. Lightwave Tech., **4**, 50 (1986)
49. A J Romano, J A Bucaro and J J Shirron, J. Lightwave. Tech. **14**, 1992 (1996)
50. D Marcuse, Bell Syst. Tech. J. **51**, 229(1972)
51. D Marcuse, Bell Syst. Tech. J. **51**, 1199 (1972)
52. D Marcuse, Bell Syst. Tech. J. **52**, 817 (1973)
53. D Marcuse, Bell Syst. Tech. J. **52**, 1423 (1973)
54. D Marcuse, Theory of dielectric optical waveguides, Academic Press, New York (1974)
55. D Marcuse, J. Opt. Soc. Am. **66**, 216 (1976)
56. D Marcuse, J. Opt. Soc. Am. **66**, 311 (1976)
57. T M Butler, B D MacCraith and C McDonagh, J. Non. Crys. Solids, **224**, 249 (1998)
58. J Y Ding, M R Shahriari and G H Sigel, Elec. Lett. **27** 1560, (1991)
59. B D Gupta and D K Sharma, Opt.Comm. **140** 32, (1997)
60. B D Gupta and Sonu Sharma, Opt. Comm. **154** 282 (1998)
61. Andrej Holobar, Bernhard H Weigl, Wolfgang Trettnak, Roman Benes, Hartmut Lehmann, Nena V Rodriguez, Arnold Wollschlager, Paul O'Leary, Peter Raspor and Otto S Wolfbeis, Sens Act. B, **11** 425 (1993)
62. Thomas Lee S, Nibu A George, P Sureshkumar, P Radhakrishnan, C P G Vallabhan and V P N Nampoori Opt. Lett, **26**, 1541 (2001)

Interferometric Weight & Displacement Sensor and Pollution Monitoring Sensors for Fe³⁺ & Mn²⁺ Detection

Introduction

Fiber optic sensors are extensively used for pollution monitoring and environmental sensing [1-25]. Moreover, they find extensive applications in various physical parameter measurement when used in the fiber interferometric configuration [26-56]. In the present chapter, we concentrate on the development of phase modulated sensors for displacement and weight measurement, and intensity modulated sensors for aqueous iron and manganese detection. In addition, a new referencing technique for intensity modulated sensors is also proposed.

4.1 Phase modulated optical fiber sensors

Phase modulation of light has been increasingly exploited as a highly sensitive technique for monitoring environmental changes over the past hundred years. The principal attraction of optical phase modulation is its intrinsically high sensitivity to environmental modulation, so that very high-resolution measurements are feasible. The advantages of using fibers in interferometric sensors lie both in easing the alignment difficulties inherent in assembling interferometers with long arms, and in increasing the sensitivity of the phase modulation to the environmental parameter

simply by increasing the optical path length exposed to the measurand. A suitably designed fiber interferometer takes optical interferometry from the laboratory optical bench into a compact and mechanically rugged piece of instrumentation. Optical fiber interferometric sensors are among the most sensitive measurement devices yet developed.

Hydrophones, magnetometers, accelerometers, strain gauges, and thermometers have all been fabricated around the fiber interferometer, and all have achieved sensitivities exceeding that available from other technologies. Moreover, the dynamic range of fiber interferometers is as high as 150 dB. How much of this is actually available depends on the detection technique used to convert the phase modulation to a usable electrical signal.

The basic elements of an optical fiber interferometer are shown in fig 4.1. The modulator is included in the reference arm either to incorporate the required 90° imbalance for homodyne detection or to provide frequency offset for heterodyne detection. The beam splitters are most conveniently optical fiber 3 dB couplers, thereby, eliminating mechanical noise common with discrete optical components. However, the use of couplers does limit the scope of the modulation function to phase modulators based on mechanical stretching of the fiber using piezoelectric elements.

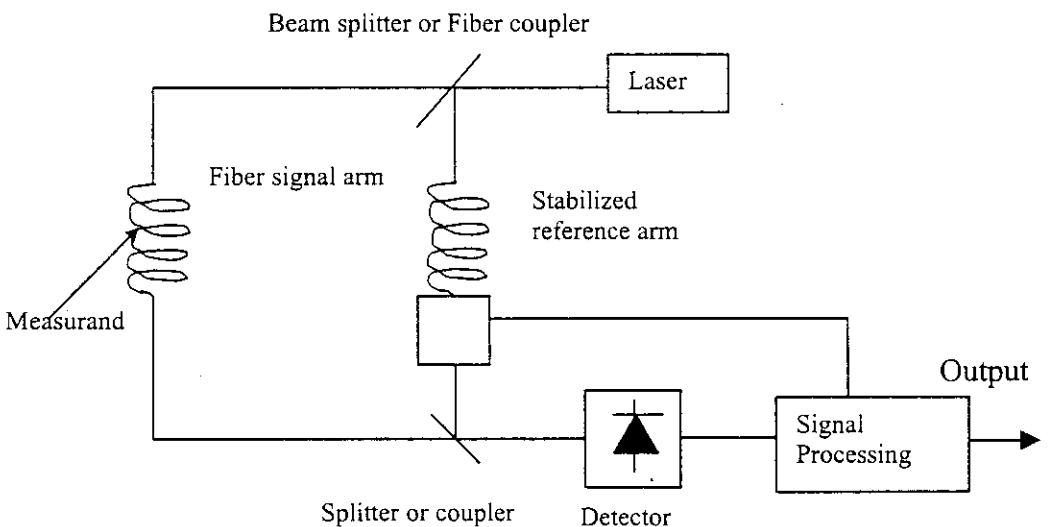


Figure 4.1: Schematic sketch of a Mach-Zehnder interferometer

4.1.1 Phase modulation mechanisms in optical fibers

The total phase of the light path along an optical fiber depends on three properties of the fiber guide:

- Its total physical length

- The refractive index and the index profile

- The geometrical transverse dimensions of the guide

It is assumed that the index profile remains constant with environmental variations, so that all the following analysis concentrates on evaluating the depth of phase modulation for variations in length, refractive index and guide dimensions alone. These variations may then be evaluated for a given perturbation applied to the fiber, and hence the phase sensitivity of the fiber to this perturbation can be estimated. The total physical length of an optical fiber may be modulated by:

- Amplitude of a longitudinal strain

- Thermal expansion

- Application of a hydrostatic pressure causing expansion via Poisson's ratio

The refractive index varies with:

- Temperature

- Pressure and longitudinal strain via photoelastic effect

And the guidance dimensions with:

- Radial strain in a pressure field

- Longitudinal strain through Poisson's ratio

- Thermal expansion

The effect of a pure change in length, δL , on the phase of light propagating in the guide is readily determined:

$$\delta\phi_L = \frac{2\pi\delta L}{\lambda_g} = \frac{2\pi L}{\lambda_g} \varepsilon_l \text{ where } \lambda_g = \frac{\lambda_0}{n} \sin\theta, \lambda_0 \text{ is the wavelength of light in the}$$

guide, θ is the angle of incidence of a ray on the core-cladding interface and ε_l is the

longitudinal strain. The effect of a change in refractive index Δn is equally readily derived to be:

$$\delta\phi_n = \frac{2\pi}{\lambda_g} L \Delta n \quad (4.1)$$

in the limit that the change in λ_g is negligible. The change in guide wavelength with core diameter is a little more complicated to derive, but the general expression:

$$\Delta\phi_d = \frac{2\pi L}{\lambda_g^2} \frac{\partial \lambda_g}{\partial d} \Delta d \quad (4.2)$$

is clear from simple geometrical considerations.

Temperature changes the refractive index and the geometrical dimensions of the fiber. The change in phase is thus

$$\Delta\phi = \frac{2\pi L}{\lambda'_g} \left\{ \alpha + \frac{\partial n}{\partial T} \right\} \Delta T \quad (4.3)$$

where α is the temperature coefficient of expansion. The effect of a pressure variation on the optical phase path may be written in the most general form as

$$\Delta\phi = \frac{2\pi L}{\lambda_g} \left\{ \varepsilon_l - \frac{n^2}{2} (P_{11} + P_{12}) \varepsilon_r + P_{12} \varepsilon_l \right\} \quad (4.4)$$

where ε_l is the longitudinal strain and ε_r the radial strain. P_{11} and P_{12} are the photoelastic constants of the silica fiber.

4.1.2 Experimental setup

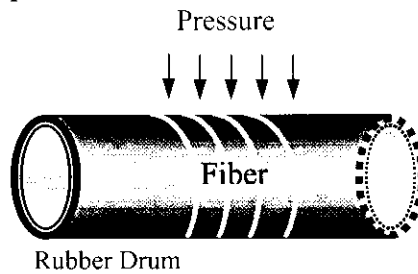


Figure 4.2: Sensing Shell

The sensing arm of the interferometer consists of a fiber wound over a hollow, elastic, cylindrical structure made of thin rubber of thickness 1 mm as shown in fig 4.2. It has been experimentally observed that the rubber tube is more sensitive and reversible than a polymer film or a paper of appropriate thickness.

The light emitted from a diode pumped solid-state laser (B&W TEK, BWT-50) operating at 532 nm and 50 mW is coupled to a fiber optic 3dB coupler using a microscope objective of NA 0.25. One arm at the output end of the coupler may be

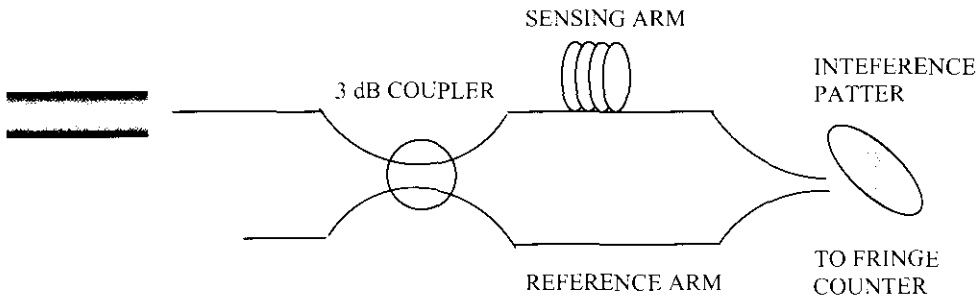


Figure 4.3: Experimental Setup

treated as the reference arm and the other as the sensing arm (sensing shell) as shown in Fig 4.3. Finally, these two arms are brought near to each other laterally and the light coming out is allowed to interfere. The interference pattern is allowed to fall on a photodiode and the signal is amplified and fed to a fringe counting system, which is used to count the number of fringes shifted when the rubber tube gets deformed. This amount of deformation is proportional to the amount of force applied on it.

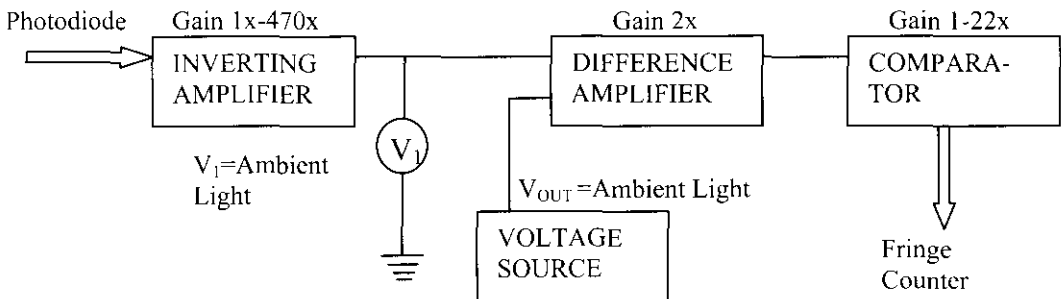


Figure 4.4: The block diagram of the photo-detector

The block diagram of the detector-fringe counter system is shown in fig 4.4.

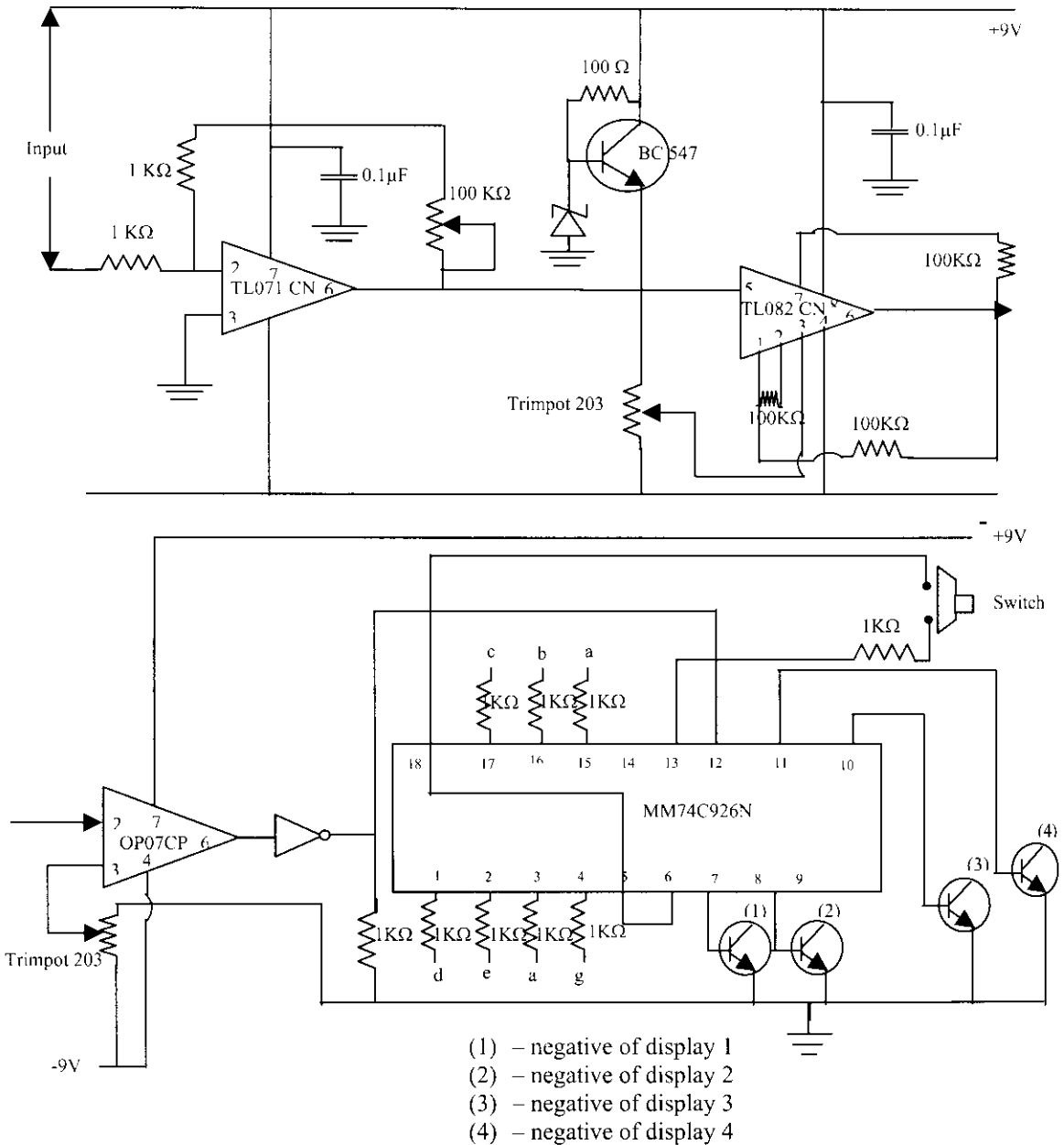


Fig 4.5: Electronic circuit for a detector-fringe counter system.

The weak signal coming from a commercially available photodiode (commercially known as photo-receiver) is amplified using a low noise operational amplifier (TL-071). The amplified signal is then fed to a double OPAMP (TL082) operating as a difference amplifier and a voltage amplifier, which nullifies the effects of ambient light intensity. The reference signal for this difference amplifier is provided by a zener diode driving a transistor (BC547) in combination with a potentiometer (trimport 203). This output is again amplified and fed to a comparator (OP07CP). Depending on the voltage set at the second trimport 203, the output of this comparator switches between +9V and -9V. Finally, the output of this third stage is fed to a standard counter IC (MM74C926N) which in turn drives a set of 4 seven segment displays through 4 transistors. Using this fringe counter 0-9999 fringes can be counted.

A compact detector-fringe counting system using the above circuit is developed and is shown in fig 4.6



Fig 4.6: Detector-Fringe counting system

4.1.3 Results and Discussion

For the displacement measurement, the rubber tube that serves as the sensing shell is held in between a platform and a micrometer screw. The displacements with a resolution of $10\ \mu\text{m}$ are made using the screw which applies a pressure in the transverse direction of the shell and the corresponding number of fringes shifted is noted. The experiment is carried out using rubber tubes of varying radii and different fiber turns. Fig 4.7 shows the sensor response curve with shell diameter of 20 mm and varying fiber turns. It can be seen that the sensitivity is a function of number of turns of the fiber. This is in agreement with the theoretically predicted results (4.1), because as the number of turns increases the total sensing length increases.

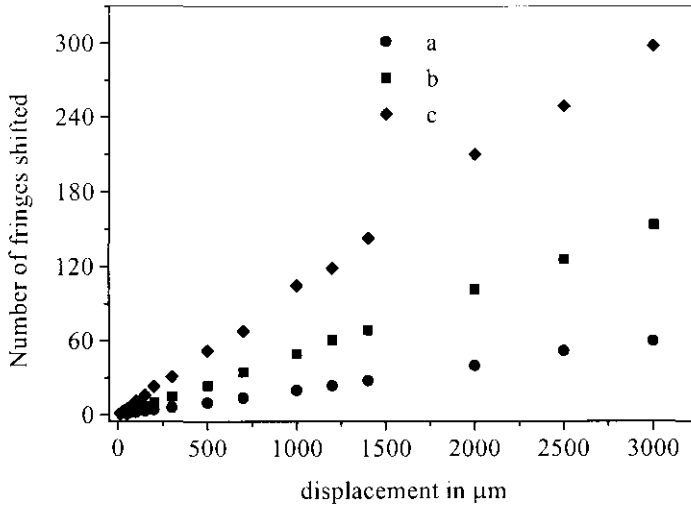


Figure 4.7: Shows the response of the displacement sensor with shell radius 20 mm for various fiber turns, $a = 1$ fiber turn, $b = 3$ turns and $c = 5$ turns

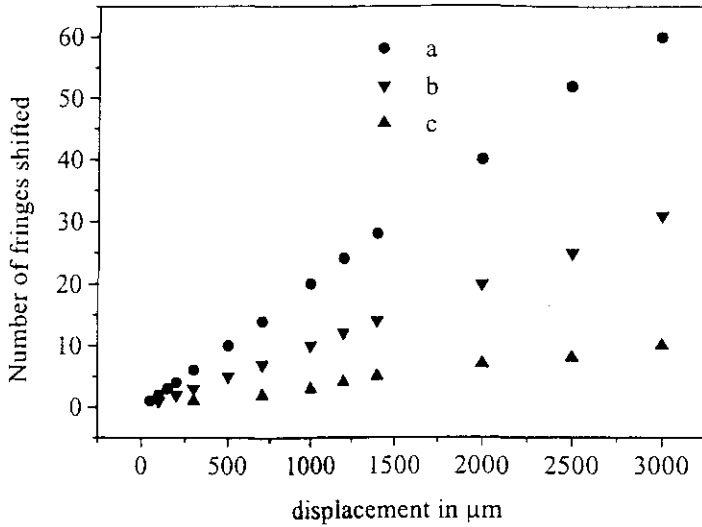


Figure 4.8: Shows the response of a single turn displacement sensor with various shell radii $a = 2 \text{ cm}$, $b = 3 \text{ cm}$ and $c = 4 \text{ cm}$

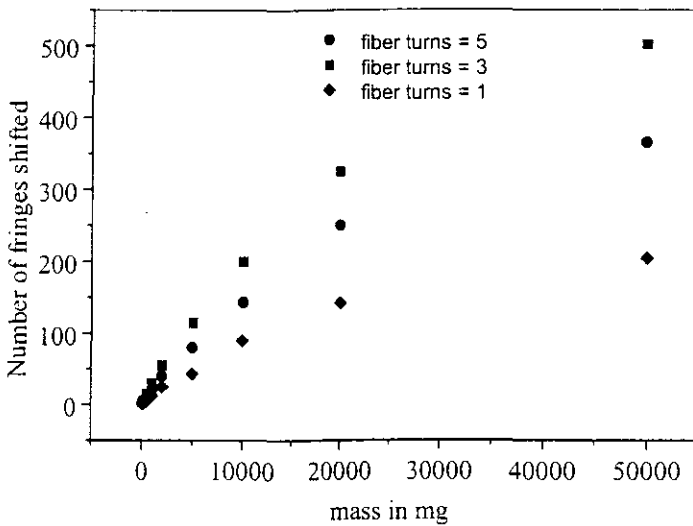


Figure 4.9: Shows the response of the weight sensor of radius 20mm, with various fiber turns, $a = 1$ fiber turn, $b = 3$ turns and $c = 5$ turns

Fig 4.8 shows the response of a single turn of the fiber for various shell radii. Here the response of the sensor is inversely proportional to the bending radius. Even

though the total sensing length decreases with the bending radius, the loss due to power coupling to radiation modes will be stronger for smaller bending radius. This may be the reason for the observed effect.

Fig 4.9 shows the response of the weight sensor response with different fiber turns for a constant fiber radius of 20 mm. It is obvious from the figure that as the number of turns increases the sensitivity correspondingly increases which is understandable on the basis of (4.1). The response of the weight sensor also varies in a similar fashion with shell radius just as in the case of the displacement sensor.

4.2 Fiber optic Fe³⁺ and Mn²⁺ detection in aqueous environments

The ever-expanding industrialization and concomitant domestic waste generation causes the release of steadily growing number of pollutants into the environment. Therefore, a great deal of attention must be paid to the pollution of natural freshwater and seawater reserves. Standards for drinking water have evolved over the years as knowledge of the nature and effects of various contaminants has grown. It is considered desirable that drinking water be free of suspended solids and turbidity. In addition, it should be tasteless, odourless and dissolved inorganic solids be in moderate quantities, and toxic substances and pathogens be absent. With further improvements in water quality standards, additional requirement may be added to this list, making drinking water quality requirements even more stringent.

Iron and manganese are minerals found in drinking water supplies. Water percolating through soil and rock can dissolve minerals containing iron and manganese and hold them in solution. Occasionally, iron pipes also may be a source of iron in water. Several factors that cause iron contamination of piped drinking water are, low chlorine residual, infrequent and insufficient hydrant flushing, low water usage, breakage of water pipes by tree roots, frost or pipe corrosion, galvanic or bacterial corrosion, presence of dissolved organic matter and heterotrophic bacteria. Iron and manganese are chemically similar and cause similar problems. Iron is the more frequent of the two contaminants in water supplies; manganese is typically found in iron-bearing water.

Iron and manganese can affect the flavor and color of food and water. In fact, vegetables cooked in iron-contaminated water turn dark and look unappetizing. In addition, they may react with tannins in coffee, tea and some alcoholic beverages to produce a black sludge, which affects both taste and appearance. Iron will cause reddish-brown staining of laundry, porcelain, dishes, utensils and even glassware. Manganese acts in a similar way but causes a brownish-black stain. Soaps and detergents do not remove these stains, and use of chlorine bleach and alkaline builders (such as sodium and carbonate) may intensify the stains. Iron and manganese deposits will build up in pipelines, pressure tanks, water heaters and water softeners. This reduces the available quantity and pressure of the water supply. Iron and manganese accumulations become an economic problem when water supply or water softening equipment must be replaced. There also are associated increases in energy costs from pumping water through constricted pipes or heating water with heating rods coated with iron or manganese mineral deposits.

Oxidation of dissolved iron particles in water changes the iron to white, then yellow and finally to red-brown solid particles that settle out of the water. Iron that does not form particles large enough to settle out and that remains suspended (colloidal iron) leaves the water with a red tint. The four forms of iron commonly found in drinking water are ferrous, ferric, organic and iron bacteria. Ferric iron precipitates or settles out. Organic iron does not settle out. In well water, insoluble iron oxide is converted to a soluble form of ferrous (dissolved) iron. In deep wells, where oxygen content is low, the iron/manganese-bearing water is clear and colorless (the iron and manganese are dissolved). Water from the tap may be clear, but when exposed to air, iron and manganese are oxidized and change from colorless, dissolved forms to colored, solid forms. Iron bacteria (a harmless bacteria), occur in soil, groundwater, and some surface waters. They thrive on iron in the sink or metal parts of the water system and are most easily seen on the inside surface of the toilet tank.

Manganese is similar to iron but forms a brownish-black precipitate and stains. Manganese is less commonly found in groundwater than iron, rarely found

alone in a water source, and generally found with dissolved iron. In fact, manganese is objectionable in water even when present in smaller concentrations than iron. Manganese usually is dissolved in water, although some shallow wells contain colloidal manganese (black tint).

The presence of iron and manganese in water is not considered health problem. In fact, small concentrations are essential to human health. However, high concentrations of iron may give the water an unpleasant metallic taste while still being safe to drink. Under guidelines for public water supplies set by the Environmental Protection Agency (EPA), iron and manganese are considered secondary contaminants. Secondary standards apply to substances in water that cause offensive taste, odor, color, corrosion, foaming, or staining but have no direct affect on health. Secondary standards set by World Health Organization [57] as well as Kerala State Pollution Control Board [58] specifies secondary contaminant level for Iron as 0.3 milligram per litre (300 ppb) and manganese as 0.05 mg/L (50 ppb). Conventional methods of iron detection are generally based on spectrophotometry and fluorescence quenching [59-63]. In addition, a few works related to fiber optic iron detection have also been reported [64-67].

In this context, it is worthwhile to develop fiber optic sensors for Fe^{3+} and Mn^{2+} detection. The characterization of the sensors is carried out using an automated data acquisition system by setting up a LabVIEW environment in the lab.

4.2.1 LabVIEW fundamentals

LabVIEW is a graphical programming language that uses icons instead of lines of text to create applications. In contrast to text-based programming languages, where instructions determine program execution, LabVIEW uses dataflow programming, where data determine execution. In LabVIEW, a user interface is built by using a set of tools and objects. The user interface is known as the front panel. One then adds code using graphical representations of functions to control the front panel objects. The block diagram contains this code. If organized properly, the block diagram resembles a flowchart. LabVIEW is integrated fully for communication with

hardware such as GPIB, VXI, PXI, RS-232, RS-485, and plug-in data acquisition devices. LabVIEW also has built-in features for connecting one's application to the Internet using the LabVIEW web server and software standards such as TCP/IP networking and ActiveX.

LabVIEW programs are called virtual instruments, or VIs, because their appearance and operation imitate physical instruments, such as oscilloscopes and multimeters. Every VI uses functions that manipulate input from the user interface or other sources and display that information or move it to other files or other computers.

A VI contains the following three components:

- **Front panel**—Serves as the user interface.
- **Block diagram**—Contains the graphical source code of the VI that defines its functionality.
- **Icon and connector pane**—Identifies the VI so that one can use the VI in another VI. A VI within another VI is called a subVI. A subVI corresponds to a subroutine in text-based programming languages.

4.2.1.1 Front Panel

The front panel is the user interface of the VI. One can build the front panel with controls and indicators, which are the interactive input and output terminals of the VI, respectively. Controls are knobs, push buttons, dials, and other input devices. Indicators are graphs, LEDs, and other displays. Controls simulate instrument input devices and supply data to the block diagram of the VI. Indicators simulate instrument output devices and display data which the block diagram acquires or generates.

4.2.1.2 Block Diagram

After one builds the front panel, he can add code using graphical representations of functions to control the front panel objects. The block diagram contains this graphical source code. Front panel objects appear as terminals on the block diagram. However, one cannot delete a terminal from the block diagram. The terminal disappears only

after one deletes its corresponding object on the front panel. Moreover, every control or indicator on the front panel has a corresponding terminal on the block diagram. Additionally, the block diagram contains functions and structures from built-in LabVIEW VI libraries. Wires connect each of the nodes on the block diagram, including control and indicator terminals, functions, and structures. LabVIEW communicates with most instruments through instrument drivers, which are libraries of VIs that control programmable instruments.

LabVIEW instrument drivers simplify instrument control and reduce test development time by eliminating the need to learn the low-level programming protocol for each application. The foundation for LabVIEW drivers is the VISA (Virtual Instrument Software Architecture) VI library, a single interface library for controlling GPIB, VXI, RS-232, and other types of instruments. Drivers using VISA are scalable across instrument I/O interfaces.

4.2.2 Experimental

For developing the sensor probe a plastic clad silica (PCS) fiber with core diameter 200 μ m and numerical aperture (NA), 0.22 is unclad over a length of 12 cm. This is done by first removing the sheath of the fiber with a sharp razor and then removing the cladding by immersing the unsheathed portion in pure HF for a minute. The bent fiber sensor uses a bare plastic fiber of core diameter 380 μ m and NA 0.3. The permanent microbents are written on the plastic fiber by pressing the fiber in between a pair of corrugation plates each having a length of 60mm and pitch 1 mm.

To calibrate the sensor standard solutions of Fe³⁺ are prepared by the thiocyanate method in which Fe³⁺ reacts with thiocyanate to give a series of intensely red-colored compounds, which remain in true solution [68]. The potassium thiocyanate solution is prepared by dissolving 20 gm of A.R. potassium thiocyanate in 100 ml distilled water. 0.864 gm of Ferric Ammonium Sulphate is dissolved in 10 ml concentrated HCl, which is further diluted to 1 liter. 1 ml of such a solution is \equiv 0.1 mg of Fe. Knowing this value, test solutions of different concentrations are prepared by again diluting the above solution as required. 40 ml of the test solution is

mixed with 5 ml of 2 M potassium thiocyanate solution and 3 ml of 4 M nitric acid, and the resultant solution is diluted to 50 ml. Fig 4.10 shows the absorption spectra of the solution with various concentrations of Fe^{3+} . It is clearly visible from the plot that the peak absorption of the solution is at 480 nm. The sensitivity of the sensor will be high if the operating wavelength is near this wavelength. This is the motivation for using the 488 nm output of an Ar^+ laser to power the sensor.

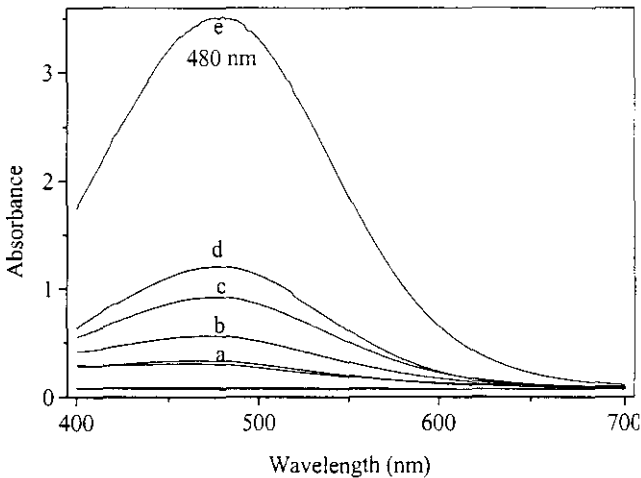


Figure 4.10: Absorption spectrum of the resulting solution containing various concentrations of Fe^{3+} ($a = 1 \text{ ppm}$, $b = 2.5 \text{ ppm}$, $c = 5 \text{ ppm}$, $d = 10 \text{ ppm}$ and $e = 25 \text{ ppm}$)

Small quantities of manganese are usually determined calorimetrically by oxidation to permanganic acid. Here an oxidizing agent like potassium periodate is used to oxidize the manganese iron. Standard potassium permanganate (Qualigens, India) solution is reduced with a little sulphite after the addition of dilute sulphuric acid (Merck, India), and the sulphur dioxide is removed by boiling. The resulting Mn^{2+} solution is diluted and oxidized with potassium periodate (Qualigens, India) to give a coloured solution with absorption peaks at 526 nm and 546 nm as shown in fig 4.11.

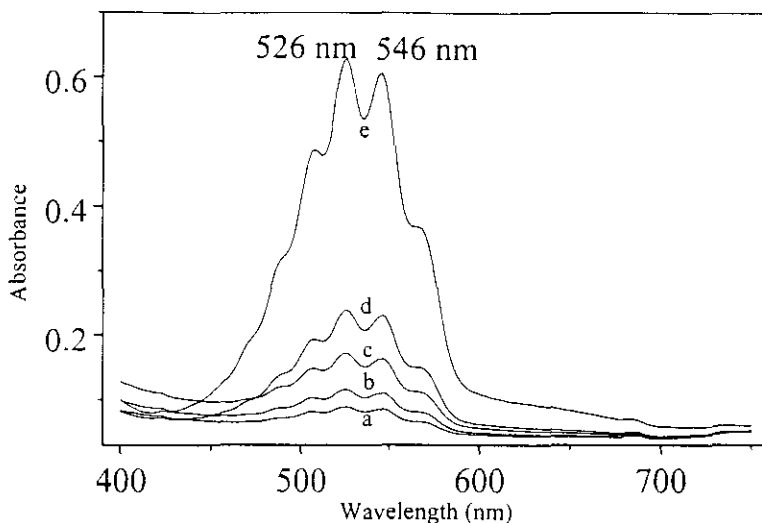


Figure 4.11: Absorption spectrum of the resulting solution containing various concentrations of Mn^{2+} ($a = 3$ ppm, $b = 5$ ppm, $c = 7$ ppm, $d = 10$ ppm and $e = 30$ ppm)

The schematic diagram of the experimental set-up used to characterize the iron sensor is shown in fig 4.12. The laser radiation at 488 nm from an Ar^+ laser (Spectra Physics, model 171) is coupled to the optical fiber using two mirrors M_1 and M_2 and a microscope objective having a numerical aperture 0.25. The optical fiber is fixed on a pair of x-y translators, with the unclad/microbent portion of the fiber passing through a glass cell. A laser power meter (Metrologic 545-45) is used to measure the light guided through the fiber, which in turn is connected to a PC using the GPIB (IEEE-488) card of a digital multimeter (DMM, HP-34410). Another laser power meter (Newport 1815-C) is used with the microbent fiber to measure the optical power in the cladding modes. Fig 4.13 shows the program used to continuously take the values from the DMM, which is plotted to give the graph. The front panel of the basic LabVIEW program of the DMM is shown in the fig 4.14 and its block diagram is shown in fig 4.15. It may be noted that the front panel is almost similar to the front view of the DMM. The total number of samples and the delay between each sample can be adjusted. The data is taken as a block of samples which also can be controlled.

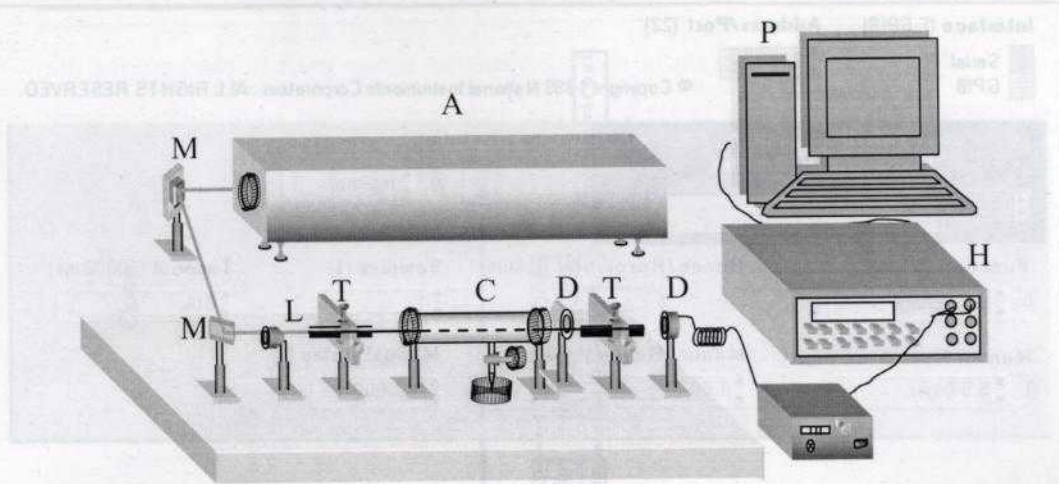


Fig 4.12: Schematic of the experimental set-up for Iron sensing. A- Ar^+ laser, M_1 -Mirror1, M_2 -Mirror2, L-Lens, T_1 -X-Y translator, T_2 -X-Y translator, C-Glass Cell, D_1 -Detector1 (Metrologic 45-545), D_2 -Detector2 (Newport 1815-C), H-Multimeter & P - Personal Computer

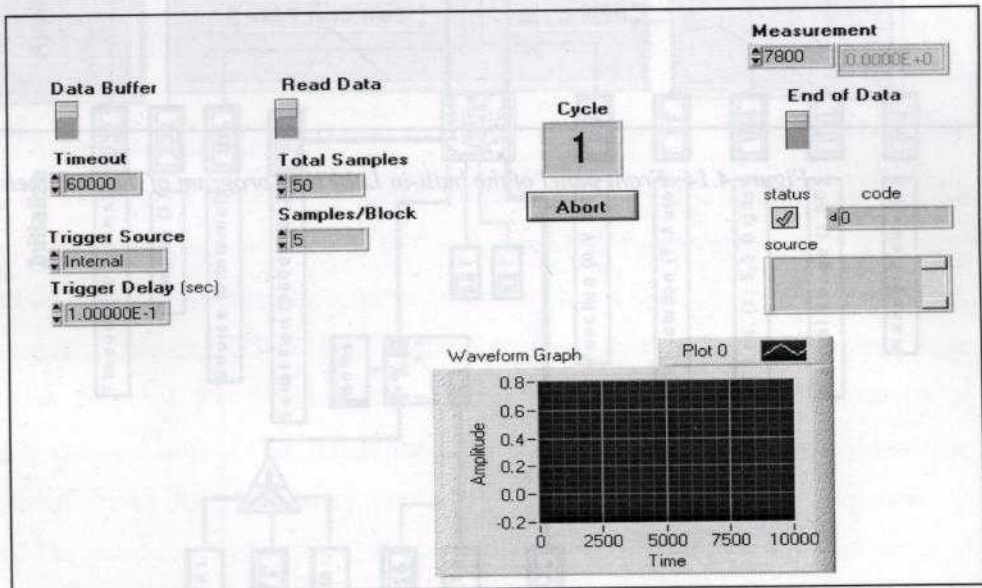


Figure 4.13: Front panel of the LabVIEW program used to continuously take readings

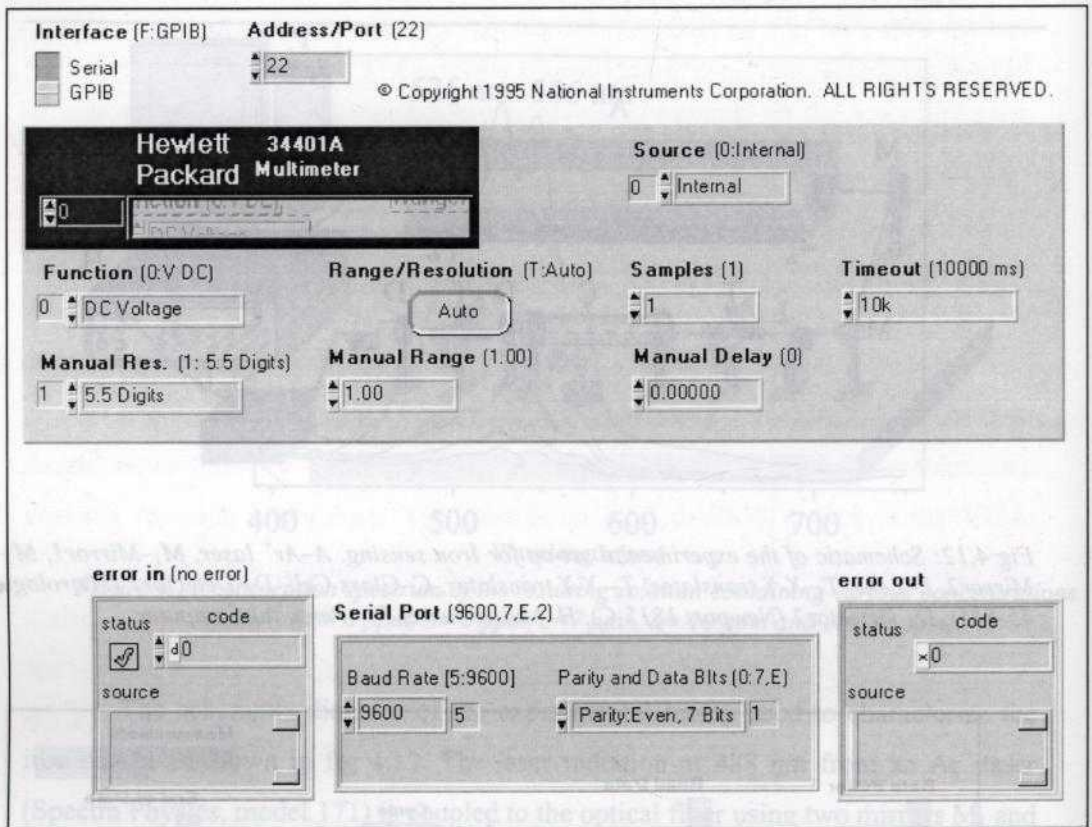


Figure 4.14: Front panel of the built-in LabVIEW program of the multimeter

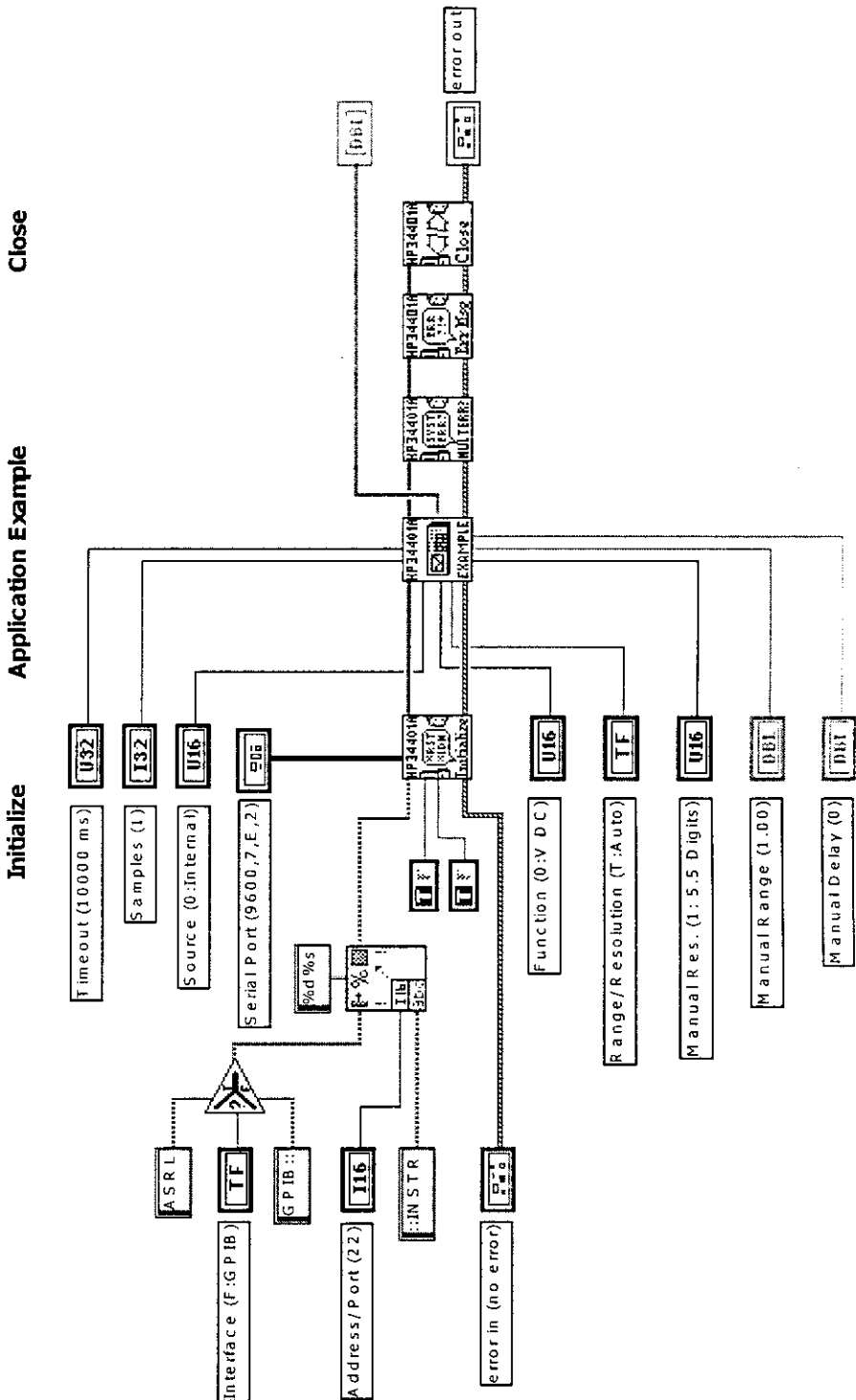


Figure 4.15: front panel of the LabVIEW program used to continuously take readings

The schematic diagram of the experimental set-up used to characterize the manganese sensor is shown in fig 4.16. The light coming from a green He-Ne laser (JDS Uniphase) operating at 543.5 is coupled to the unclad or microbent fiber whose sensing region is in a cell containing Mn^{2+} solution. A detector (Newport 1815-C) measures the light intensity coming at the output end of the fiber.

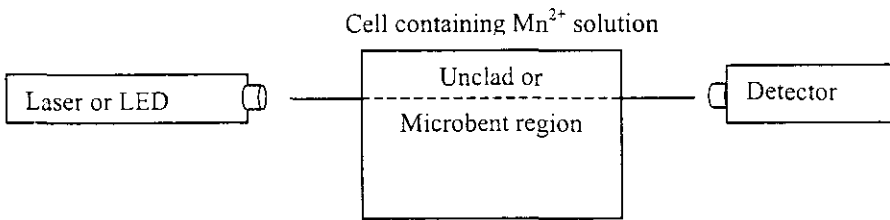


Figure 4.16: Schematic sketch of the experimental setup for Mn^{2+} sensing

In order to make the sensor cost effective, laser is replaced with a green super bright LED whose modulating circuit is shown in the fig 4.17. The value of the variable resistance $200\text{ K}\Omega$ determines the output frequency of the astable multivibrator, which is adjusted to oscillate at one KHz. The output of the multivibrator is given to the LED for its modulation.

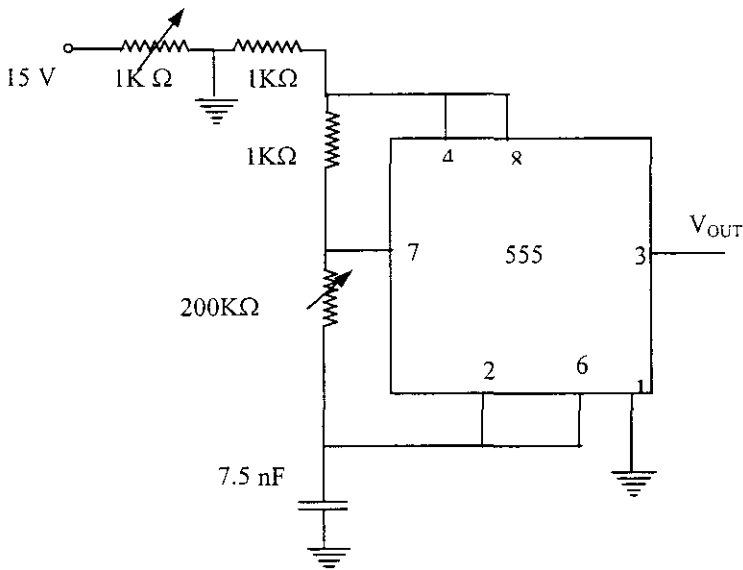


Figure 4.17: Diagram of the LED modulation circuit

The expensive commercial detector is replaced with an inexpensive photodiode and an amplifying circuit which is shown in fig 4.18.

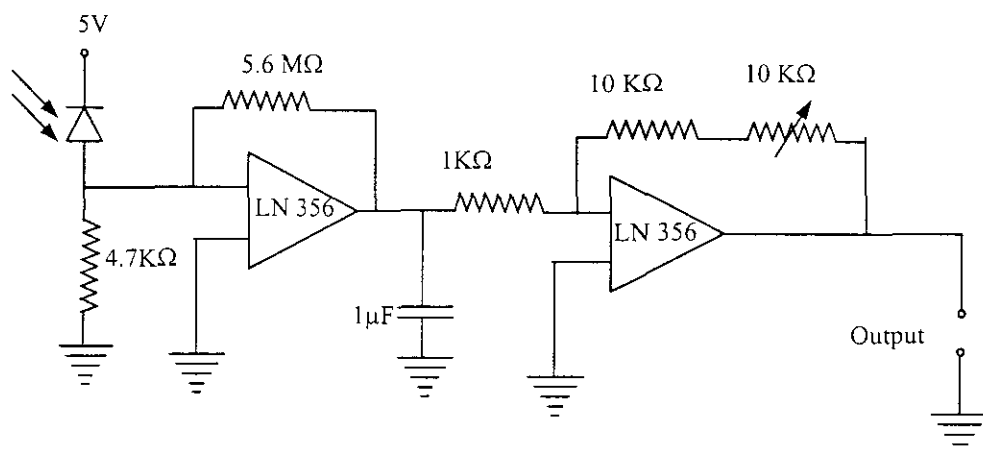


Figure 4.18: Diagram of the photodetector circuit

The amplifying circuit consists of two stages using low noise FET OPAMPs (LN 356); the first stage is a current to voltage converter and the second stage is a voltage amplifier.

4.2.3 Results and Discussion

Fig. 4.17 shows the variation of output power from a 12 cm unclad multimode PCS fiber for various concentrations of Fe^{3+} surrounding the unclad portion. It is evident from the plot that the present device can measure even a few ppb of Fe^{3+} . In addition, the sensor responds in a logarithmic fashion, which makes the device to cover a large dynamic range of 4 – 5 orders of magnitude, though sacrificing its sensitivity at higher concentrations. This is not the case with conventional spectrophotometric detection where the absorbance varies linearly with concentration. Moreover, it should be noted that with a standard spectrophotometer (Jasco UV-570) the range of detection is limited with a minimum detectable concentration of 1 ppm and the maximum 25 ppm. However, according to the drinking water standards of the World Health Organization and Kerala State Pollution Control Board the permissible limit of

iron content in water is 0.3 ppm which is well below the detection limit of the spectrophotometric method.

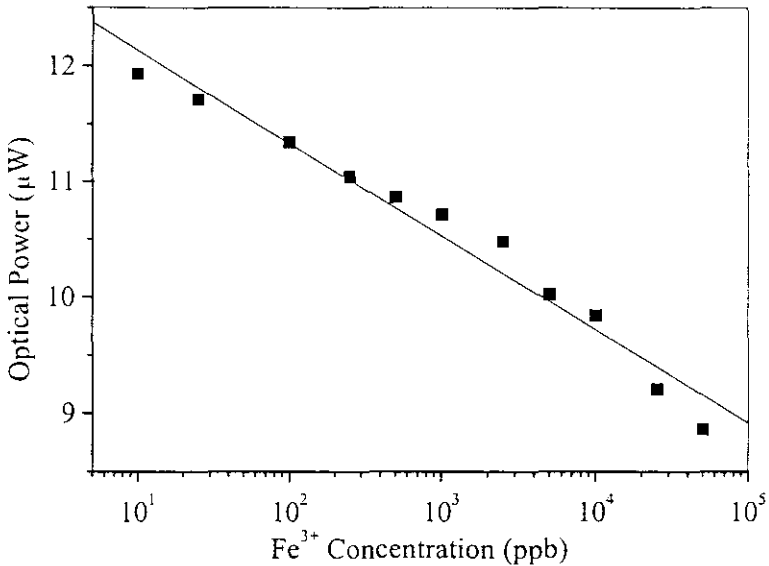


Figure 4.19: Variation of guided mode power in an unclad multimode plastic clad silica fiber with respect to Fe^{3+} concentration

Figs 4.20 and 4.21 shows the experimental graphs obtained with a plastic FOS whose sensing region is 6 cm long microbent portion at the middle of the fiber. Fig 4.18 corresponds to the change in core mode (guided mode) power with the variation in concentration of Fe^{3+} surrounding the bent portion of a plastic fiber. It is observed that the sensitivity of a 6 cm microbent fiber is almost same as that of a 12 cm unclad PCS fiber. This reduction in the sensing length is obviously an advantage of the former over the unclad fiber sensor.

Fig 4.21 represents the change in cladding mode power with the change in concentration of Fe^{3+} surrounding the bent portion of the fiber. Contrary to the curve obtained for guided modes, here the graph in this case is not linear throughout the range of measurements. This is similar to our earlier observation with the generic sensor using microbent fiber. The non-linearity is mainly attributed to the azimuthal anisotropy in microbending that in turn is restricted to a single plane only. But it

should be noted that this detection of cladding modes is very sensitive above 1-ppm level of Fe^{3+} concentration.

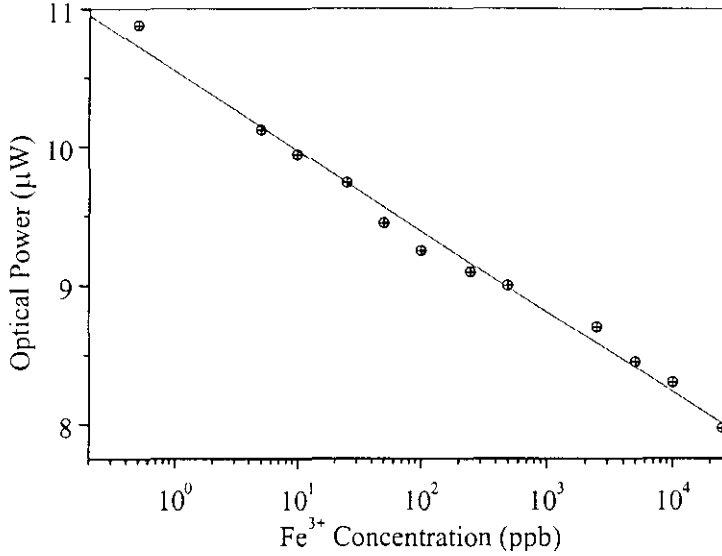


Figure 4.20: Variation of guided mode power in a microbent plastic fiber with respect to Fe^{3+} concentration

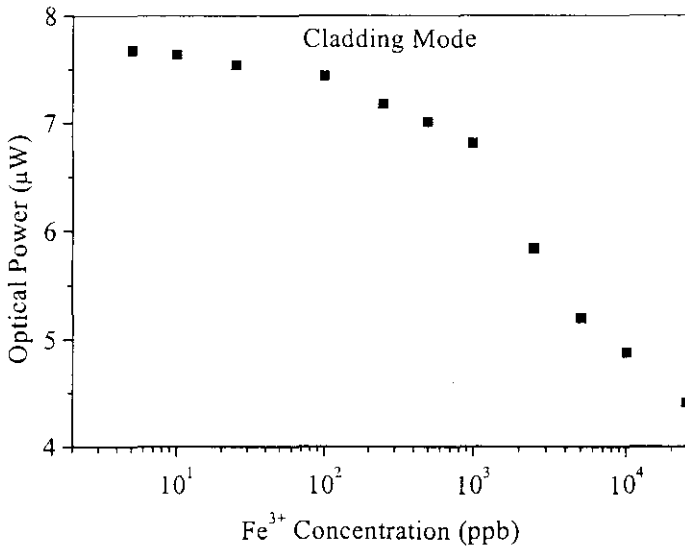


Figure 4.21: Variation of cladding mode power in a microbent plastic fiber with respect to Fe^{3+} concentration

Comparing the results obtained with the unclad PCS fiber sensor and microbent plastic fiber sensor, the latter is found to be more useful, because of the following reasons. 1) The sensing length can be reduced considerably without any loss of sensitivity, 2) it is a double detection scheme utilizing both cladding and core modes which enables a cross checking of the readings and hence the reliability of measurements is high, 3) the sensitivity of detection of cladding mode variation in ppm range is higher than the core mode power variation corresponding to both microbent and unclad fibers and 4) it uses inexpensive plastic fiber and hence is cost effective. It can be seen that both type of sensors are of the intensity modulated type and hence requires only a few optical components which will significantly reduce their cost, from the device point of view.

The response time of the present device is measured by taking the readings continuously in the block data collection mode of LabVIEW as shown in fig 22. The valleys in the graph correspond to the removal of standard solutions from the glass vessel. The response time is found to be approximately 2 minutes which is the time needed for the reading to get stabilized. Nevertheless, during our measurements we have observed that 90% of the stabilized power meter reading is reached within a relatively short time of 3 seconds.

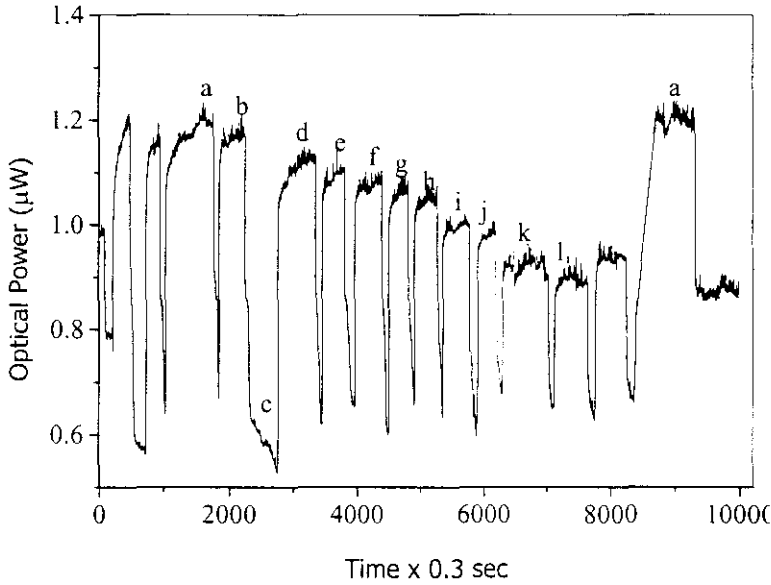


Figure 4.22: Temporal response of the PCS fiber Fe^{3+} sensor (a=water, b= 2.5 ppb, c= air, d=10 ppb, e=25 ppb, f= 100 ppb, g= 250 ppb, h=1ppm, i=2.5 ppm, j=10 ppm, k=25 ppm, l=50 ppm)

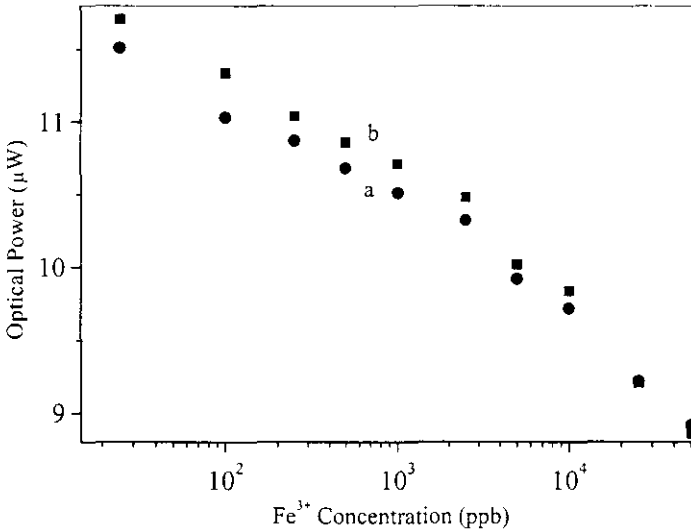


Figure 4.23: Variation of guided mode power in an unclad multimode plastic clad silica fiber with respect to Fe^{3+} concentration (a=response time of 3 seconds, b=response time of 2 minutes)

Fig 4.23 gives a comparison between the readings taken after two minutes/three seconds of addition of the various Fe^{3+} test solutions. It can be clearly seen that the response time can be considerably reduced without much sacrificing the sensitivity. Fig 4.24 & 4.25 shows the characteristic curves of the Mn^{2+} sensor with a microbent fiber and an unclad fiber respectively; the source is a laser, and the detector is a power meter (Metrologic).

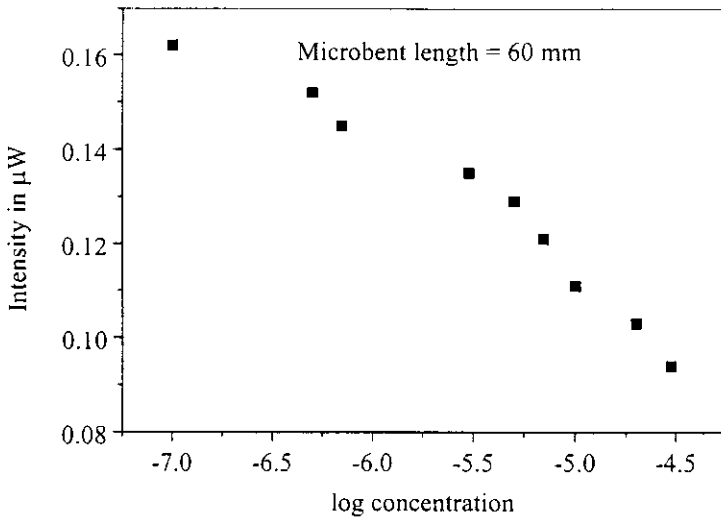


Figure 4.24: Variation of guided mode power in a microbent plastic fiber with respect to Mn^{2+} concentration

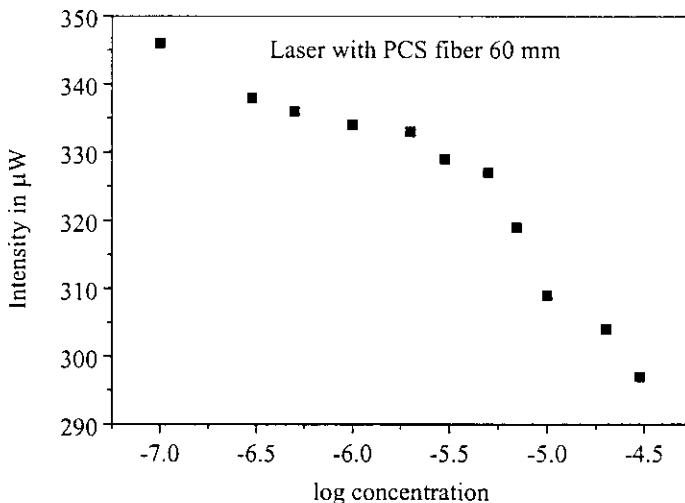


Figure 4.25: Variation of guided mode power in an unclad multimode plastic clad silica fiber with respect to Mn^{2+} concentration

Fig 4.26 shows the characteristic curve of the sensor with an unclad fiber as the sensor head, the source is an LED, and the detector is a photodiode. Comparison of the above three figs shows that the sensor with LED and the inexpensive detector circuit is as sensitive as that obtained with the laser and expensive detector.

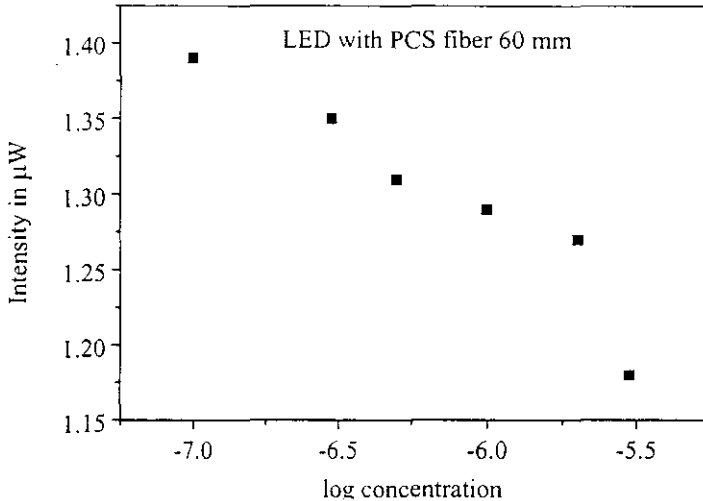


Figure 4.264: Variation of guided mode power in an unclad multimode plastic clad silica fiber with respect to Mn^{2+} concentration

4.3. Referencing strategies for intensity modulated fiber optic sensors (IMFOS)

Considerable amount of research has been carried out for the fabrication of myriad varieties of FOS. However, only a few of them have come to the market. One reason for this may be the restricted precision of IMFOS which are the most economic ones. In continuous analogue measurement applications of IM-FOS there is the requirement that the output from a system should be truly related to the measurand alone. In practice, this condition cannot be easily satisfied due to the variable losses within optical components such as fiber leads, optical couplers and connectors. Furthermore, additional measurement unreliability can arise from the instability of the optoelectronic components, such as optical sources and detectors. It is impossible to eliminate these variations in any optical fiber systems design but compensation may be applied by monitoring the undesirable optical signal losses. The usual approach is

to generate at least one additional (reference) signal which may then, in conjunction with the measurand signal, be used to make a relative measurement that is free from these so-called common mode variation. Both signals need be separately identified which is normally achieved by employing either spatial separation, wavelength separation, frequency separation, temporal separation or a combination of these methods [69-76].

Spatial separation is required when the optical signals have the same spectral constitution as in the case where they are generated from a single LED source used in conjunction with a Y-coupler or from two similar LED sources. In the case when each signals contained within a separate spectral band both signals can be transmitted on the same optical fiber link. The presence of spectral spacing between the signal channels enables wavelength separation by the use of simple wavelength demultiplexing elements. Temporal separation can be employed when the signals are generated from, separate optical sources by time division multiplexing (TDM). The optical signals are transmitted with separate time slots and therefore they can be separately identified from their time of arrival at the point of detection. In the frequency separation technique by frequency division multiplexing (FDM) the optical source is modulated at different frequencies. The optical signals are then separated by the use of electrical filtering of the photocurrent into the respective frequency components. An advantage of both TDM and FDM signals is that they can be allowed to propagate into the same fiber as well as enabling detection with common photodetector.

Here we propose and develop a new reference strategy that can take care of source fluctuations, by placing an index matching liquid on the cladding at a distance of 1.5 cm from the input side of the optical fiber and detecting this optical power which is used to normalize the fiber output. Light is launched into the optical fiber as both core and cladding modes and the power carried in the latter decays off very quickly. When there is source intensity variation, corresponding changes occur for core and cladding mode power. In the conventionally used IMFOS, the core mode

power at the fiber output end alone is measured and used for sensing applications. However, here we detect both core mode and cladding mode power and the former is normalized by the latter. The schematic of the experimental set-up is shown in Fig 4.27. The source used is a Ar^+ laser operating in the current control mode so that its output power can be varied.

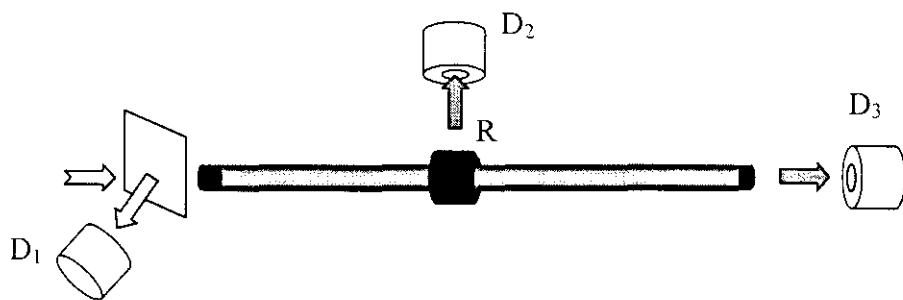


Fig 4.27: D_1 , detector for measuring source power, D_2 , detector for measuring cladding mode power, D_3 , for measuring core mode power, R , index matching liquid

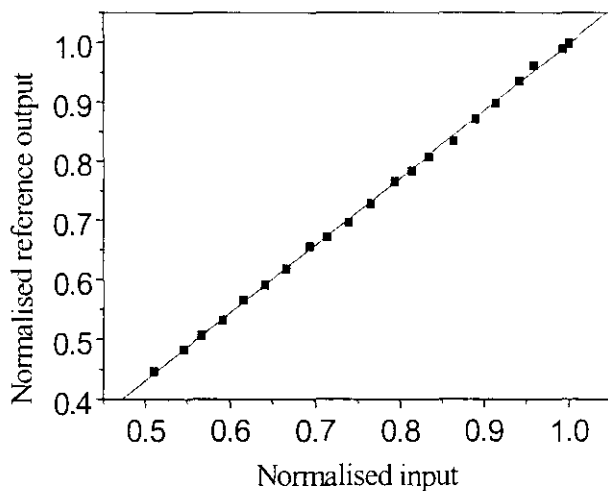


Figure 4.28: Variation of cladding mode power with respect to source power

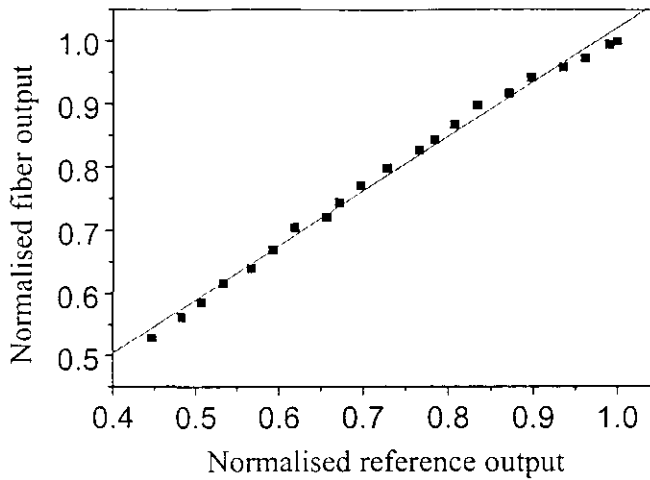


Figure 4.29: Variation of cladding mode power with respect to source power

The variation of the cladding mode power with respect to source power and core mode power are shown in fig 28 and fig 29 respectively. From the graphs, it is clear that the present referencing scheme can be used in various IMFOS for nullifying the effect of source fluctuations.

As first part of this chapter, development of sensors for weight and displacement measurement based on interferometry has been discussed. In the second part, fabrication of intensity modulated sensors for Fe^{3+} and Mn^{2+} detection in aqueous environments has been detailed. The sensors are evaluated in terms of the findings of the experimental results. Finally a new referencing strategy has been developed.

References:

1. Otto S Wolfbeis, *Anal. Chem.* **74**, 2663 (2002)
2. Ferdinand P, Magne S, Roy O, Marty V, Dewynter, Rougeault S, Bugaud M, in *Optical Sensors and Microsystems*, Kluwer Academic/Plenum Publishers, New York, 205 (2000)
3. Martellucci S, Chester A N, Mignani A. G, *Chem. Abstr.* **134**, 154059 (2001)
4. Tokar J. M, Dickey T D, *Ocean Sci. Technol.* **1**, 303 (2000)
5. Lyons W B, Ewald H, Flanagan C, Lochmann S, Lewis E, *Meas. Sci. Technol.* **12**, 958 (2001)
6. Burck J, Kramer K, Roth S, *Technol. Ueberwach.* **41**, 18, (2000)
7. Zaatar Y, Zaouk D, Bechara J, Houry A, Llinaress C, Charles J P Mater. Sci. Eng. B, **B74**, 296; (2000)
8. Hecht H, Koelling M, *Sens. Act. B*, **B81**, 76 (2001)
9. Zhuang Z, Li W, Chen X, Sun D, Wang X, *Xiamen Daxue Xuebao, Ziran Kexueban*, **40**, 477, (2001)
10. Li M, Zhang M, *Chuangang Jishu Xuebao*, **13**, 74 (2000)
11. Degrandpre M D, Baehr M M, Hammar T R, *Ocean Sci. Technol.* **1**, 123 (2000)
12. Neurauter G, Klimant I, Wolfbeis O S, *Fresenius' J. Anal.Chem.* **366**, 481 (2000)
13. G Showtzer, I Latka, H Lehmann and R Wilsch, *Sens. Act. B*, **38-39**, 151 (1997)
14. W R Seitz, in *CRC Critical Reviews in Analytical Chemistry*, **19**, 135 (1988)
15. S M Klainer, J R Thomas and J C Francis, *Sens. Act. B*, **11**, 81 (1993)
16. R P Gupta, Z Gergintschew, D Schipanski, P D Vyas, *Sens. Act. B*, **63**, 35 (2000)
17. O S Wolfbeis and H E Posch, *Anal. Chim. Acta*, **185**, 321 (1986)
18. J Burck, J P Conzen, B Beckhaus and H J Ache, *Sens. Act. B*, **18-19**, 291 (1994)
19. K M Leonard, *Sens. Act. B*, **24-25**, 458 (1995)
20. A S Jazi and J V Peterson, **CH2998**, 1139 (1991)
21. D W Swindle Jr, T Vo-Dinh and M G Yalcintas, in *Environmental Geotechnology*, Balkema Rotterdam (1992)
22. P Radhakrishnan, V P N Nampoori and C P G Vallabhan, *Opt. Engg.* **32**, 62 (1993)
23. Boris Mizaikoff, *Meas. Sci. Technol.* **10**, 1185 (1999)
24. P Suresh Kumar, C P G Vallabhan, V P N Nampoori, V N Sivasankara Pillai and P Radhakrishnan, *J. Opt. A: Pure Appl. Opt.* (in press)
25. T Hirschfeld, T Denton, F Milanovich, S Klainer, *Opt. Engg.* **22**, 527 (1983)
26. J H Cole, R L Johnson, P B Bhutia, *J. Acoust. Soc. Am.* **62**, 1136 (1977)
27. C D Butter and G B Hocker, *Appl. Opt.* **17**, 2867 (1978)
28. G B Hocker, *Appl. Opt.* **18**, 1445 (1979)
29. H Okamura, *Elec. Lett.* **23**, 834 (1987)
30. J H Cole, J A Bucaro, *J. Acoust. Soc. Am.* **62**, 2108 (1980)
31. R A Bergh, H C Lefere and J H Shaw, *J. Lightwave Technol.* **2**, 91 (1984)
32. B Culshaw and I P Giles, *J. Phys. E: Sci. Instrum.* **16**, 5 (1983)
33. A Dandriudge, A B Tveten, TG Giallorenzi, *Appl. Phys. Lett.* **37**, 526 (1980)
34. D A Jackson, *J. Phys. E: Sci. Instrum.* **14**, 1274 (1981)
35. K M Leonard, Development of a fiber-optic chemical sensor for multicontaminant monitoring of environmental systems, *Sens. Actuators B*, **24-25**, 450 (1995)
36. L Yuan and L Zhou, *Meas. Sci. Technol.* **9**, 1174 (1998)
37. M A Page-Jones, J K A Everard, *Elec. Lett.* **26**, 117 (1990)
38. F M Haran, J S Barton, S R Kidd and J D C Jones, *Meas. Sci. Technol.* **5**, 526 (1994)

39. K De Souza, P C Wait and T P Newson, *Elec. Lett.* **33**, 2148 (1997)
40. D A Jackson, *Meas. Sci. Technol.* **5**, 621 (1994)
41. D A Brown and SL Garrett, *Proc. SPIE*, **1367**, 282 (1990)
42. F Bucholtz, D M Dagenais, K P Koo and S Vohra, *Proc. SPIE*, **1367**, 226 (1990)
43. C McGarrity, D A Jackson, *Proc. SPIE*, **1797**, 218 (1992)
44. D Zarinetchi, S P Smith and S Ezckiel, *Opt. Lett.* **16**, 229 (1991)
45. F Farahi, J D C Jones and D A Jackson, *Opt. Lett.* **16**, 1800 (1991)
46. F Farahi, D J Webb, J D C Jones and D A Jackson, *J. Lightwave Technol.* **8**, 137 (1990)
47. A S Georges, T P Newson, J D C Jones and D A Jackson, *Opt. Lett.* **14** 251 (1989)
48. M N Inci, S R Kidd, J S Barton and J D C Jones, *Meas. Sci. Technol.* **4**, 382 (1993)
49. D A Jackson and J D C Jones, *Opt. Laser Technol.* **18**, 243, 299 (1986)
50. A D Kersey, A Dandridge, *Proc. SPIE*, **838**, 184 (1987)
51. J A Sirkis and H W Haslach Jr. *J. Lightwave Technol.* **8**, 1497 (1990)
52. A B Buckman, *J. Lightwave Technol.* **8**, 1456 (1990)
53. K D Oh, J Ranade, V Arya, A Wang, R O Claus, *IEEE Photonics. Technol. Lett.* **9**, 797 (1997)
54. J T Mercado, A V Khomenko, R C Martinez and M A Garcia-Zarate, *Opt. Comm.* **177**, 219 (2000)
55. J W Barbara, J P Davis, L C Bobb, H D Krumboltz and D C Larson, *J. Lightwave Technol.* **LT-5**, 1169 (1987)
56. Han-Sun Choi, Henry F. Taylor and Chung E. Lee, *Opt. Lett* **22**, 1814 (1997)
57. Howard S Peavy, Donald R Rowe, George Tchobalogous, *Environmental Engineering*, Mc Graw Hill, 1985
58. Kerala State Pollution Control Board – STANDARDS & GUIDELINES.
59. B P Esposito, W Breuer and Z I Cabantchik, *Biometals 2002: Third International Biometals Symposium*, 729 (2002)
60. Olynyk J, Hall P, Sallie R, Reed W, Shilkin K and Mackinnon M, *Hepatology*, **12**, 26 (1990)
61. Lee C, *Journal of Forensic Sciences*, **31**, 920 (1986)
62. J M Barrero, M C Moreno-Bondi, M C Perez-Conde and C Camara, *Talanta*, **40**, 1619 (1993)
63. J M Barrero, C Camara and M C Perez-Conde, *Analyst*, **120**, 431 (1995)
64. N Malcik and P Caglar, *Sens. Act. B*, **38-39**, 386 (1997)
65. P Pulido, J M Barrero, M C Perez-Conde and C Camara, *Quim. Anal.* **12**, 45 (1993)
66. M Feraldos, M C Moreno and C Camara, *Analisis*, **16**, 87 (1988)
67. L Jianzhong and Z Zhujun, *Anal. Lett.* **27**, 2431 (1994)
68. Vogel's textbook of Quantitative inorganic analysis, Longman Group Limited, London. Part F, Chapter 18 "Determination of Iron" 738 (1978)
69. B E Jones and R C Spooncer, *J. Phys. E: Sci. Instrum.* **16**, 1124 (1983)
70. G Murtaza and J M Senior, *Opt. Laser Technol.* **25**, 235 (1993)
71. E Theocharous, *Proc. SPIE*, **798**, 253 (1987)
72. G Martens, J Kordts and G Weidinger, *Proc. SPIE*, **798**, 186 (1987)
73. M Kieli and P R Herezfeld, *Proc. SPIE*, **798**, 331 (1987)
74. P M Cavaleiro, A B Lobo Ribeiro and J L Santos, *Elec. Lett.* **31**, 392 (1995)
75. E Theocharous, *J. Phys. E: Sci. Instrum.* **18**, 253 (1983)
76. I P Giles, S McNeill and B Culshaw, *J. Phys. E: Sci. Instrum.* **18**, 502 (1983)

Long Period Gratings in Multimode Fibers: Application in Chemical Sensing

Introduction

Two major areas of application of optical fibers are fiber optic communication and sensing. The bridge between these two fields has become shorter by the advent of fiber gratings, both short period and long period, which are extensively used for communication as well as sensing purposes. Gratings, both amplitude and phase, are optical components which diffract a beam of light. Grating structures in optical fibers was first fabricated by Hill and co-workers in 1978 [1]. They launched an intense Ar⁺ laser radiation into a germanium doped fiber and observed that after several minutes an increase in the back-reflected light intensity occurred which grew until almost all the light was reflected back. Spectral measurements, done indirectly by strain and temperature tuning of the fiber grating, confirmed that a very narrowband Bragg grating filter had been formed over the entire 1-m length of the fiber. This achievement subsequently called "Hill gratings" was an outgrowth of research on the nonlinear properties of germanium-doped silica fiber. Detailed studies showed that the grating strength increased as the square of the light intensity, suggesting a two-photon process as the mechanism [2]. In the original experiments, laser radiation at 488 nm was reflected from the fiber end producing a standing wave pattern that

formed the grating. The problems encountered by Hill gratings such as the fixed and narrow operating range was removed by the discovery of external writing or side writing technique by Meltz et al in 1989 [3] where a single photon at one-half of the above wavelength, namely at 244 nm in the ultra violet (UV), was used and it proved to be far more effective. Moreover, the grating formation was found to be orders-of-magnitude more efficient.

Fiber Gratings in general are classified according to the grating period into fiber bragg grating (FBG) with grating period of about $1\mu\text{m}$ and long period grating (LPG) having a grating period of about $100\mu\text{m}$. In FBG the diffracted light travels contra-directionally to the light launched and in an LPG the diffracted light is co-directional with the launched light as shown in fig 5.1. FBGs find applications as laser diode stabilizers [4], mode converters [5], fiber amplifiers, fiber lasers [6], band pass filters [7], add-drop filters [8,9], dispersion compensators [10], optical sensors [11-20] etc., whereas LPGs are generally used as non-reflecting band-rejection filters [21,22], band-pass filters, gain flatteners in erbium doped fiber amplifiers (EDFAs), optical sensors [23-30] etc. Both FBG and LPG based optical sensors are superior to other fiber sensors in that they are self referencing in nature.

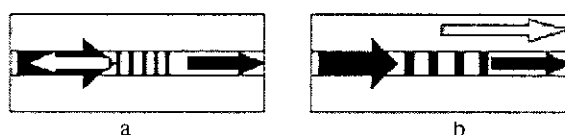


Fig 5.1: Light propagation in an FBG (a) and an LPG (b)

5.1 Photosensitivity of glass

When an optical fiber is irradiated by ultraviolet (UV) light, the refractive index of the fiber changes permanently; a phenomena termed as photosensitivity [31-35]. The change in refractive index is permanent in the sense that it will last for decades (life times of 25 years are predicted) if the optical waveguide after exposure is annealed appropriately, that is by heating for a few hours at a temperature of 50°C above its maximum operating temperature. Initially, photosensitivity was thought to be a

phenomenon associated only with germanium doped optical fibers. Subsequently, it has been observed in a wide variety of different fibers, many of which did not contain germanium as a dopant. Nevertheless, optical fiber having a germanium-doped core remains the most important material for the fabrication of grating based devices.

The magnitude of the refractive index change (Δn) obtained depends on several factors such as the irradiation conditions (wavelength, intensity and total dosage of irradiating light), the composition of glassy material forming the fiber core and any processing of the fiber prior to irradiation. A myriad different continuous-wave and pulsed laser light sources with wavelengths ranging from the visible to the ultraviolet have been used to make photo-induce refractive index changes in optical fibers. In practice, the most commonly used light sources are KrF and ArF excimer lasers that generate, respectively, 248 and 193 nm optical pulses (pulsewidth 10 ns) at pulse repetition rates of 50–75 pulses/s. The typical irradiation condition is an exposure to the laser light for a few minutes at intensities ranging for 100–1000 mJ/cm². Under these conditions, refractive index variation is positive in germanium doped monomode fiber with a magnitude ranging from 10^{-5} to 10^{-3} .

The refractive index change can be enhanced (photosensitization) by processing the fiber prior to irradiation using techniques such as hydrogen loading or flame brushing. In the case of hydrogen loading, a piece of fiber is put in a high-pressure vessel containing hydrogen gas at room temperature and pressures of 100 to 1000 atmospheres. After a few days, hydrogen in molecular form diffuses into the silica fiber and at equilibrium, the fiber becomes saturated (i.e. loaded) with hydrogen gas. The fiber is then taken out of the high-pressure vessel and irradiated before the hydrogen gets sufficient time to diffuse out. Photoinduced refractive index changes up to 100 times greater (Δn as high as 10^{-2}) are obtained by hydrogen loading a germanium-doped-core optical fiber. In flame brushing, the section of fiber that is to be irradiated is mounted on a jig and a hydrogen-fueled flame is passed back and forth along the length of the fiber. The brushing takes about 10 minutes and upon

irradiation, an increase in the photoinduced refractive index change by about a factor of 10 is obtained.

Irradiation at intensity levels higher than 1000 mJ/cm^2 mark the onset of a different nonlinear photosensitive process that enables a single irradiating excimer light pulse to photoinduce a large index change in a small localized region near the core/cladding boundary. In this case, the refractive index changes are sufficiently large to be observable with a phase contrast microscope and have the appearance of damaging the fiber physically. This phenomenon has been used for the writing of gratings using a single excimer light pulse. No well developed theory exists for the physical mechanism underlying the photosensitivity in optical fibers. Nevertheless, densification model and color center model are the two models used to explain the photosensitivity. While the former gives adequate explanation for photosensitivity in ordinary germanosilicate glasses, the latter is found to be useful in describing the enhancement of photosensitivity for H_2 loaded germanosilicate fibers.

5.2 Grating Fabrication Techniques

The following tree diagram shows the different types of grating fabrication techniques.

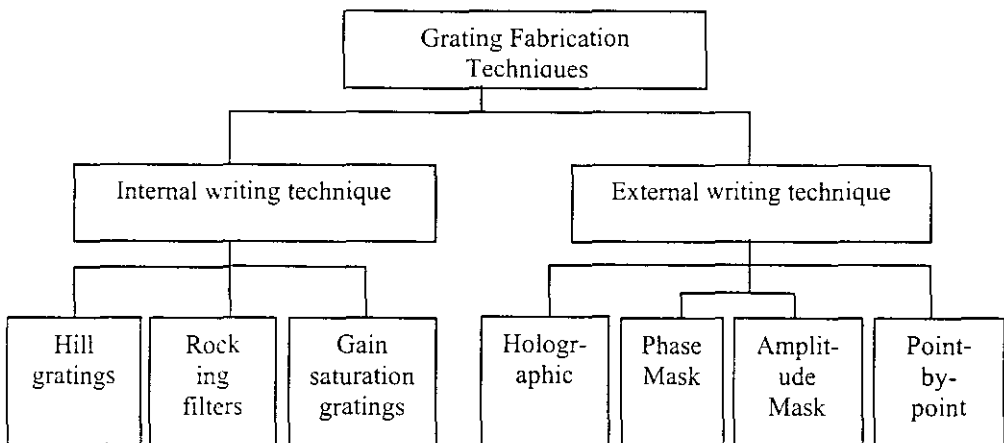


Figure 5.2: Tree diagram showing the types of grating fabrication techniques

Fiber gratings can be fabricated by a variety of techniques. In the internal writing technique, which includes the Hill gratings, Rocking filters and Gain Saturation gratings, the gratings are formed by two-photon absorption resulting from interference of two counter propagating beams in an optical fiber, which results in a self-organized refractive index. The more versatile and widely used external writing techniques such as interferometric, phase masks, amplitude masks and point-by-point technique, employ external UV writing procedure by single-photon absorption.

5.2.1 Holographic technique

In the Holographic (interferometric) technique UV light from a laser is split into two and allowed to interfere to form a standing wave pattern of periodic spatial light intensity that writes a corresponding periodic index grating in the core of the fiber [36,37]. This method known as the transverse holographic technique is possible because the fiber cladding is transparent to the UV light whereas the fiber core is highly absorbing.

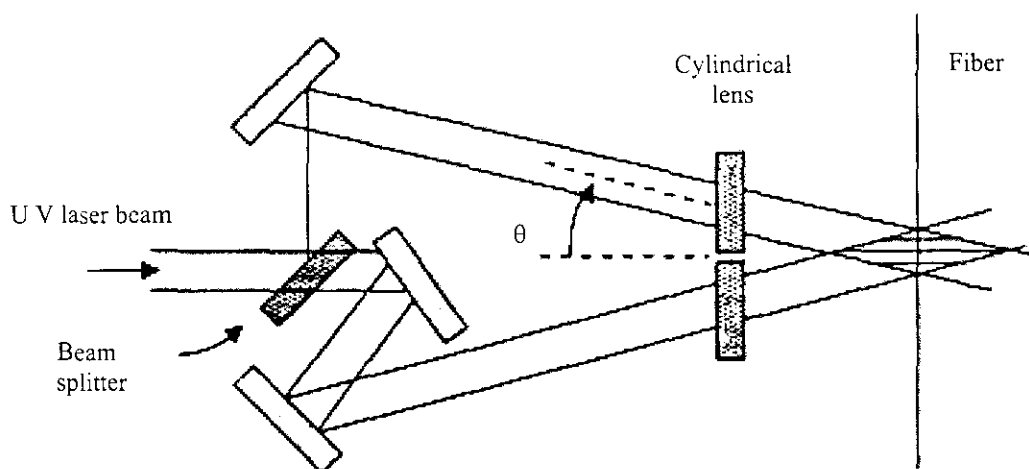


Figure 5.3: Schematic illustration of the dual-beam holographic technique

5.2.2 Phase Mask Technique

In the phase mask technique, ultraviolet light, which is incident normal to a phase mask, is diffracted by its periodic corrugations [38,39]. The phase mask is made from

flat slab of silica glass, which is transparent to ultraviolet light. On one of the flat surfaces, a one dimensional periodic surface relief structure is etched using photolithographic techniques. The shape of the periodic pattern approximates a square wave in profile. The optical fiber is placed almost in contact with the corrugations of the phase mask as shown in fig 5.4.

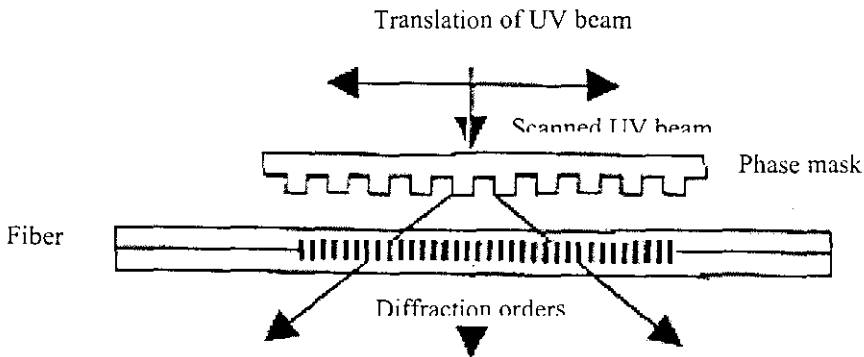


Figure 5.4: Schematic illustration of a phase mask interferometer used for making fiber gratings

If the period of the phase mask grating is Λ_{mask} , the period of the photo-imprinted index grating is $\Lambda_{\text{mask}}/2$. Note that this period is independent of the wavelength of ultraviolet light irradiating the phase mask; however, the corrugation depth required to obtain reduced zeroth-order light is a function of the wavelength and the optical dispersion of the silica. The phase mask technique has the advantage of greatly simplifying the manufacturing process for Bragg gratings, yet yielding gratings with a high performance. In comparison with the holographic technique, the phase mask technique offers easier alignment of the fiber for photo-imprinting, reduced stability requirements on the photo-imprinting apparatus and lower coherence requirements on the ultraviolet laser beam thereby permitting the use a cheaper ultraviolet excimer laser source. Furthermore, there is the possibility of manufacturing several gratings at once in a single exposure by irradiating parallel fibers through the phase mask. The capability to manufacture high-performance gratings at a low per unit grating cost is critical for the economic viability of using

gratings in some applications. A drawback of the phase mask technique is that a separate phase mask is required for each Bragg wavelength. The phase mask technique not only yields high performance devices but also is very flexible in that it can be used to fabricate gratings with controlled spectral response characteristics. The phase mask technique has also been extended to the fabrication of chirped or aperiodic fiber gratings.

5.2.3 Amplitude mask technique

A simple, yet efficient way of fabricating LPGs is the amplitude mask technique where an amplitude mask with variable transmittance is used to modulate the UV light falling on the optical fiber. The variations in the mask include using photolithographic chrome-on-silica mask [21,22], etched dielectric mirrors [40], or microcontact [41] printing of the masks onto the fiber surface.

5.2.4 Point-by-point technique

This non-holographic scanning technique bypasses the need of a master phase mask and fabricates the grating directly on the fiber, period by period, by exposing short sections of the fiber to a single high-energy pulse. The fiber is translated by a distance before the next pulse arrives, resulting in a periodic index pattern such that only a fraction in each period has a higher refractive index [42,43]. The method is referred to as point-by-point fabrication. The technique works by focusing an ultraviolet laser beam so tightly that only a short section is exposed to it. Typically, the width of the beam is chosen to be half of the period, although it could be a different fraction if so desired.

There are a few practical limitations of this technique. First, only short fiber gratings (< 1 cm) are typically produced because of the time-consuming nature of the point-by-point fabrication method. Second, it is hard to control the movement of a translation stage accurately enough to make this scheme practical for long gratings. Third, it is not easy to focus the laser beam to a small spot size that is only a fraction of the grating period. Typically, the period of a first-order grating is about $0.5 \mu\text{m}$ at $1.55 \mu\text{m}$ and becomes even smaller at shorter wavelengths. For this reason, the

technique was first demonstrated in 1993 by making a 360- μm -long, third order grating with a period of 1.59 μm . The third-order grating still reflected about 70% of the incident 1.55- μm light. From a fundamental standpoint, an optical beam can be focused to a spot size as small as the wavelength. Thus, the 248-nm laser commonly used in grating fabrication should be able to provide a first-order grating in the wavelength range from 1.3 to 1.6 μm with proper focusing optics similar to that used for fabrication of integrated circuits. Nevertheless, the point-by-point fabrication method is quite suitable for long-period gratings in which the grating period exceeds 10 μm and even can be longer than 100 μm . In the present work, we fabricate the long period gratings using this technique.

5.3 Other types of gratings in optical fibers

FBGs and LPGs are the most widely used fiber gratings. However, other types of grating structures also find application in telecommunication and sensing. Chirped gratings with varying grating element along the length of the fiber, find application in sensing although they were originally developed for dispersion compensation in high bit-rate telecommunication systems. Another class of fiber gratings is the tilted gratings, where the gratings are tilted with respect to the fiber axis [44]. The main effect of grating tilt is to effectively reduce the coupling coefficient. Tilted gratings are used for both co-directional and contra-directional coupling. Both FBG and LPG along with chirped grating based optical sensors are superior to other fiber sensors in that they are self referencing in nature.

5.4 Theoretical Background

5.4.1 Coupled mode theory

A perfect dielectric waveguide can transmit optical energy by any of its guided modes without converting the energy to any of the other possible guided modes or to the non-guided modes which consists of a discrete set of cladding modes and a continuous spectrum of radiation modes [45].

For guided modes the orthogonality condition can be expressed as

$$\int_S [\overline{E}_i(x, y, z) \times \overline{H}_j(x, y, z)] \cdot dS = \delta_{ij} \frac{\beta}{|\beta|} \quad (5.1)$$

and for radiation modes,

$$\int_S [E(i) \times E(j)] \cdot dS = \delta(i - j) \frac{\beta}{|\beta|} P \quad (5.2)$$

where all the terms have the usual meaning as previously described in Chapter II. The modes of a given system form a complete set which means that the allowed modes span the entire space of the system. Therefore any general electric field configuration can be expressed as a linear combination of guided and non guided modes as given by

$$E(x, y, z) = \sum_{\text{guided}} a_i E_i(x, y, z) + \int_{\text{radiation}} \hat{a}(\beta) E(x, y, z, \beta) d\beta \quad (5.3)$$

where a_i are weight factors and \hat{a} is a unit normal.

Any imperfection in the guide, such as a local change of its index of refraction or a deviation from perfect straightness or an imperfection of the interface between two regions with different refractive indices, couples the power in a particular guided mode among other guided modes as well as unguided modes. Coupled mode theory describes this energy exchange, and serves as the primary tool for designing optical couplers, switches and filters.

5.4.2 Coupled mode equations for co-directional coupling

Consider a waveguide with a refractive index profile $n^2(x, y)$ in which there is an z -dependent perturbation given by $\Delta n^2(x, y, z)$. Let $\psi_1(x, y)$ and $\psi_2(x, y)$ be the two modes of the waveguide in the absence of perturbation. The total field at any value of z is given by

$$\psi(x, y, z) = A(z)\psi_1(x, y)e^{-i\beta_1 z} + B(z)\psi_2(x, y)e^{-i\beta_2 z} \quad (5.4)$$

β_1 and β_2 are the propagation constants in the absence of perturbation and $A(z)$ and $B(z)$ are the corresponding amplitudes. Here, modes with propagation constants β_1 and β_2 are propagating in the $+z$ direction. In the absence of perturbation A and B

are constants; the perturbation, however, couples power among the modes and hence A and B are z -dependent. Since ψ_1 and ψ_2 are modes of the fiber in the absence of any perturbation, they must satisfy the following equations:

$$\nabla_t^2 \psi_1 + [k_0^2 n^2(x, y) - \beta_1^2] \psi_1 = 0 \quad (5.5)$$

$$\nabla_t^2 \psi_2 + [k_0^2 n^2(x, y) - \beta_2^2] \psi_2 = 0 \quad (5.6)$$

where

$$\nabla_t^2 = \nabla^2 - \frac{\partial^2}{\partial z^2} \quad (5.7)$$

They also satisfy the orthogonality condition:

$$\int_{-\infty}^{\infty} \int_{-\infty}^{\infty} \psi_1^*(x, y) \psi_2^*(x, y) dx dy = 0 \quad (5.8)$$

In the presence of a perturbation in refractive index, the wave equation to be satisfied by $\psi(x, y, z)$ is

$$\nabla_t^2 \psi + \frac{\partial^2 \psi}{\partial z^2} + k_0^2 [n^2(x, y) + \Delta n^2(x, y, z)] \psi = 0 \quad (5.9)$$

Substituting for ψ from equation (5.4), and neglecting double derivatives of A and B w.r.to z (under slowly varying approximation), we get

$$-2i\beta_1 \frac{dA}{dz} \psi_1 - 2i\beta_2 \frac{dB}{dz} \psi_2 e^{-i\Delta\beta z} + k_0^2 \Delta n^2(x, y, z) [A\psi_1 + B\psi_2 e^{i\Delta\beta z}] = 0 \quad (5.10)$$

where

$$\Delta\beta = \beta_1 - \beta_2 \quad (5.11)$$

Multiplying equation (5.10) by ψ_1^* and integrating and then further multiplying by ψ_2^* and integrating, we get after simplifications :

$$\frac{dA}{dz} = -iC_{11}A - iC_{12}B e^{i\Delta\beta z} \quad (5.12)$$

$$\frac{dB}{dz} = -iC_{22}B - iC_{21}Ae^{-i\Delta\beta z} \quad (5.13)$$

where

$$C_y(z) = \frac{k_0^2 \iint \psi_i^* \Delta n^2 \psi_j dx dy}{2\beta_i \iint \psi_i^* \psi_i dx dy} \quad (5.14)$$

Equations 5.12 and 5.13 represent the coupled mode equations and describe the z -dependence of A and B .

5.4.3 Coupling by periodic perturbation

In the presence of z -dependent sinusoidal perturbation, we may write:

$$\Delta n^2(x, y, z) = \Delta n^2(x, y) \sin Kz \quad (5.15)$$

where $K = \frac{2\pi}{\Lambda}$, and Λ is the spatial period of perturbation. This gives

$$C_y(z) = \frac{k_0^2 \sin Kz \iint \psi_i^* \Delta n^2 \psi_j dx dy}{2\beta_i \iint \psi_i^* \psi_i dx dy} \quad (5.16)$$

$$C_y(z) = 2\kappa_y \sin Kz \quad (5.17)$$

where

$$\kappa_y = \frac{k_0^2 \iint \psi_i^* \Delta n^2(x, y) \psi_j dx dy}{4\beta_i \iint \psi_i^* \psi_i dx dy} \quad (5.18)$$

Substituting in equation 5.12, we get

$$\frac{dA}{dz} = -2i\kappa_{11}A \sin Kz - B\kappa_{12}e^{i(\Delta\beta+K)z} + B\kappa_{12}e^{i(\Delta\beta-K)z} \quad (5.19)$$

For weak perturbations, the coupling coefficients, κ_{12} and κ_{21} are small and hence, the typical length scale over which the modes amplitude change $(1/\kappa_{12}) \sim (1/\kappa_{21})$, is large. It can be shown that for $\Delta\beta \sim K$, the contributions from the first and second terms in the RHS of equation (5.19) are negligible as compared to the third term, and hence can be neglected. However, the second term would have made significant contribution if $\Delta\beta = \beta_1 - \beta_2 = -K$. Thus, in the presence of a periodic perturbation,

coupling takes place mainly between the modes for which $\Delta\beta$ is close to either K or $-K$. The approximation retaining either $e^{i(\Delta\beta-K)z}$ term or $e^{i(\Delta\beta+K)z}$ term in equation (5.19) is called the synchronous approximation.

Hence, under this approximation, equation (5.19) can be written as

$$\frac{dA}{dz} = \kappa_{12} B e^{i\Gamma z} \quad (5.20)$$

where
$$\Gamma = \Delta\beta - K \quad (5.21)$$

Similarly,
$$\frac{dB}{dz} = -\kappa_{21} A e^{-i\Gamma z} \quad (5.22)$$

If modes ψ_1 and ψ_2 are normalized to carry unit power, then under the weakly guiding approximation, we may write :

$$\frac{\beta_i}{2\omega\mu_0} \iint \psi_i^* \psi_i dx dy = 1 \quad (5.23)$$

Using orthonormality condition, we can show that

$$\kappa_{12} = \kappa_{21} = \kappa \quad (5.24)$$

Thus, the two coupled equations become

$$\frac{dA}{dz} = \kappa B e^{i\Gamma z} \quad (5.25)$$

$$\frac{dB}{dz} = -\kappa A e^{-i\Gamma z} \quad (5.26)$$

These two equations describe the coupling between two modes propagating along the same direction i.e. β_1, β_2 have same sign. This can be seen in the equation (5.4).

Such kind of coupling is co-directional coupling, as explained earlier also.

5.4.3.1 Co-Directional Coupling under Phase Matching Condition

Phase matching condition is given by $\Gamma = 0$

i.e.
$$\beta_1 - \beta_2 = K \quad (5.27)$$

Thus, the periodic perturbation should have period

$$\Lambda = \frac{2\pi}{\beta_1 - \beta_2} = \frac{\lambda_0}{(n_{e1} - n_{e2})} \quad (5.28)$$

where we have put $\beta_1 = \frac{2\pi n_{e1}}{\lambda_0}$ and $\beta_2 = \frac{2\pi n_{e2}}{\lambda_0}$, n_{e1}, n_{e2} are the effective refractive indices of the two modes. Then equations (5.20) and (5.22) become

$$\frac{dA}{dz} = \kappa B \quad (5.29)$$

$$\frac{dB}{dz} = -\kappa A \quad (5.30)$$

Differentiating (5.33) and making substitution from (5.34), we obtain

$$\frac{d^2 B}{dz^2} = -\kappa^2 B \quad (5.31)$$

Its solution is

$$B = b_2 \sin Kz - b_1 \cos Kz \quad (5.32)$$

Similarly,

$$A = b_1 \sin Kz - b_2 \cos Kz \quad (5.33)$$

Initial conditions assume that at $z=0$, the mode ψ_1 is launched with unit power,

$$A|_{z=0} = 1 \quad (5.34)$$

and initially ψ_2 had no power in it.

$$B|_{z=0} = 0 \quad (5.35)$$

Thus $b_1=0$ and $b_2=-1$ and therefore

$$A(z) = \cos \kappa z \quad (5.36)$$

Similarly,

$$B(z) = -\sin \kappa z \quad (5.37)$$

Thus the powers carried by the two modes vary with z as

$$P_1 = |A(z)|^2 = \cos^2 \kappa z \quad (5.38)$$

and

$$P_2 = |B(z)|^2 = \sin^2 \kappa z \quad (5.39)$$

Hence, we note that there is a periodic exchange of power between the two modes and for complete power transfer from E_1 to E_2 , we have

$$P_2 = 1 \text{ and } P_1 = 0$$

i.e at length $z = L_c$, $\sin \kappa z = 1$, and $\cos \kappa z = 0$.

$$\Rightarrow \kappa L_c = \frac{\pi}{2} \quad \text{or} \quad L_c = \frac{\pi}{2\kappa} \quad (5.40)$$

This is graphically shown in fig 5.5

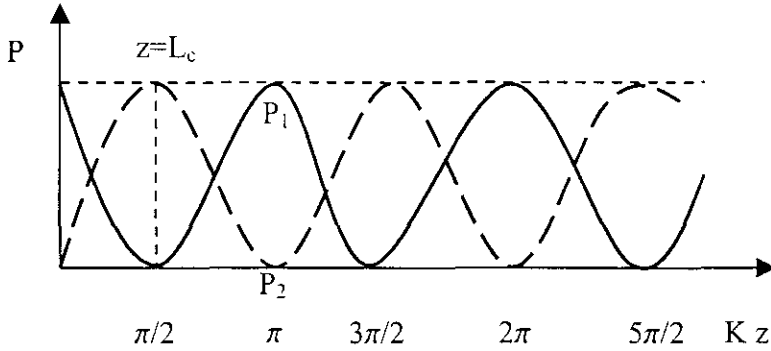


Fig 5.5: Power exchange between two modes as light propagates through a fiber in the z direction

5.4.3.2 Coupled mode equations for contra-directional coupling

When coupling takes place between two modes propagating in opposite directions, it is known as contra-directional coupling. In such a case, we will have to choose

$$\psi(x, y, z) = A(z)\psi_1(x, y)e^{-i\beta_1 z} + B(z)\psi_2(x, y)e^{i\beta_2 z} \quad (5.41)$$

Here, the mode with propagation constant β_1 is propagating in the $+z$ direction and the mode with propagation constant β_2 is propagating in the $-z$ direction. Following an exactly similar procedure, one obtains coupled mode equations for contra-directional coupling as:

$$\frac{dA}{dz} = \kappa B e^{i\Gamma z} \quad (5.42)$$

$$\frac{dB}{dz} = \kappa A e^{-i\Gamma z} \quad (5.43)$$

The signs on the RHS of equations 5.42 and 5.42 are same, unlike that in co-directional coupling, therefore, the solution in this case are not oscillatory.

5.4.4 Principle of operation of Long Period Gratings

In 1995, Vengsarkar *et al.* [17] introduced a new type of fiber grating device, long period grating (LPG) to the optics community. A typical LPG has a period of hundreds of microns, a length of about 1–3 cm, and an index modulation depth of 10^{-4} or greater. The optical power transmitted through the fiber as core modes at a wavelength λ , is coupled between core modes and cladding modes at the grating region as shown in fig 5.6.

In one approach this coupling process may be expressed as

$$\lambda = (n_{co} - n_{cl}(p))\Lambda \quad (5.44)$$

where Λ , n_{co} , $n_{cl}(p)$ are the period of the gratings, the effective refractive index of any of the core modes and the effective refractive index of the p^{th} cladding mode respectively. This equation is similar to (5.31). Since in single mode fibers there exists only one core mode (LP_{01}) and many cladding modes (LP_{lp}), the core-cladding coupling occurs at certain specific wavelengths. These wavelengths can be found out by calculating the various values of $n_{cl}(p)$ which in turn is determined by assuming a step index profile for the cladding and ignoring the presence of the core. The light in the cladding quickly decays due to losses at the cladding/air interface, leaving a series of loss bands or resonance in the guided mode as shown in fig 5.7.

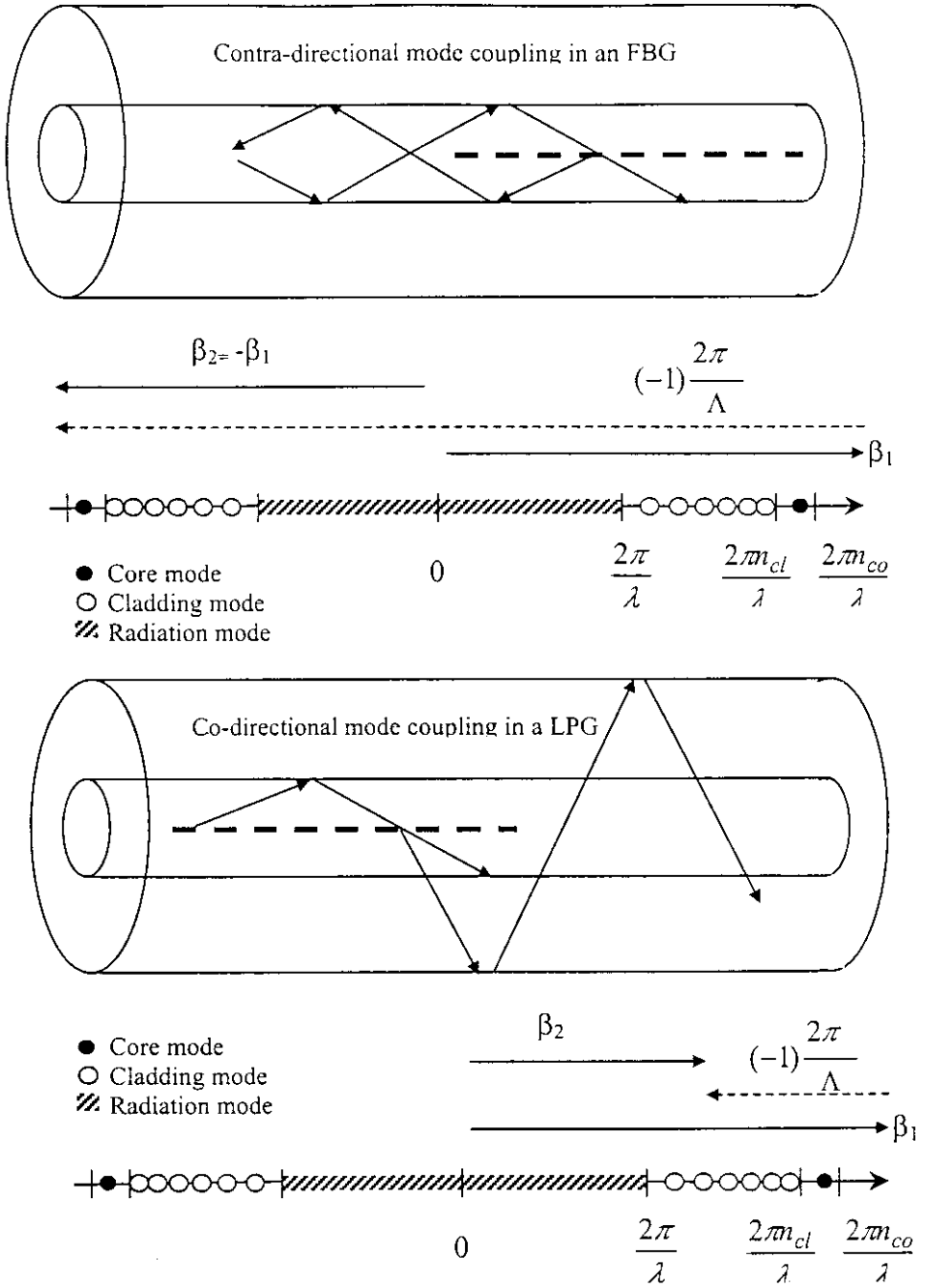


Fig 5.6: Ray-optic and modal illustration of core mode Bragg reflection by an FBG and cladding mode coupling by a LPG

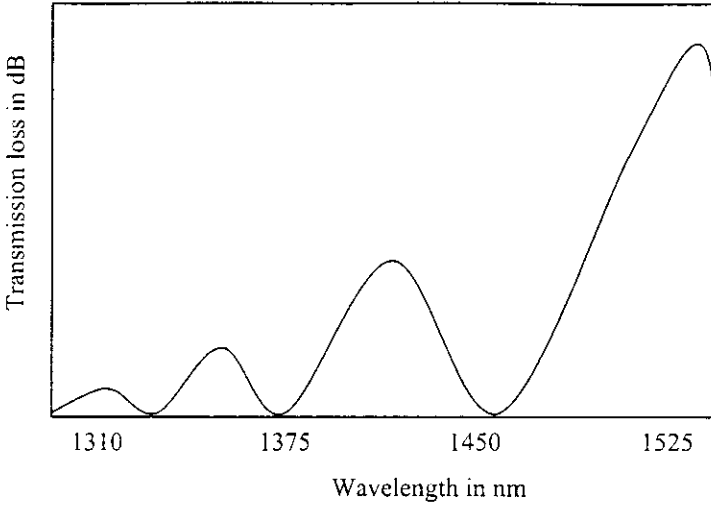


Fig 5.7: Loss bands of transmission in a single mode LPG

Another method of calculating the wavelength separation between the different cladding modes makes use of the cut-off wavelength λ_{cut} , which is the wavelength at which a given mode switches from a cladding mode to radiation mode or vice versa. We consider the transverse component of the propagation constant of the cladding mode κ . This component satisfies the condition

$$\beta_{cl}^2 + \kappa^2 = \frac{\omega^2 n_{cl}^2}{c^2} \quad (5.45)$$

where β_{cl} is the propagation constant of the cladding mode, ω is angular frequency of the radiation and c is the velocity of light. We first find the separation in wavelength between the p^{th} cladding mode and λ_{cut} by using the above two equations,

$$\lambda_p - \lambda_{cut} \approx \frac{\lambda_p^2 \lambda_{cut}^2}{8n_{cl}(n_{eff} - n_{cl})} \frac{p^2}{a_{cl}^2} \quad (5.46)$$

where n_{eff} is the effective refractive index of the guided LP_{0l} mode and a_{cl} is the cladding radius. For the first few cladding-modes one can further simplify the expression by assuming that λ_p and λ_{cut} are in close proximity. The wavelength separation between the p^{th} and the

$(p + l)^{th}$ mode can then be approximated by

$$\delta\lambda_{p,p+1} \approx \frac{\lambda_{cut}^3}{8n_{cl}(n_{eff} - n_{cl})} \frac{(2p+1)}{a_{cl}^2} \quad (5.47)$$

The ratio of power coupled into the n th-cladding mode to the initial power contained in the guided LP_{0l} mode is then given by

$$\frac{P_{cl}^{(n)}(l)}{P_{0l}(0)} = \frac{\sin^2 \left[\kappa_g L \sqrt{1 + \left(\frac{\delta}{\kappa_g} \right)^2} \right]}{1 + \left(\frac{\delta}{\kappa_g} \right)^2} \quad (5.48)$$

where δ is the detuning parameter given by

$$\delta = \frac{1}{2} \left\{ \beta_{0l} - \beta_{cl}^{(n)} - \frac{2\pi}{\lambda} \right\} \quad (5.49)$$

κ_g is the coupling constant for the grating and L is the grating length. The coupling constant κ_g is proportional to the UV-induced index change and is typically increased to maximize the power transfer to the cladding mode. Thus, Δn (and hence, κ_g) is increased until the condition $\kappa_g = \pi/2$ is met.

Assuming complete transfer, the full width at half maximum (FWHM) $\Delta\lambda$ of the spectral resonance defined by the previous equation is approximately given by

$$\Delta\lambda = \frac{0.8\lambda^2}{L(n_{eff} - n_{cl})} \quad (5.50)$$

5.5. Sensors based on fiber gratings

FBG was the first grating structure to be formed in an optical fiber. Eventhough it has been developed and used in communications since 1978, the demonstration of FBGs in sensor technology was done only in the late 1980s. Since then a myriad varieties of sensors followed. They are extensively used in strain monitoring and/or temperature sensing. Whenever there is a change in the grating structure (refractive index change

or grating period) of the fiber due to some environmental change, the reflected signal called the “Bragg” signal or the transmission spectrum of the fiber changes. The basic principle of operation commonly used in an FBG-based sensor system is to monitor this shift in wavelength of the transmitted signal or returned “Bragg” signal with the changes in the measurand (e.g., strain, temperature). For an FBG, the Bragg wavelength, λ_B or resonance condition of a grating can be derived from (31) by putting

$$\beta_1 = -\beta_2 = \frac{2\pi n_{eff}}{\lambda_B} \quad (5.51)$$

as
$$\lambda_B = 2n_{eff} \Lambda \quad (5.52)$$

where Λ is the grating pitch and n_{eff} is the effective refractive index of mode of the fiber. When a spectrally broadband source of light is injected into such a fiber, a narrowband spectral component at the Bragg wavelength is reflected by the grating. Perturbation of the grating results in a shift in the Bragg wavelength of the device, which can be, detected in either the reflected or transmitted spectrum, as shown. Most of the work on fiber Bragg grating sensors has focused on the use of these devices for providing quasi-distributed point sensing of strain or temperature. The strain response arises due to both the physical elongation of the sensor (and corresponding fractional change in grating pitch), and the change in fiber index due to photoelastic effects, whereas the thermal response arises due to the inherent thermal expansion of the fiber material and the temperature dependence of the refractive index. The shift in Bragg wavelength with strain and temperature can be expressed as

$$\Delta\lambda_B = 2n\Lambda \left(\left\{ 1 - \left(\frac{n^2}{2} \right) [P_{12} - \nu(P_{11} + P_{12})] \right\} \varepsilon + \left[\alpha + \frac{\left(\frac{dn}{dT} \right)}{n} \right] \Delta T \right) \quad (5.53)$$

where ε is the applied strain, P_{ij} coefficients are the Pockel’s coefficients of the stress-optic tensor, ν is the Poisson’s ratio, and α is the coefficient of thermal

expansion of the fiber material and ΔT is the temperature change. The factor $\{(n^2/2)[P_{12} - \nu(P_{11} + P_{12})]\}$ has a numerical value of ≈ 0.222 . The measured strain response at constant temperature is found to be

$$\frac{1}{\lambda_B} \frac{\delta \lambda_B}{\delta \varepsilon} = 0.78 \times 10^{-6} \mu\varepsilon^{-1} \quad (5.54)$$

This responsivity gives a “rule-of-thumb” measure of the grating shift with strain of 1 nm per 1000 $\mu\varepsilon$ at 1.3 μm . In silica fibers, the thermal response is dominant and accounts for $\approx 95\%$ of the observed shift. The normalized thermal responsivity at constant strain is

$$\frac{1}{\lambda_B} \frac{\delta \lambda_B}{\delta T} = 6.67 \times 10^{-6} \text{ } ^\circ\text{C}^{-1} \quad (5.55)$$

The above two equations respectively demand a wavelength resolution of ≈ 1 pm (0.001 nm) to resolve a temperature change of ≈ 0.1 $^\circ\text{C}$, and a strain of 1 μstrain , which is not unattainable using laboratory instrumentation.

The nature of the output of Bragg gratings provides these sensors with a built-in self-referencing capability. As the sensed information is encoded directly into wavelength, which is an absolute parameter, the output does not depend directly on the total light levels, losses in the connecting fibers and couplers, or source power. This is widely acknowledged as one of the most important advantages of these sensors. The wavelength-encoded nature of the output, however, also facilitates wavelength division multiplexing by allowing each sensor to be assigned to a different “slice” of the available source spectrum. This enables quasi-distributed sensing of strain, temperature, or potentially other measurands by associating each spectral slice with a particular spatial location. The upper limit to the number of gratings, which can be addressed in this way, is a function of the source profile width and the operational wavelength bandwidth required for each grating element. With current gratings, it is possible to multiplex 20 or more devices along a single fiber path if the peak strains experienced by the gratings do not exceed $\pm 0.1\%$.

5.5.1 Long Period Grating Sensors

LPG's were initially developed for use as band-rejection filters, and have been used for gain flattening EDFAs. However, LPG's also present unique opportunities as fiber optic sensors. An individual grating can have many resonances over a broad wavelength range, as illustrated by its transmission spectrum. The center wavelengths of the LPG resonances depend critically on the index difference between the core and the cladding, and hence any variation caused by strain, temperature, or changes in the external refractive index can cause large wavelength shifts in the resonances. Thus for strain and temperature sensing, LPG's are unique among fiber grating sensors in that an LPG resonance at a given wavelength can have a very different sensitivity, depending on the fiber type and the grating period. The strain and temperature response of a long period grating resonance can be either positive or negative, depending on the differential responses of the core and cladding [56]–[62]. An LPG resonance with a temperature response as low as $-0.20 \text{ nm}/^\circ\text{C}$, and positive response as large as $0.15 \text{ nm}/^\circ\text{C}$ has been reported [56]. The observed strain responses range from -0.0007 to $0.0015 \text{ nm}/\mu\epsilon$ [53]. Additionally, the responses of two resonance bands of the same LPG usually differ in magnitude. These properties make LPG's particularly useful for multi-parameter sensors such as the strain and temperature sensors discussed earlier. Two LPG resonances can be used to simultaneously determine strain and temperature using a single grating element, or an LPG resonance can be paired with an FBG to make the same measurement.

5.6 Experimental

Long period gratings with a period, $\Lambda = 500 \text{ }\mu\text{m}$ and length 10 mm are written in an unjacketed step index multimode plastic clad silica (PCS) fiber (Newport F-MBB) of N.A. 0.37 and core diameter $200 \text{ }\mu\text{m}$. The writing technique employed here is the point-by-point technique using the frequency tripled (355 nm , 9 ns) radiation from a pulsed Nd:YAG laser (Spectra-Physics GCR-170), which is operated in the single shot Q-switched mode. The fiber with the cladding is placed on a micro-translator, which can be moved in steps of $500 \text{ }\mu\text{m}$. The radiation from the

laser is focused on to the fiber using a quartz cylindrical lens. After each irradiation process the fiber is translated through 500 μm and the pattern was generated for a total length of 10 mm. The experimental setup used for fiber irradiation is given as the back cover of this thesis. The formation of gratings is clearly indicated by a loss in transmission. Apart from this observation, when light is allowed to pass through the fiber streaks of light from the grating region can be seen on the LPG fiber, similar to the case with a microbent optical fiber. The fiber gratings thus formed is used in evanescent wave chemical sensing. The schematic of the experimental setup for chemical sensing is shown in fig 5.8.

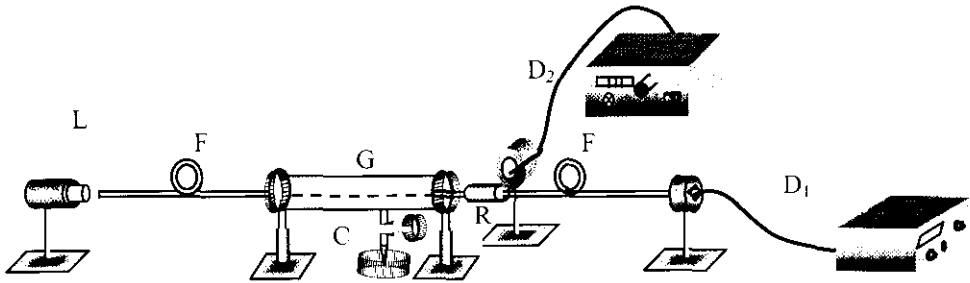


Fig 5.8: Schematic diagram of the experimental set-up L: He-Ne Laser (633 nm), C: Cell containing methylene blue in water, F: Optical Fiber, R: Index Matching Liquid, D₁: Detector 1 (Metrologic 45-545), D₂: Detector 2 (Infos M-100) G: Grating Region

To characterize the present sensor the grating is immersed in MB dye solution, which is kept at 20⁰C. The grating region of the fiber is immersed in a glass cell containing Methylene Blue (MB) dye solution, the absorption peak of which is at 664 nm. This grating sensor is powered by a continuous wave He-Ne laser (Spectra Physics) operating at 632.8 nm. The sensing technique used here is the bright and dark field detection schemes as previously employed in connection with microbent fibers. Detector D₁ (Newport 1815-C) measures core-mode power, which is placed at the output end of the fiber. In order to detect the cladding mode power an index matching liquid (R) is placed near the grating region (G), and the emerging light is collected using another optical fiber of core diameter 1000 μm and is coupled to a Detector D₂ (Infos M-100).

In order to record the transmission spectrum of a graded index multimode fiber and a step index multimode fiber, a white source (150 W tungsten-halogen lamp) with the help of a focusing lens (focal length = 5 cm) is used to illuminate the fiber. The detection is carried out by a collecting lens and a monochromator, which in turn is connected, to a computer through a digital multimeter (DMM) (HP 34410) and a photomultiplier tube (PMT) (Oriol), as shown in fig 5.9.

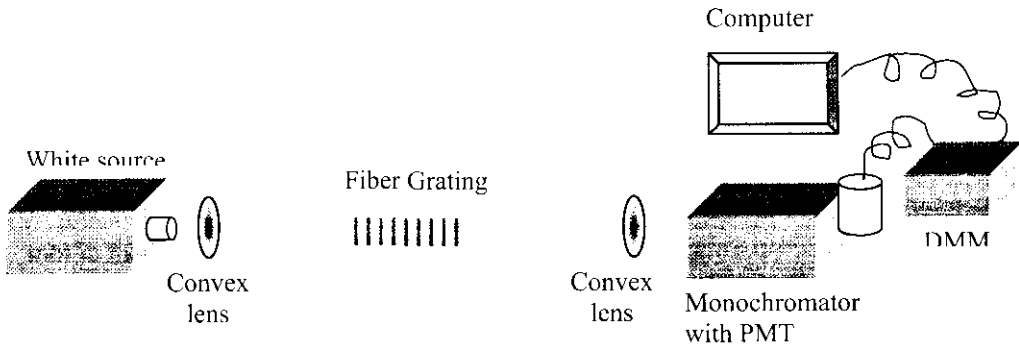


Fig 5.9: Schematic diagram of the experimental setup used for taking the transmission spectrum of fiber grating

5.7 Results and Discussion

The optical power transmitted through the fiber as core modes at a wavelength λ , is coupled between core modes and cladding modes at the grating region as shown in fig 5.10.

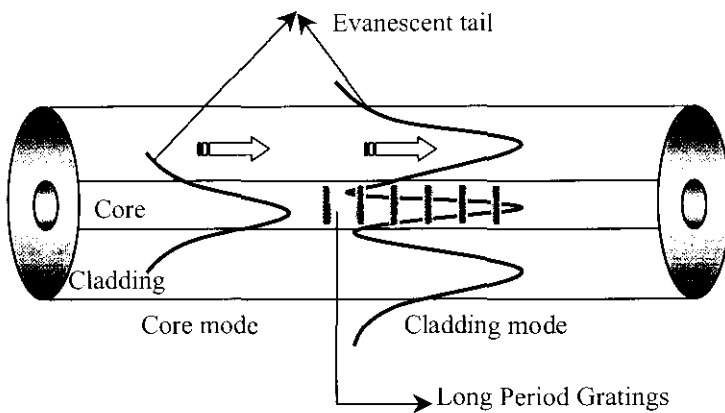


Fig 5.10: Diagram showing the core mode-cladding mode power coupling and the corresponding evanescent tails

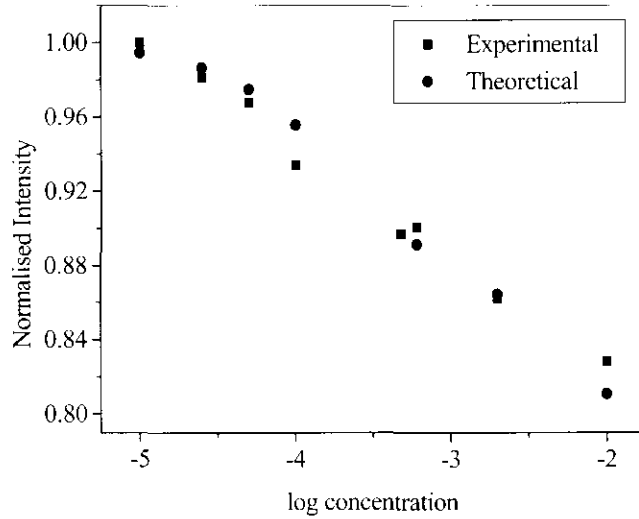


Fig 5.11: Plot showing core-mode intensity variation with dye

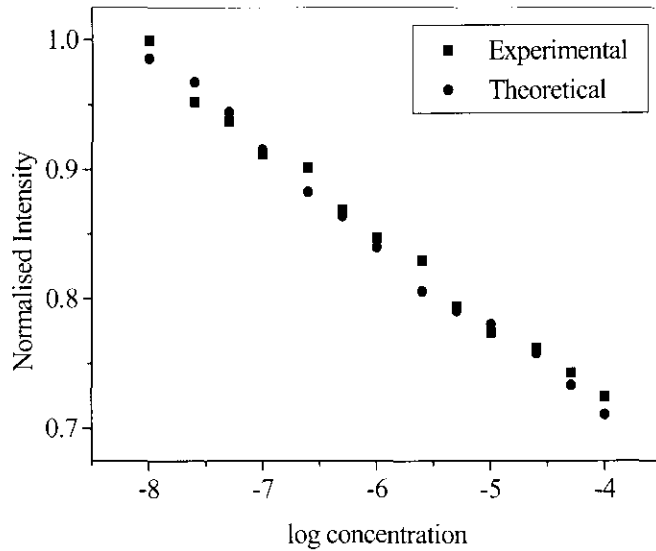


Fig 5.12: Plot showing cladding-mode intensity variation with dye

The optical power contained in the core and cladding modes is measured for various dye concentrations. The variation of the core mode intensity with concentration of the MB dye is shown in fig 5.11. This clearly indicates that the bright field detection scheme is sensitive enough to detect micro molar concentration

of chemical species. Nevertheless, the dark field detection scheme that detects the cladding mode power, with the help of an index matching liquid that surrounds the fiber just beyond the grating region, is seen to be even more sensitive with a detection limit of 10 nanomoles per litre as can be inferred from fig.5.12.

It may be noted that the index matching liquid has to be placed as close as possible to the grating region in order to have maximum cladding power. However, such a restriction does not impede the remote sensing capability of the present sensor which is made possible by using another optical fiber to collect the light coming out of the index matching liquid. Such a high sensitivity may be achievable with an unclad fiber also, but only with longer sensing length of about 100 mm as against 10 mm in this case.

Fig 5.10 throws light upon the basic mechanism of the present sensing technique. A part of the guided/core mode power in a fiber grating is coupled to unguided/cladding mode power at the sensing/grating region. Nevertheless, a part of this cladding mode power extends out of the cladding as evanescent tail, similar to the evanescent tail of core modes allowing the optical power to be absorbed by an absorbing chemical species that surrounds the cladding region. Such absorption reduces both core-mode power and cladding mode power as shown in figs 5.11 & 5.12 and this enables a fiber with cladding to act as an evanescent wave chemical sensor. It should be noted that this explanation of the observed effect falls in line with that given in the case of microbent chemical sensing. The method employed here differs from the conventionally used chemical sensing techniques employing LPG's where wavelength modulation takes place by the variations in the real part of the refractive index of surrounding medium. However, in the present case the basic mechanism behind the change in output intensity with concentration of MB dye is different. MB dye solution has a different refractive index than pure solvent. i.e., water. However, the main contribution for this change will be from the imaginary part of the refractive index, which corresponds to the optical absorption. In the present

case, this is due to the close match of the absorption peak of the MB dye with the propagating wavelength.

The fundamental equation that deals with evanescent wave sensing by conventional unclad fibers when power is assumed to be distributed equally among all the modes is given by

$$\frac{P_{out}}{P_{in}} = \frac{1}{N} \sum_{\nu=1}^N \exp(-\alpha \eta_{\nu} C l) \quad (5.56)$$

where P_{out} is the output power, P_{in} is the input power of the fiber, N is the total number of modal groups where each value of N represent a group of modes having the same penetration depth., $\alpha = 1.09 \cdot 10^5 \text{ mol}^{-1} \text{ cm}^{-1}$ is the molar absorption coefficient, η_{ν} is the modal fractional power in the cladding for ν^{th} core mode and l is the interaction length between the evanescent field and absorbing species of concentration C . However, in the present case some of the terms occurring in the above equation will have a slightly different meaning. It should be noted that, for a given wavelength, say 632.8 nm, all the core modes will not be coupled to cladding modes, but coupling takes place only for those modes which satisfy equation (5.44). Hence only a limited number of modes undergo core mode-cladding mode power coupling. η_{ν}' is the modal fractional power outside the cladding for ν^{th} cladding mode and $l=1 \text{ cm}$ is the length of the grating region. In the present case a curve fitting done by assuming $\alpha = 1.09 \cdot 10^5 \text{ mol}^{-1} \text{ cm}^{-1}$ and $l = 1 \text{ cm}$ gives the best curve fit for $N = 25$ by taking different values for η_{ν} . It can be seen from figs. 5.11 and 5.12 that the theoretically obtained data fits very well with the experimentally observed data, which clearly establishes the validity of the given relationship. It is observed that the present sensor shows detectable output variation, even with a dye concentration of a few nanomoles/litre.

The normalized transmission spectrum of a graded index fiber with LPG of 100 μm and length 10 mm is shown in the figure 5.13. The normalization is done by

using an ordinary graded index fiber without gratings. It can be seen that spectrum contains some peaks and valleys of transmission at some wavelengths.

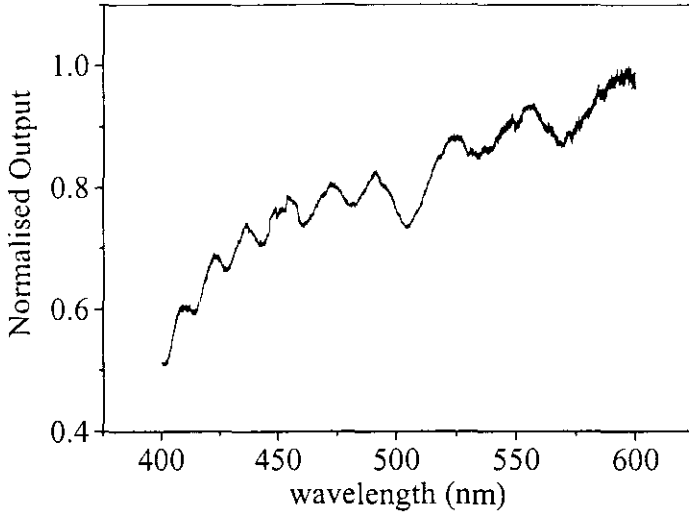


Fig 5.13: Normalized transmission spectrum of graded index fiber

The origin of such a spectrum may be due the fact that in a graded index fiber, the guided modes have equal spacing as already illustrated in chapter III. In addition, the cladding modes are not spaced equally in k-space and their intermodal spacing is proportional to the mode number. The cladding modes are usually found out by assuming a step index refractive index profile for the cladding without considering the presence of the core. This idea of mode spacing is shown in table 5.1 where $\beta_{co}(\mu)$ and $\beta_{cl}(\mu)$ are the assumed propagation constants of the μ^{th} core and cladding modes respectively. The core and cladding mode coupling is expressed as a difference between the corresponding propagation constants. The difference $\beta_{co}(\mu) - \beta_{cl}(\mu)$ signifies the power coupling between the μ^{th} core and cladding modes, while $\beta_{co}(\mu+1) - \beta_{cl}(\mu)$ gives the power coupling between the $(\mu+1)^{\text{th}}$ core and μ^{th} cladding mode.

μ	$\beta_{co}(\mu)$	$\beta_{cl}(\mu)$	$\beta_{co}(\mu) - \beta_{cl}(\mu)$	$\beta_{co}(\mu+1) - \beta_{cl}(\mu)$
1	3	1	2	
2	6	2	4	5
3	9	4	5	7
4	12	7	5	8
5	15	11	4	8
6	18	16	2	7

Table 5.1: simulation of the mode coupling in graded index fiber

It can be seen that all the possible values for the difference $\beta_{co}(\mu) - \beta_{cl}(\mu)$ and $\beta_{co}(\mu+1) - \beta_{cl}(\mu)$ gives a set of some specific values. The difference here corresponds to the wavelength of coupling and therefore it can be seen that the strength of mode coupling takes place only at a certain discrete set of wavelengths. In other words, the coupling between the guided modes and leaky modes will be large for some wavelengths and will be small for some other wavelengths. The transmission spectrum of a graded index fiber with LPG of grating period 100 μm and length 10 mm taken using an optical spectrum analyzer is shown in fig 5.14, which is similar to the one obtained with a monochromator. However, here the transmission wavelength chosen is in the NIR.

The normalized transmission spectrum of a step index fiber with LPG is shown in fig 5.15. Here the spectrum is smooth as against a wavy transmission spectrum for the graded index fiber. In the case of step index fiber, the inter-modal spacing is proportional to the mode number. That means the intermodal spacing for both core modes and cladding modes are varying with respect to the mode number. This is simulated in table 5.2. The mode coupling shown in this table similar to Table 5.1. It can be seen that, unlike in the case of graded index fiber, the difference between propagation constants can give rise to a set of any possible numbers. This means that in the case of a step index fiber, there is no restriction on wavelength for mode

coupling phenomenon to take place and hence it is independent of wavelength as experimentally obtained.

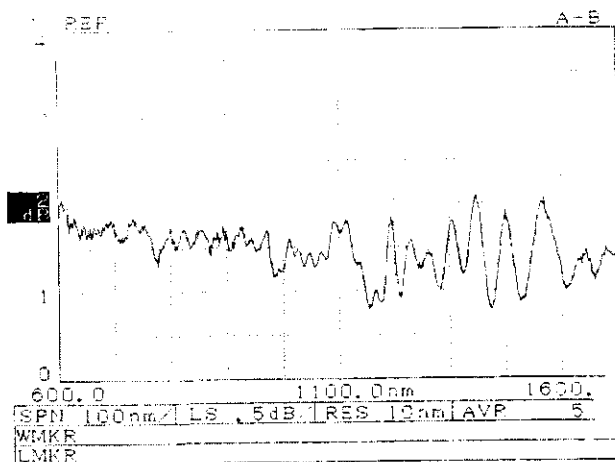


Fig 5.14: Transmission spectrum of graded index fiber.

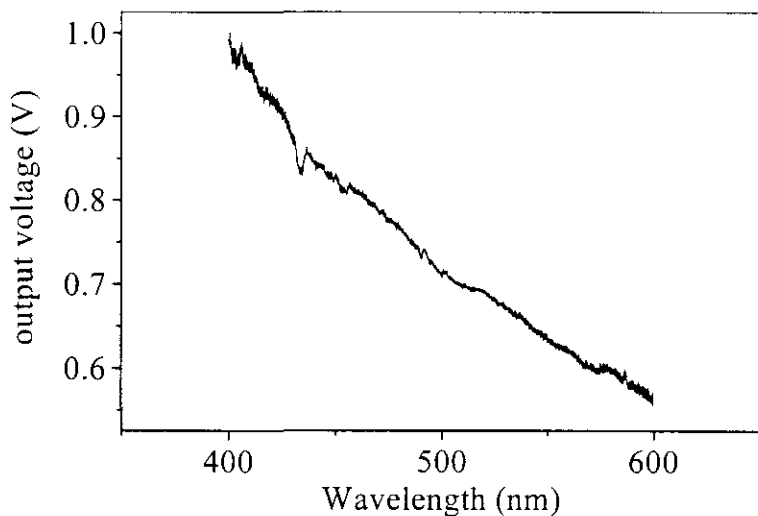


Fig 5.15: Normalized transmission spectrum of graded index fiber

μ	$\beta_{co}(\mu)$	$\beta_{cl}(\mu)$	$\beta_{co}(\mu) - \beta_{cl}(\mu)$	$\beta_{co}(\mu+1) - \beta_{cl}(\mu)$
1	2	1	1	
2	4	2	2	3
3	7	4	3	5
4	11	7	4	7
5	16	11	5	9
6	22	16	6	11

Table 2: simulation of the mode coupling in step index fiber

This chapter describes the fabrication of long period gratings in step index and graded index multimode fibers by point-by-point laser writing technique. The transmission properties of both types of fibers are studied. In addition, such grating written fibers are found to be ideal candidates for evanescent wave chemical sensing application, mainly because of short sensing length and double detection scheme.

REFERENCE:

1. K O Hill, Y Fujii, D C Johnson and B S Kawasaki, *Appl. Phys. Lett.* **32**, 647 (1978)
2. J Bures, J Lapierre and D Pascale, *Appl. Phys. Lett.* **37**, 860 (1980)
3. G Meltz, W W Morey and W H Glenn, *Opt. Lett.* **14**, 823 (1989)
4. D M Bird, J R Armitage, R Kashyap, R M A Fatah, and K H Cameron, *Electron. Lett.* **27**, 1115-1116 (1991)
5. F Bilodeau, K O Hill, B Malo, D C Johnson, and I M Skinner, *Electron. Lett.* **27**, 682 (1991)
6. G A Bail and W W Morey, *IEEE Photon. Technol. Lett.* **3**, 1077, (1991)
7. F Bilodeau, K O Hill, B Malo, D C Johnson and J Albert, *IEEE Photon. Technol. Lett.* **7**, 388 (1995)
8. L Dong, P Hua, T A Birks, L Reekie, and Pt. S. J. Russell, *IEEE Photon. Technol. Lett.* **8**, 1656 (1996)
9. D K W Lam and Garside, *Appl. Opt.* **20**, 440 (1981)
10. K O Hill, B Malo, F Bilodeau, S Theriault, D C Johnson and J Albert, *Opt. Lett.* **20**, 1438 (1995)
11. X M Tao, L Q Tang, W C Du and C L Choy, *Composites Sci. Technol.* **60**, 657 (2000)
12. G Duck and M M Ohn, *Opt. Lett.* **25**, 90 (2000)
13. N Takashi, K Yoshimura, S Takashi and K Imamura, *Ultrasonics*, **38**, 581, (2000)
14. N Takashi, K Yoshimura, S Takashi and K Imamura, *IEICE Trans. Elec.* **82**, 275 (2000)
15. X W Shu and D X Huang, *Opt. Comm.* **171**, 65 (1999)
16. A I Gusarov, F Beghmans, O Deparis, A F Fernandez, Y Defosse, P Megret, M Decreton and M Blondel, *IEEE Phot. Technol. Lett.* **11**, 1159 (1999)
17. L Yu-Lung and C Han-Sheng, *Meas. Sci. Technol.* **9**, 1543 (1998)
18. N Takashi, A Hirose, and S Takashi, *Opt. Rev.* **4**, 691 (1997)
19. G P Brady, K Kalli, D J Webb, D A Jackson, L Reekie and J L Archambault, *IEE Proc.- Optoelectronics*, **144**, 156 (1997)
20. A M Vengsarkar, J A Greene and K A Murphy, *Opt. Lett.* **16**, 1541 (1991)
21. A M Vengsarkar, P J Lemaire, J B Judkins, V Bhatia, T Erdogan and J E Spie, *IEEE J. Lightwave Technol.* **14**, 58 (1996)
22. A M Vengsarkar, J R Pedrassani, J B Judkins, P J Lemaire, N S Bergano and C R Davidson, *Opt. Lett.* **21**, 336 (1996)
23. K T V Grattan and T Sun, *Sens. Act. A*, **82**, 40 (2000)
24. A D Kersey, M A Davis, H J Patrick, M LeBlanc, K P Koo, C G Askins, M A Putnam and E J Friebele, *IEEE J. Lightwave Technol.* **15**, 1442 (1997)
25. K O Hill and G Meltz, *IEEE J. Lightwave Technol.* **15**, 1263 (1997)
26. T Erdogan, *IEEE J. Lightwave Technol.* **15**, 1277 (1997)
27. V Bhatia and A M Vengsarkar, *Opt. Lett.* **21**, 692, (1996)
28. V Grubsky and J Feiberg, *Opt. Lett.* **4**, 203 (2000)
29. J L Archambault and S G Grubb, *IEEE J. Lightwave Technol.* **15**, 1578 (1997)
30. H J Patrick, A D Kersey and F Bucholtz, *IEEE J. Lightwave Technol.* **16**, 1606 (1998)
31. M Douay, W X Xie, T Taunay, P Bernage, P Niray, P Cordier, B Poumellec, L Dong, J F Bayon, H Pignat and E Delevaque, *IEEE J. Lightwave Technol.* **15**, 1329 (1997)
32. C G Askins and M A Putnam, *IEEE J. Lightwave Technol.* **15**, 1363 (1997)

33. S Kannan, J Z Y Guo and P J Lemaire, *IEEE J. Lightwave Technol.* **15**, 1478 (1997)
34. S LaRochelle, V Mizrahi, G I Stegeman and J E Spie, *Appl. Phys. Lett* **57**, 747 (1990)
35. T E Tsai, G M Williams and E J Friebele, *Opt. Lett.* **22**, 224 (1997)
36. M M Broer, R L Cone and J R Simpson, *Opt. Lett.* **16**, 1391 (1991)
37. V Mizrahi and J E Spie, *IEEE J. Lightwave Technol.* **11**, 1513 (1993)
38. H J Patrick, C G Akins, RW McElhalon, and E J Friebele, *Electron. Lett.* **33**, 1167 (1997)
39. J A Rogers, R J Jackman, G M Whitesides, J L Wagener, and A M Vengsarkar, *Appl. Phys. Lett.* **70**, 7 (1997)
40. B Malo, S Theriault, D C Johnson, F Bilodeau, J Albert and K O Hill, *Electron. Lett.* **31**, 223 (1995)
41. J Albert, K O Hill, B Malo, S Theriault, F Bilodeau, D C Johnson and L E Erickson, *Electron. Lett.* **31**, 222 (1995)
42. V Grubsky, A Skorucak, D S Starodubov and J Feinberg, *IEEE Photonics Technol. Lett.* **11**, 87 (1999)
43. E M Dianov, D S Starodubov, S A Vasiliev, A A Frolov and O I Medvedkov, *Opt. Lett.* **22**, 221 (1997)
44. W W Morey, G Meltz J D Love and S J Hewlett, *Elec. Lett* **30**, 730 (1994) (titled)
45. D Marcuse, *App. Opt.* **17**, 3232 (1978)

Summary and Conclusions

Fiber optic sensors have their own unique place in sensing applications. They have been with us for the past 30 odd years. Most of the sensors developed in laboratories could be commercialised. Their study is important not only from the commercial point of view but also from the technological point of view. Many new ideas of physics have been evolved during the study of fiber optics. Therefore, it is worthwhile to devote some time to develop new sensing configurations and sensors as done during this research work.

Fabrication and characterization of evanescent wave fiber optic pH sensors is discussed. Both short-range and wide-range pH sensors are developed. It is carried out by immobilising pH sensitive dyes (bromocresol purple, bromocresol green and cresol red) using the sol-gel dip coating technique on the unclad portion of an optical fiber. Single layer films coated by this procedure gives a fractional change in intensity of only 15% leading to poor sensitivity of the device. The thickness of the thin film has been found to be $\sim 200\text{nm}$ which is less than the evanescent wave penetration depth. Multi-layer sol-gel coatings impregnated with dye has been found to increase the sensitivity considerably. It can be inferred that there is a high level of

interconnectivity between pores in different layers of the dye doped sol-gel thin film. This also contributes to the increased sensitivity of multi-layer sol-gel coatings. However, the response time of the sensor has been found to be adversely affected by increasing the number of layers. The pH value of the fluid can be monitored continuously without a break unlike pH electrode. An added feature of the present device is that its sensing region can be considerably reduced without any appreciable loss of sensitivity. This reduction in uncladded length gives the device better ruggedness. It is observed that the present device is reusable and found to give repeatable results even after using continuously for hours.

We demonstrate the behaviour of a permanently microbent fiber optic sensor immersed in an absorbing medium. Two distinct detection schemes viz., bright field detection and dark field detection configuration have been proposed for the measurements. The optical power propagating through the sensor has been found to vary with the concentration of the absorbing species in the surrounding medium. The present sensor has been found to be sensitive enough to detect concentrations as low as nano moles/litre of a chemical species, with a dynamic range of more than six orders of magnitude. Additionally, it has been observed that the sensitivity of the sensor is dependent on the bending amplitude and length of the microbend region in bright field detection scheme while it is almost independent of both in the dark field detection configuration. This indicates the possibility that the latter feature can be exploited in compact sensor designs thereby reducing the length of the sensing region without sacrificing their sensitivity. Moreover, the present sensing scheme is shown to be viable for refractive index measurements as well. Optical fiber sensors developed for measuring pH values usually employ an unclad and unstrained section of the fiber. However, we describe the design and fabrication of a microbent fiber optic sensor that can be used for pH sensing. In order to obtain the desired performance, a permanently microbent portion of a plastic optic fiber is coated with a thin film of dye impregnated sol-gel material. The results of measurements of core

mode-power and cladding mode-power variation with change in pH of a solution surrounding the coated portion of the fiber is presented.

We have demonstrated how evanescent wave field in optical fibers of various types viz., unclad and microbent fibers; can be successfully exploited for detection of trace amounts of Fe^{3+} and Mn^{2+} in water. The results obtained using two fibers viz., an unclad multimode PCS fiber and microbent plastic fiber, are used for a comparative study, which reveals that the latter is more versatile in Fe^{3+} sensing application. It can be clearly seen that the sensitivity is only slightly affected by effectively reducing the response time. In addition, a LabVIEW environment is created in the lab for data acquisition. An inexpensive source-detector combination made of an LED and a photodiode proves to be as sensitive as a laser-power meter combination for Mn^{2+} sensing. A Fiber optic Mach-Zehnder interferometer is constructed for weight and displacement sensing. The sensor is sensitive enough to detect a mass of 1 mg or a displacement of 10 μm . The detection is done by a self-built fringe counter.

We have presented the performance of a very sensitive evanescent wave chemical sensor by creating long period gratings in a multimode step index fiber. The output intensity is approximately linearly dependent on the logarithm of concentration of the absorbing species surrounding the grating region of the fiber in both bright and dark field detection configurations. Moreover, the sensor is highly sensitive and can even detect very low concentrations of the order of 10 nanomoles per liter using the dark field detection scheme. Furthermore, the dynamic range of operation is found to be greater than 4 orders of magnitude. A comparative study with a conventional unclad evanescent wave sensor reveals that the present sensor is superior in many aspects, such as short sensing length and use of double detection scheme to facilitate more reliable and accurate measurements. The transmission characteristics of grating written step index and graded index fibers are studied.

G8542

Future prospects

The work detailed in this chapter can form the basis for the development of a variety of sensors. Therefore, additions can be made to this work to make new devices as well as study the characteristics of new fibers and sensors. A list of possible future work is given below.

- A hand held fiber optic pH meter can be made using an LED or diode laser in conjunction with a photodiode detector assembly.
- The use of fiber sensors for aqueous contaminant detection can be extended to other harmful ions such as Chlorine or volatile organic compounds like dichloro methane and tetra choloro ethylene.
- Long period gratings in multimode fibers are promising candidates for sensing as well as communication applications. A detailed study based on changing the grating period and forming chirped or tilted gratings can be carried out using an optical spectrum analyser.

G18542